

Modeling of
marine biogeochemical cycles
with an emphasis on
vertical particle fluxes

Regina Usbeck

Alfred-Wegener-Institut für Polar- und Meeresforschung
PF120161, D-27515 Bremerhaven

Die vorliegende Arbeit ist die inhaltlich unveränderte Fassung einer Dissertation, die 1999 im Fachbereich Physik/Elektrotechnik der Universität Bremen vorgelegt wurde.

Eine Farbversion dieses Dokumentes kann bezogen werden unter:
<http://www.awi-bremerhaven.de/GEO/Publ/PhDs/RUsbeck>

Contents

Zusammenfassung	iv
Abstract	v
1 Introduction	1
1.1 The biological pump	4
1.2 Biogeochemical modeling	8
2 The adjoint model	14
2.1 Basics	15
2.2 Optimization	16
2.3 Data and model geometry	18
2.4 Model parameters	20
2.5 Advection-/diffusion matrix	22
2.6 Gas exchange and heat flux	24
2.7 Model particle fluxes	24
2.7.1 Export production	26
2.7.2 Remineralization	28
2.7.3 Accumulation	29
2.7.4 River input	30
2.7.5 Comment on the constraints of model particle fluxes	31
2.8 Costfunction	31
2.8.1 Terms of costfunction $F(p^*, \tilde{p})$	32
2.8.2 Weighting of costfunction $F(p^*, \tilde{p})$	33
2.9 Experiments	35
3 General model results and reference experiment	37
3.1 Current field	38
3.2 Property distributions	42
3.3 Model particle fluxes	46

4	Particle fluxes in the water column: Sediment traps	53
4.1	Data	55
4.2	Experiments with assimilated sediment trap data	60
4.2.1	Organic carbon fluxes, some examples	60
4.2.2	Model fluxes vs. sediment trap data	63
5	Accumulation of biogeneous particles	68
5.1	Sediment accumulation rate data	68
5.2	Model sediment accumulation rates	69
5.3	Distribution of surface sediments in the Atlantic	72
6	A special case: <i>Opal</i> fluxes in the Weddell Sea	76
7	Conclusions	82
A	River input	85
B	Derivatives of costfunction $F(p^*, \tilde{p})$	87
B.1	Euphotic zone	87
B.2	Water column	87
B.3	Sediment-water interface	88
B.4	Riverine input	88
B.5	Deviations from sediment trap data	88
C	New variables and routines	90
C.1	New variables	91
C.1.1	moddat.h	91
C.1.2	parflux.prm	91
C.1.3	sediments.h	92
C.1.4	deprm.h	92
C.2	New routines	93
C.2.1	lfluxdat(finam,dat,edatmi,ident)	93
C.2.2	laccudat(finam,dat,edatmi,ident)	93

C.2.3	setrivers	93
C.2.4	calbiofl(p,np)	94
C.2.5	ofdbioflux(p,objgrd,np,objf,tobjf,tffak,ifobjf)	94
C.2.6	ofdacc(p,objgrd,np,objf,tobjf,tffak,ifobjf)	94
C.2.7	ofsmip(p,objgrd,np,objf,tobjf,tffak,ifobjf)	95
C.2.8	ofapbg(p,objgrd,np,objf,tobjf,tffak,ifobjf)	95
D	Abbreviations and units	96
	Acknowledgments	98
	References	99

Zusammenfassung

Diese Arbeit beschäftigt sich mit marinen biogeochemischen Kreisläufen von Nährstoffen und Silikat. Biogene Partikelflüsse von organischem Kohlenstoff, Karbonat und Opal werden mit einem adjungierten Modell gleichzeitig mit der ozeanischen Zirkulation bestimmt. Die Advektion und Diffusion gelöster Nährstoffe, die Produktion und der Abbau, sowie die Akkumulation von Partikeln werden so parametrisiert, daß ein mit hydrographischen Daten und gelösten Nährstoffen konsistentes Modell des Strömungsfeldes und der Partikelflüsse entsteht. Es wird gezeigt, daß die Modellverteilungen von Temperatur, Salinität und gelösten Nährstoffen in gute Übereinstimmung mit den Daten gebracht werden können. Das berechnete Strömungsfeld ist im Einklang mit geostrophischer Dynamik und enthält alle wichtigen Wassermassentransporte, die Partikelflüsse sind realistisch in ihrer Verteilung und Größenordnung.

Ein Hauptziel der Untersuchungen war der Vergleich von adjungiert berechneten Partikelflüssen mit direkten Messungen. Hierfür wurden Sinkstoffallendaten des Sonderforschungsbereiches 261, "Der Südatlantik im Spätquartär", in das Modell aufgenommen. Der Vergleich von Modellergebnissen und Fallendaten ergibt generell höhere Flüsse im Modell. Das zum Reproduzieren der Sinkstoffallendaten gezwungene Modell behält systematische Abweichungen bei; eine Lösung, die mit Sinkstoffallendaten und Nährstoffen gleichzeitig konsistent ist, konnte nicht gefunden werden. Die Ergebnisse deuten darauf hin, daß Sedimentfallen Sinkstoffe nicht quantitativ messen. Die Fangeffizienz scheint, besonders in geringen Wassertiefen, gering zu sein.

Weiterhin wurde das Modell erweitert, so daß Akkumulationsraten berechnet werden können. Die Nährstoffbudgets in der bodennächsten Schicht des Modells werden zur Bestimmung von Partikelflüssen in das Sediment genutzt. Die resultierenden Akkumulationsraten von organischem Kohlenstoff und Opal stimmen teilweise mit unabhängigen Schätzungen überein, Karbonatflüsse scheinen vom Modell unterschätzt zu werden. Dennoch bietet das hier vorgestellte Modell eine neue, unabhängige Methode, um mittlere Akkumulationsraten zu berechnen.

Das Weddellmeer hebt sich im Modell als ungewöhnliches Gebiet ab. Generell gilt der Südozean (SO) als HNLC (High Nutrient Low Chlorophyll) Region, d.h., trotz hohem Nährstoffangebot bleibt die Produktion von organischem Kohlenstoff relativ gering. Andererseits finden sich im SO sehr hohe Si/C Verhältnisse im partikulären Material und der SO wird als wichtiges Gebiet für den Silikatkreislauf angesehen. Dies spiegelt sich im Modell durch hohe Opalflüsse im flacheren Wasser wider, die aber durch extreme Lösung nicht in den tieferen Ozean gelangen und so auch nicht zur Sedimentakkumulation beitragen.

Die hier gezeigten Ergebnisse ermutigen dazu, die adjungierte Methode zur unabhängigen Berechnung von Partikelflüssen heranzuziehen. Mit höherer Auflösung und Einbeziehung weiterer Tracer könnte das Modell auch für Aussagen über biogeochemische Kreisläufe in regionalem Maßstab genutzt werden.

Abstract

This study investigates oceanic biogeochemical cycles of nutrients and silicate.

An adjoint model is used to calculate the 3D large scale ocean circulation and biogeochemical fluxes of nutrients and silicate simultaneously. Advection and diffusion of dissolved nutrients, production of particulate matter, and vertical particle fluxes are parameterized to achieve a 3D flow field and biogeochemical particle fluxes consistent with hydrographic and nutrient data. Vertical fluxes are parameterized for particulate organic carbon, calcite, and opal separately. It is shown that simulated distributions of temperature, salinity, nutrients and silicate can indeed be brought to good agreement with data. The resulting flow field is consistent with geostrophic dynamics and contains major current. Resulting biogeochemical particle fluxes are reasonable in their spatial distribution and magnitude. A major goal of the model calculations is to examine whether particle fluxes determined with the adjoint method conflict with direct flux measurements. Sediment trap data from the German Joint Research Project SFB261 "The South Atlantic in the Late Quaternary" are assimilated into the model. The comparison of model results and sediment trap data reveals that model fluxes are generally higher than direct measurements. Even if the model is forced to reproduce sediment trap data, systematic deviations remain. A solution which gives particle fluxes in agreement with sediment trap data *and* data of dissolved nutrients cannot be obtained. The results from adjoint modeling indicate that sediment traps do not catch sinking particles quantitatively but trapping efficiency seems to be low, especially at shallow water depths.

An extension of the model is the calculation of sediment accumulation rates. Budgets of dissolved nutrients in the bottom layer are used for indirect determination of accumulation rates for organic carbon, calcite, and opal. The accumulation rates derived with the adjoint model are partly agree with recent independent estimates. Model values for calcite accumulation are lower than literature values.

The resulting model fields of physical circulation and biogeochemical fluxes bear very special conditions in the Weddell Sea. The Southern Ocean is generally identified as a HNLC (High Nutrients Low Chlorophyll) region, i.e. organic carbon production is low in spite of high nutrient concentrations in surface waters. Further it is known that the Southern Ocean plays a major role in silica cycling which is reflected in high model opal productivity. On the other hand, opal fluxes in the deep Weddell Sea were found to be rather low. The 'high production low flux anomaly' is also reproduced in the model results.

The results presented in this study give confidence that adjoint modeling can be used to calculate vertical particle fluxes from water column nutrient distributions. It is proposed that further refinement of the model grid and the inclusion of more, independent tracers in the model calculations can be used for a better understanding of biogeochemical cycles.

1 Introduction

The world ocean is a very complex dynamical system that permanently redistributes large amounts of energy and matter over large distances. Depending on the processes involved, cycling occurs on a variety of time scales. The ocean is a huge reservoir of heat, salt, CO_2 , oxygen, and nutrients and interacts with the lithosphere and the atmosphere. Along spreading pathways, sea water properties are affected and modified by many processes. Particulate and dissolved substances are added by aeolian and riverine input. The substances undergo several modifications and are finally accumulated at the sea floor forming deep sea sediments. It is assumed that the oceanic cycles are currently at a quasi-steady state, i.e. inputs and outputs of any substance are approximately in balance. By knowing the concentrations of a particular constituent in sea water and its rate of removal and/or addition from/to the ocean it is possible to calculate the specific residence time. The residence times cover a wide range from a few years (^{210}Pb , ^{230}Th) to about 2×10^8 years (sodium, chloride). The different time scales reflect the very heterogeneous processes making the oceans an interesting study object for many disciplines in modern science.

Ocean circulation controls the budgets of fresh water and heat. Thus, ocean circulation directly affects atmospheric circulation and the daily weather. Small changes in ocean circulation may cause major disturbances in the global climate. The 'El Niño' event is a special case which is currently of major public interest because of its impact on local fisheries and global climate.

The interest in climate forecasts has continuously grown over the last years not only because of time limited phenomena as 'El Niño' but also because it is believed that increasing atmospheric CO_2 and methane concentrations may cause major long-term modifications of today's environment ("Greenhouse effect"). CO_2 is dissolved in sea water at different rates depending on surface temperature and CO_2 partial pressure differences. Large sinks of atmospheric CO_2 are found in the northern polar region whereas the ocean is a source of CO_2 in low latitudes. The global ocean conveyor belt takes about a time scale of 1,000 years so the water transports atmospheric CO_2 approximately at this rate to the deep ocean. The oceanic uptake of CO_2 is an important current research topic for oceanographers and meteorologists.

The CO_2 storage capabilities of the ocean not only depend on ocean circulation but also on biogeochemical processes. Phytoplankton living in the surface layer of the ocean consumes dissolved nutrients (phosphate and nitrate) and also CO_2 . During photosynthesis, the inorganic components are reformed to build organic matter. The CO_2 concentration near the sea surface is lowered whereas oxygen is released. This process is commonly named primary production (PP) and forms the very beginning of the biological food-chain upon which all surface oceanic life depends. Life on earth is mostly restricted to earth's surface where the sun provides a more or less continuous supply of energy.

The ocean covers about 71% of the earth's surface and so the ocean is very important for global cycling because of its huge extents although biological productivity per unit area is relatively small compared to land. Furthermore, ocean circulation serves as a large-scale global redistributor for all inherent constituents.

Particles resulting from primary production are partly consumed by zoo-plankton and fish (secondary producers) and, after completing their life cycles, dead primary and secondary producers sink towards the sea floor. This results in a net transport of organic matter (and so nutrients and CO_2) into the deep ocean. These processes are known as the “biological pump” and are discussed in greater detail in section 1.1. Many biologists, fisheries engineers, and biological oceanographers have great concern in the biological upper ocean processes for economical and ecological reasons. Also, the biological pump affects surface CO_2 partial pressure and is in this way linked to other oceanographic disciplines mentioned above.

At the sea floor, terrigenous sediments (which are transported into the ocean by rivers, wind, and ice) and biogenous sediments (the remains of biological production reaching the sea floor) are ‘removed’ from the marine system. Matter buried in the deep ocean does no longer participate in marine cycles, and thus the sediment can be interpreted as a net sink. The deep sea sediments again undergo several modifications before they are finally partly subducted at plate boundaries and partly accreted to continental plates. The recycling of the lithosphere occurs on geological time scales of several million years but closes the cycle because the subducted and accreted matter finally builds new crust which is then eroded and brought back to the ocean. The deep sea sediments form an archive which stores information about marine processes over very long times. The deep sea sedimentary record is nearly the only information source concerning marine geological history. Geologists study deep sea drilling cores to reconstruct marine palaeo-environments which helps to better understand natural climatological fluctuations.

The information which is extracted from sediment cores is very heterogeneous. The remains of phytoplankton record the upper ocean processes (productivity, temperature, etc.), terrigenous components reflect intensity of matter input (strength of winds, river discharge, etc.). For some environments, the terrigenous signal might be negligible (e.g. in the pelagic deep sea) whereas in some regions the marine biogeochemical signal might be not recoverable because terrigenous sediments dominates the record (e.g. near most river mouths). A major problem in marine geology is that the ‘coding’ of the signals found in deep sea sediments is not well understood and that the difference in signal coding might be large between different areas. A key for the interpretation of sedimentary data is the net accumulation rate. The total accumulation of a given substance directly influences the residence time in the ocean and gives estimates for the strength of a particular process.

In the last years, increasing effort has been spent to understand biogeochemical cycles in order to determine the rates of input, recycling, and removal of matter and energy in the ocean. Only a better understanding of all modifications will finally allow a more accurate interpretation of the signals in sediment cores. Information about cycling in the oceans is not only stored in the sediments but also in property distributions in the world ocean. Figure 1.1 shows the distribution of temperature, salinity, oxygen, and phosphate along a section in the western Atlantic.

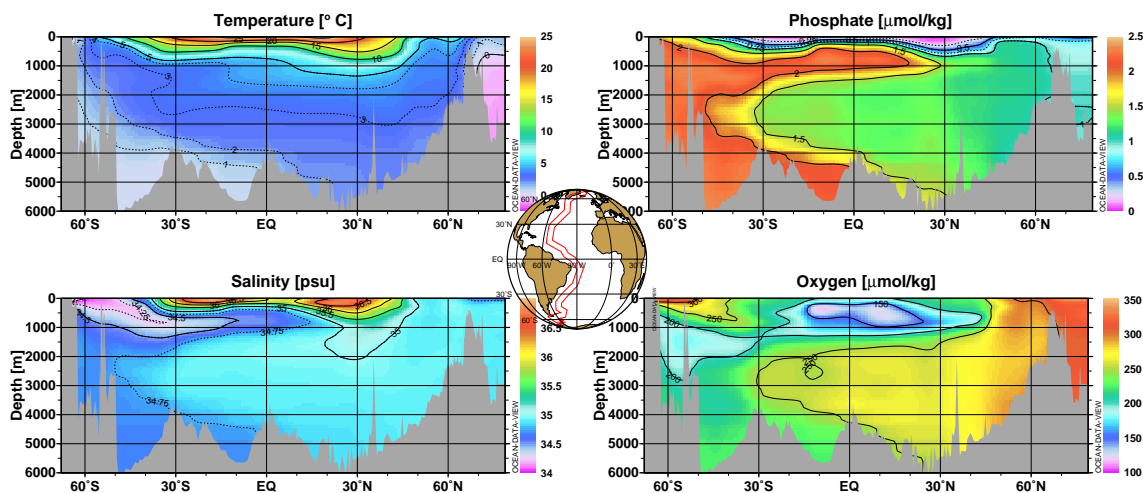


Figure 1.1: Temperature, salinity, phosphate, and oxygen concentrations along the west Atlantic GEOSECS (Geochemical Ocean Sections Study) section (Bainbridge, 1980)

The climatic influence on surface water characteristics can be clearly seen in the distribution of temperature and salinity. At low- and mid-latitudes (between ca. $40^{\circ}S$ and $40^{\circ}N$), surface temperature is high due to continuous insolation. Salinity is also high due to evaporation of fresh water. The temperature is continuously decreasing with depth down to temperatures below $0^{\circ}C$ whereas salinity shows a 'tongue' of minimum salinities at about 800m depth obviously generated at the surface in the Southern Ocean (south of ca. $50^{\circ}S$). This low-salinity water, which goes along with a slight depression in temperature, is associated with Antarctic Intermediate Water (AAIW) which spreads northwards in the Atlantic. Another distinct water mass is the Antarctic Bottom Water (AABW) which is associated with comparably low salinities and very low temperatures. These water masses are produced in the Southern Ocean by cooling of surface water and density changes due to freezing and melting of sea ice and ice shelf. Because the deep water masses store information about surface water properties and modification processes, distributions of temperature and salinity can be used to reconstruct ocean circulation. To further constrain ocean circulation, conservative tracers with known input rates at the ocean surface are also used, e.g. radiocarbon ^{14}C (Broecker et al., 1960) and chlorofluorocarbons CFC's (Bullister (1989), Roether (1996)). Comparing salinity, temperature, and phosphate concentrations reveals that high phosphate concentrations roughly coincide with Antarctic waters which are also rich in nitrate and silicate. The vertical gradients in phosphate distribution are relatively strong with concentrations approaching zero at the surface in low latitudes. This is not surprising since phosphate is involved in photosynthesis which takes place in surface waters and, especially in tropical and subtropical regions, all nutrients are depleted in the upper water column during primary production.

The phosphate distribution is influenced by physical processes (advection and diffusion) *and* biology and thus, phosphate is a non-conservative tracer of water masses.

Maximum phosphate concentrations are found in about 500m depth near the equator where oxygen shows a strong minimum. The differences between phosphate and oxygen store information about biogeochemical processes in the water column. At the surface, oxygen is produced during photosynthesis, and remineralization of sinking organic matter releases phosphate and nitrate whereas oxygen is used up. This 'apparent oxygen utilization' (AOU) is used to estimate degradation of organic carbon. These data thus indirectly contain information about particle fluxes.

However, vertical particulate fluxes are also directly observed using various techniques such as in-situ filtration of sea water or sediment traps which collect sinking particles in different water depths over longer periods. Particle concentrations in water column directly depend on surface particle production.

All together, property distributions and particle concentrations in water column not only reflect physical circulation but also processes modifying nutrients such as production of organic matter and subsequent degradation (see Section 1.1).

Biogeochemical processes are coupled to physical circulation. Thus, for a full understanding of nutrient cycling, physical and biogeochemical processes must be regarded. Since distributions of temperature, salinity, *and* dissolved nutrients contain information about the current field as well as about biogeochemical processes, oceanographers began to develop coupled physical/biogeochemical models. The progress in physical/biogeochemical modeling is outlined in Section 1.2.

1.1 The biological pump

Biogeochemical processes together with physical circulation control the cycles of nutrients in the water column and gas exchange of O_2 and CO_2 with the atmosphere. Biological processes in the upper water column are closely linked to physical circulation. Primary productivity (photosynthesis) not only depends on availability of light but also on the supply of nutrients due to advective and diffusive processes. In vast areas of the world ocean, surface waters are depleted in nutrients and silicate due to biological productivity. Sinking detritus remineralizes and transports nutrients into deeper water. Upwelling of deep water closes the cycle and supplies nutrients to the euphotic zone. The coupling of biogeochemical and physical processes is visualized in Figure 1.2, for a detailed process description see, e.g. (Lalli and Parsons, 1997):

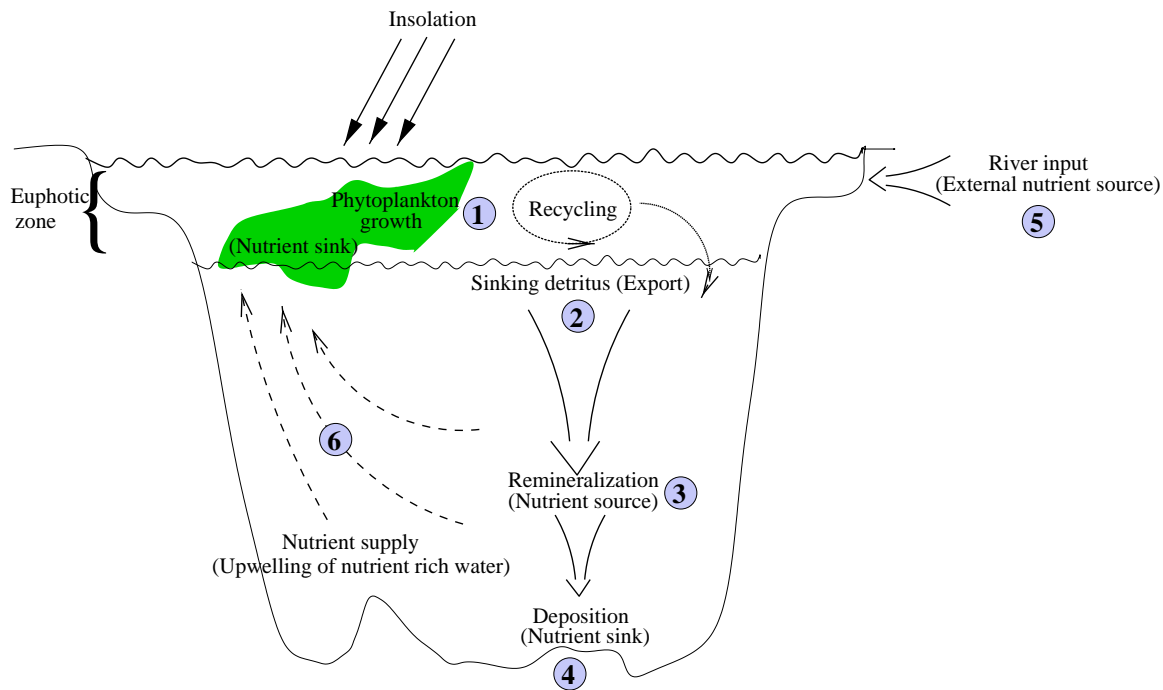


Figure 1.2: Schematic diagram of the biological pump in the ocean

Phytoplankton grows in the upper mixed layer of the ocean (1). Photosynthesis is either limited by light and/or by nutrients. During photosynthesis, dissolved nutrients as phosphate, nitrate, and inorganic carbon are consumed by growing phytoplankton cells. The most abundant species in temperate and high latitudes belong to the diatom group. Diatoms form frustules of amorphous silica (*Opal*) and so, silicate is consumed too. Other species (like coccolithophorides) form calcium carbonate ($CaCO_3$) frustules or no shells at all (for instance cyanobacteria). Carbon, phosphate, nitrate, and silica are depleted in surface waters, and especially near the equator concentrations are very low (see Figure 1.1). Total primary production is commonly named 'gross production'. Many efforts have been spent on the estimation of primary production (PP). Direct measurements of nitrate utilization, chlorophyll concentrations, oxygen saturation, pH, and others were assimilated for different maps of estimated primary production. The maps most commonly used are based on very heterogeneous data and were summarized by Berger (1989). Globally integrated primary production in these maps varies from 20 GtC/y to 27 GtC/y . In 1996, Antoine and Morel (1996) presented a new method to estimate total primary production from satellite chlorophyll measurements (NOAA, 1998) and "climatological fields" (Antoine and Morel (1996), Antoine et al. (1996)). In their new maps, integrated primary production was much higher than thought before ranging from 36.5 GtC/y to 45.6 GtC/y .

Primary production is partly already recycled within the euphotic zone supplying a standing stock of marine microorganisms. A part of planktonic detritus sinks towards the sea floor and appears as a loss of nutrients for the ecosystem in the euphotic zone. Consequently, this part of biomass is called 'export production' EP (2). The amount of exported particles is regionally variable and depends non-

linearly on primary production. Eppley and Peterson (1979) defined the 'f-ratio' which describes the ratio of export production to primary production (EP/PP). The f-ratio itself was found to depend on nitrate concentration, zoo-plankton grazing, seasonality, and more. In a review of Eppley (1989) the f-ratio varies from 0.06 (i.e. 6% of primary production is exported) in the oligotrophic open ocean areas to 1 (all primary production sinks out of the euphotic zone) during special spring bloom events. Eppley and Peterson (1979) estimated that for primary production between $20\text{GtC}/\text{y}$ and $45\text{GtC}/\text{y}$ about $3.4\text{GtC}/\text{y}$ to $4.7\text{GtC}/\text{y}$ is exported to the deep ocean.

The fate of sinking particles **(2)**, **(3)** is examined using sediment traps. An extensive discussion of sediment trap data is given in Section 4. From sediment trap data, in situ filtrations, and estimations of export production the vertical decrease of particle fluxes is calculated. The remineralization of particles increases nutrient concentrations in the deeper water column. At the sea floor, benthic organisms live on the supply of sinking detritus and remineralization continues, and so over large areas the bottom waters of the ocean bear highest nutrient concentrations.

A small amount of particles reaching the sea floor is buried in the sediments **(4)**. The accumulation of sediments is the only durable sink in the marine nutrient cycle. The total mass flux into the sediments is rather small compared to the other fluxes but the accumulated particles are almost the only information source of the marine geological history. Assuming that the cycle maintains in a steady state the nutrient sink at the sea floor must be compensated with external inputs (riverine **(5)** and/or aeolian).

The major part of export production 'pumped' into the deeper water column is remineralized during sinking. The deep waters get enriched with dissolved nutrients. The residence time of dissolved nutrients in the deeper water column depends on particle remineralization depth and on ocean circulation. Finally, the advective/diffusive upwelling of nutrient-enriched deep water **(6)** allows continuing primary (and export) production. Thus, ocean circulation becomes the engine of all marine biological activities because without upwelling of deep, nutrient-rich water, production would cease within weeks or months.

As already pointed out, the biological pump transports particulate organic carbon, calcite, and biogeneous silica towards the deep sea. Many studies focused on the effect of the biological pump on organic carbon. Organic carbon cycling is of special interest because of its relevance to climatic forecasts ("Greenhouse effect"). Global budgets are needed to estimate effects of anthropogenic CO_2 inputs into the atmosphere. The ocean is a huge reservoir for CO_2 . Depending on surface water properties the ocean appears as a source or sink for atmospheric CO_2 . Additional to physical/chemical transports in ocean circulation models, one needs to know the size of the biological pump (i.e., the amount of particles vertically transported). An example of the estimation of organic carbon cycling for the world ocean from Berger et al. (1989b) is shown in Figure 1.3.

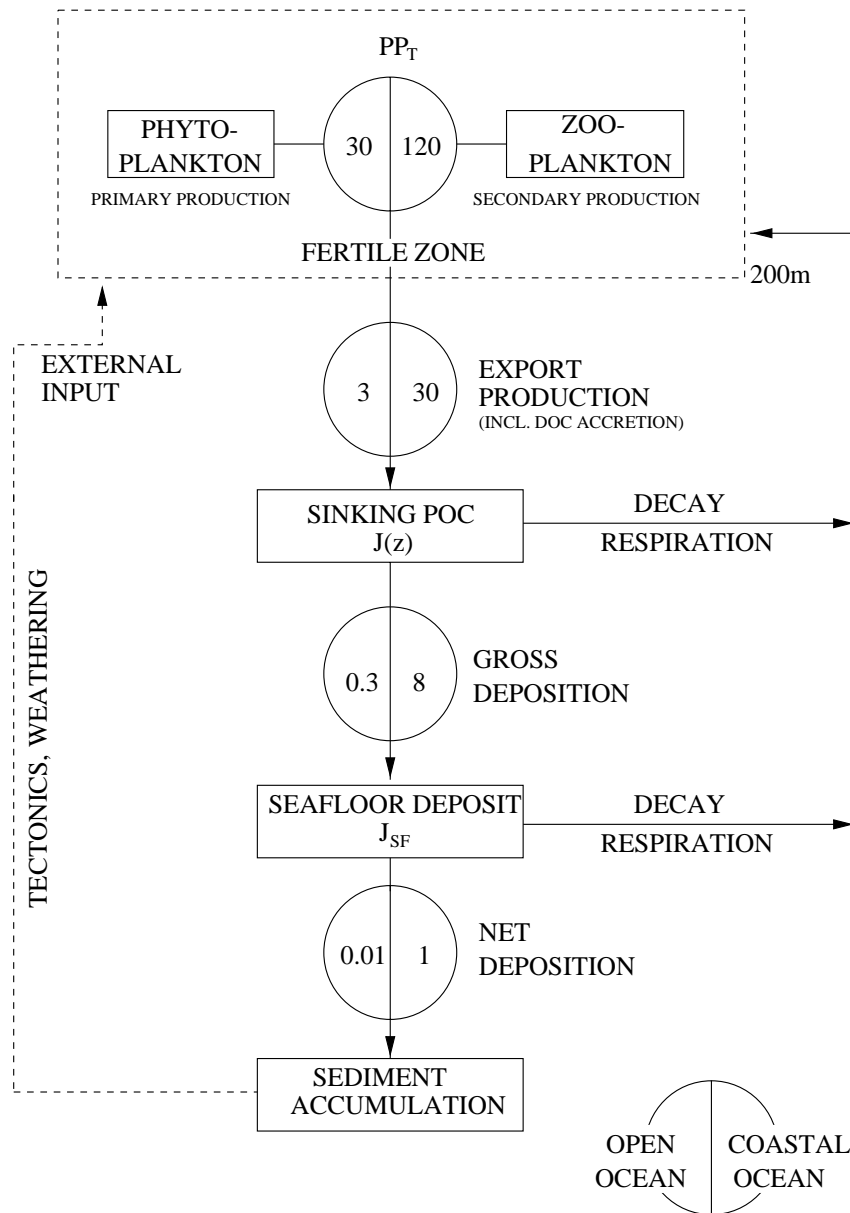


Figure 1.3: Fluxes of particular organic carbon in the world ocean from Berger et al. (1989b). Numbers denote fluxes in units $[\frac{gC}{m^2y}]$

On the left side of the circles in Fig.1.3, values for a typical open ocean environment are given and on the right side for coastal regions. Major parts of primary production are recycled within the euphotic zone and only 10% to 25% contribute to the particle flux $J(z)$. Sinking particles are remineralized and only 10% to 26% of export production reaches the sea floor. At the sediment-water-interface, redissolution continues resulting in a net deposition of 0.01 to $1\frac{gC}{m^2y}$ only. The biological pump delivers 0.03% to 0.8% of primary production to the sediment. The sum of particles removed from the water column is thus not very large but sediment accumulation is the *only* ultimate nutrient sink in the oceans.

Even if the total CO_2 removal into deep sea sediments is of minor importance com-

pared with the total amount of cycled carbon it is still important to provide estimates for carbon accumulation.

One goal of the work presented here is to test a new method to calculate accumulation rates of biogeous sediments from nutrient distributions.

As already pointed out, the estimates of primary production (and also export production) vary within a factor two. Further, the remineralization of sinking particles strongly depends on properties of individual particles (composition, morphology, size, etc.), sinking speed (residence time in water column) and properties of the surrounding water (under- and oversaturation, temperature, etc.). Suess (1980) proposed that the general form of particulate organic carbon fluxes J follows:

$$J \propto EP \frac{1}{z^\beta} \quad EP = \text{export production} \quad (1.1)$$

In the original form, the parameter β determining the depth of remineralization was equal to one but subsequent work showed that the parameter β is regionally variable. A summary was given by Bishop (1989). His work clearly shows the complex problem of determination of the degradation rates of organic matter. For different data sets and subsets, he presented eight equations with parameter β ranging from 0.5 to 1, i.e. the variation is huge. An overall valid parameterization for particle formation and redissolution is not yet found.

The present work aims at a better understanding of the variations of remineralization rates in the world ocean. As will be described later on, the work presented here determines remineralization scale lengths by means of nutrient budget calculations which will give new, independent estimates for β .

Bishop (1989) showed that productivity and degradation of biogeous particles are closely linked to oceanographic conditions. He developed simple, empirical rules to estimate fluxes. He also points out that by using the empirical rules, a full understanding cannot be achieved, especially where strong horizontal gradients exist (i.e. at the frontal systems and upwelling regions). It is thus clear that biogeochemical models *must* be linked to oceanographic models in order to understand global biogeochemical cycles.

1.2 Biogeochemical modeling

Global physical/biogeochemical models combine ocean circulation with biogeochemical processes determining consumption and redissolution of nutrients. Dissolved nutrients are used as non-conservative tracers with biogeochemical processes controlling nutrient transports together with the current field. Table 1.1 summarizes the (incomplete) history of progress in coupled oceanographic/biogeochemical modeling.

No.	Description	Citation	EP [GtC/y]
(1)	LSG, GFDL, Global inorganic carbon cycle, ^{14}C	(Maier-Reimer and Hasselmann, 1987), (Toggweiler, 1989a), (Toggweiler, 1989b)	—
(2)	HAMOCC1, Global inorganic and organic carbon cycle (POM, DOM, calcite)	(Bacastow and Maier-Reimer, 1990)	4.8
(3)	GFDL, global phosphate cycling (POM, POP)	(Najjar et al., 1992)	12-15
(4)	HAMOCC3, global cycling (POM, calcite, silicate)	(Maier-Reimer, 1993)	NG
(5)	GFDL, global cycling of phosphate and oxygen (POM, DOM, AOU)	(Anderson and Sarmiento, 1995)	NG
(6)	CCSR, global cycling (POM, calcite)	(Yamanaka and Tajika, 1996)	10
(7)	CCSR, global cycling (POM, DOM, calcite)	(Yamanaka and Tajika, 1997)	8
(8)	HAMOCC1, North Pacific adjoint (POM, calcite)	(Matear and Holloway, 1995)	—
(9)	Global adjoint (POM, calcite, silicate)	(Schlitzer, 1999a)	NG

Table 1.1: “History” of biogeochemical modeling (incomplete). For further explanation see text.

Abbreviations:

AOU: Apparent Oxygen Utilization, CCSR: Center for Climate System Research, DOM: Dissolved Organic Matter, DOP: Dissolved Organic Phosphorus, EP: Global POM export, GFDL: Geophysics Fluid Dynamics Laboratory, HAMOCC: Hamburg Ocean Carbon Cycle Circulation Model, LSG: Large Scale Geostrophic, NG: Not given, POM: Particulate Organic Matter

The first full 3D circulation model with cycling of inorganic carbon was published 1987 by Maier-Reimer and Hasselmann (1). Their model treated inorganic carbon as a passive tracer (no sources and sinks) in the ocean. At the surface, CO_2 flux was calculated using chemical interaction rates with the atmosphere. The purpose of that work was to understand the storage properties of the ocean and to determine the ocean response to increasing CO_2 concentrations in the atmosphere. One conclusion was that the model must be extended by the “biological pump” to get more realistic values of surface CO_2 partial pressure.

In 1990, the model was extended by Bacastow and Maier-Reimer with organic carbon cycling due to export production and remineralization of organic matter and calcite ($CaCO_3$) (2). Nutrients, alkalinity, and CO_2 are transported downwards in two fractions: organic soft tissue (C_{org}) and calcite ($CaCO_3$). New production was modeled using surface phosphate concentrations and Michaelis-Menten kinetics with an additional light limiting factor (depending on latitude). C_{org} is remineral-

ized with an exponential function (fluxes decrease $\propto \exp(-z)$, z = water depth) and $CaCO_3$ remineralization rates were adjusted to give reasonable alkalinity distributions. The current field was not changed in the model runs and resulting nutrient distributions were generally reasonable but locally deviations to measurements were quite large. It was discussed that the deviations are most likely due to unrealistic features in the current field.

Najjar et al. (1992) extended the 3D global circulation model of Toggweiler (1989) to include vertical biogenic carbon fluxes (3). New production calculations were based on surface phosphate concentrations and remineralization followed exponential functions and a power law according to Martin et al. (1987) (fluxes decrease $\propto 1/(z^{0.858})$, c.f. Section 1.1 and Martin et al. (1987)). Both experiments showed some systematic deviations which led to the introduction of dissolved organic matter (DOM), which was also included in Maier-Reimer's model (4). Advection of DOM and new remineralization rates for DOM helped to produce better phosphate distributions, especially in the equatorial Pacific. In the model of Najjar et al. (1992), optimum results were obtained if DOM was clearly dominating particulate organic material (POM) with a relation of 4:1. Astonishingly, the reduction of particulate organic matter led to the conclusion that sediment traps are *overestimating* particle fluxes (c.f. discussion in Section 4). Furthermore, the experiments with particles only (no DOM) showed better agreement with measurements of benthic fluxes of organic matter. Anderson and Sarmiento (1995) showed later that the contribution of DOM was probably overestimated in the GFDL (Geophysics Fluid Dynamics Laboratory) model of Najjar et al. (1992) and that the discrepancies are most likely caused by shortcomings of the current field (5). In addition to phosphate concentrations they used 'apparent oxygen utilization' (AOU) as a tracer for remineralization of organic matter. From AOU distributions they stated that the remineralization depth scale derived from sediment trap data appears too shallow (the model results indicate that main remineralization occurs deeper).

Yamanaka and Tajika (1996) tried to find the best parameterization of flux equations (power law and exponential) comparing 28 case studies with respect to the resulting phosphate concentrations. Contrary to the results of Najjar et al. (1992) they came up with the conclusion that the optimum parameters are well in the range determined by particle flux measurements and that differences might be due to a different current field (6). In an extension of that model they implemented also DOM fluxes which improved model phosphate fields but reduced POM export production (7).

The new version of HAMOCC1 with an improved current field (esp. deep water formation) and DOM was presented by Maier-Reimer (1993) (4). In this version, HAMOCC3, not only C_{org} and $CaCO_3$ were determined but biogeneous silica (*Opal*) was modeled whereas the separate treatment of DOM was abandoned. Shell material was divided into $CaCO_3$ and *Opal* with limitations of *Opal* production (availability of dissolved silica). Organic carbon remineralization was changed to a power law (Martin et al., 1987), $CaCO_3$ and *Opal* were remineralized with exponential functions (1/e-fold depth 2km and 10km, respectively). A new feature in HAMOCC3 was a 10cm sediment layer where particulate material is accumulated. HAMOCC3 generally produces realistic biogeochemical tracer distributions but deviations re-

main in areas with strong hydrographic gradients (e.g. upwelling regions). The local discrepancies are discussed to depend most likely on shortcomings of the current field.

So far, these coupled physical/biogeochemical models were improved with respect to the current field and parameterizations of biogeochemical processes. Nevertheless, the agreement of model nutrient fields and data was satisfactorily on a global scale only. Remineralization processes are still a matter of discussion. Also, integrated export of POM is not a fixed quantity but varies from 4.8 GtC/y to 15 GtC/y (c.f. Tab.1.1). Most differences (model fields to observations *and* differences between different models) are probably due to the current field. In all models discussed above, the current field was calculated *independently* of biogeochemical processes. A solution of a circulation model was “frozen” and calculation of biogeochemical processes were performed using the -unchanged- current field. The results show clearly that distributions of biogeochemical tracers not only depend on the parameterization of the underlying processes but that a minor change in the current field has strong impact on nutrient distributions.

With this background, Matear and Holloway (1995) developed an adjoint model for the North Pacific using the LSG (Large Scale Geostrophic) solution of Maier-Reimer’s HAMOCC1 model (8). The adjoint formalism is widely used to derive parameters from observations (e.g. Tarantola (1987), Wunsch (1983), Wunsch (1984)). In Matear and Holloway’s (1995) work, the adjoint model was used to vary velocities, export production rates, and remineralization scale lengths to match observations of dissolved phosphate. Data of dissolved phosphate were assimilated and the adjoint formalism was implemented similar as described by Schlitzer (1993). Optimization of the biogeochemical parameters alone (frozen current field) showed that, in agreement with Anderson and Sarmiento’s (1995) results, optimum remineralization scale lengths were indeed deeper than derived from sediment traps. Further, they re-confirmed that without changing the current field, a particle only model (no DOM) could not satisfactorily reproduce measured phosphate concentrations. A very small variation of the current field led to much better agreement of phosphate fields and data. Resulting new production showed strong resemblance with observations.

All together this overview makes clear that dynamical ocean models including biogeochemical models react very sensitively to changes in the current field. This is not surprising because productivity primarily depends on nutrient concentrations in surface waters. The nutrients available for phytoplankton growth are transported to the surface layer by advective/diffusive transports (upwelling of nutrient-rich deep water). In most circulation models, upwelling is generated from the divergence of horizontally moving water masses, i.e., as the difference between large amounts of water horizontally entering and leaving a model box. Very small changes in the horizontal current field can give rise to dramatic changes in vertical velocities and so also in nutrient supply. The results of Matear and Holloway (1995) nicely demonstrated the very critical relation between current velocities and resulting nutrient cycling and that the adjoint method can be powerfully used to solve major problems of the dynamic models described above.

A disadvantage of adjoint models is that they are not prognostic. The processes are optimized to give results in agreement with measurements and/or a priori knowl-

edge (see Section 2). Calculating the current field and/or biogeochemical processes without data is thus not possible and so the modeling of a paleo- or future -ocean is excluded.

The adjoint method is rather a diagnostic tool to quantify present processes. For instance, the amount of Antarctic Bottom Water (AABW) formation which is needed to produce temperature and salinity distributions found in the Atlantic (c.f Fig. 1.1) is a classical adjoint problem.

It was already pointed out that biogeochemical fluxes in the world ocean are rather complicated and not easily described by unique values valid for the global ocean (c.f Section 1.1). On the other hand, many data of temperature, salinity, dissolved nutrients and silicate exist. The adjoint method thus can be used to derive process rates (physical *and* biogeochemical) from these data. The results from adjoint modeling might help to understand regional characteristics of biogeochemical processes. These results then can be used to further refine dynamical models.

Schlitzer (1999) presented a global adjoint model where particle cycling optimized for organic carbon, calcite, and opal (9). In his model, export production rates and remineralization rates are optimized *together* with the physical current field to reproduce temperature, salinity, and nutrient measurements in the world ocean. Resulting property distributions were indeed in close agreement to data.

The presented work focuses on the information stored in distributions of temperature, salinity, nutrients, and silicate. The basic tool used in this work is the adjoint model from Schlitzer (1999). The method is outlined in Section 2 and general model results are presented in Section 3.

Two major modifications of Schlitzer's (1999) model are presented in this work.

- For the first time, a detailed comparison of model fluxes with independent flux measurements is performed. Vertical model fluxes of particulate biogeochemical matter are compared with particle fluxes collected in sediment traps. An extension of the model now allows to force model particle fluxes to reproduce sediment trap data. Sediment trap data are used as new, independent (from distributions of dissolved nutrients) variables recording biogeochemical processes. Assimilation of sediment trap data and results are given in Section 4.
- The model was extended to yield not only vertical particle fluxes in water column but also fluxes through the water-sediment interface. Sediment accumulation rates are calculated from nutrient budgets. Sediment accumulation does not play a major role in global biogeochemical cycles but is, as mentioned above, one interface of the marine system with the lithosphere and is an important boundary condition if one wants to estimate global sinks and sources. It was to be tested whether the adjoint model can give reasonable values for mean sediment accumulation.

Implementation and results for this new feature are given in Section 5

The experiments presented here showed that particle fluxes in the Southern Ocean are 'atypical' when compared to other areas. Results from adjoint modeling and independent studies near the Polar Front and in the Weddell Sea are compared in Section 6.

2 The adjoint model

In this work, the adjoint model is used to calculate the 3D large scale ocean circulation and biogeochemical fluxes of nutrients and silicate. The model was originally developed by Schlitzer (1993) and the first version was set up to calculate the ocean circulation, air-sea fluxes of heat and fresh water, and mixing coefficients in the Atlantic. An extensive description of the model and a comparison with other methods is given in (Schlitzer, 1995). The basic idea is to make use of the information stored in distributions of temperature and salinity to reconstruct ocean processes. Ocean currents are calculated inversely to reproduce hydrographic data. His model determines mean velocities together with air-sea heat and fresh water fluxes and mixing coefficients which give distributions close to data. The model was expanded by de la Heras and Schlitzer to a global domain (de la Heras and Schlitzer, 1999) and Schlitzer (1999) added vertical biogenic particle fluxes. Physical and biogeochemical processes are calculated using property distributions of the world ocean. Processes generating the distributions of temperature, salinity, nutrients, and silicate are parameterized to reproduce measurements.

An important feature of this model is the conservation of mass, heat, salt, and tracers. The exact satisfaction of budget equations allows the computation of cycles of phosphate, nitrate, and silicate:

For a stationary, mean ocean circulation, the transport of nutrients due to advection and diffusion processes is in equilibrium with vertical particulate fluxes. I.e., assuming steady state, the sum of all transports amounts to zero. Calculating the mean advective/diffusive transports of nutrients allows the determination of the compensating vertical particulate fluxes. Particle fluxes J are calculated with equations of the form

$$J(x, y, z) = \alpha(x, y)z^{-\beta(x, y)} \quad z = \text{water depth.} \quad (2.1)$$

The parameters α, β are regionally variable and optimized by the model to compensate for transports caused by advection and diffusion of dissolved nutrients.

The calculation of the geostrophic current field is mainly based on temperature and salinity data, vertical particle fluxes are mainly controlled by data of dissolved nutrients. Biogenic particles are modeled as sources and sinks of dissolved nutrients: Dissolved nutrients are removed from the water column during particle formation (phytoplankton growth in the euphotic zone), whereas remineralization of biogeneous particles releases nutrients (during sinking and early diagenesis at the sea floor). With the adjoint model, the rates for particle production, remineralization, and accumulation of surface sediments are determined such that particle fluxes are in agreement with dissolved nutrients. Also, the model can be forced to reproduce sediment trap data.

Further constraints for the model are discussed in Section 2.8.

2.1 Basics

The adjoint model optimizes parameters for a set of model equations such that model property fields are close to data. The data base used in this model is described in Section 2.3. A principal sketch of the model setup is shown in Fig.2.1.

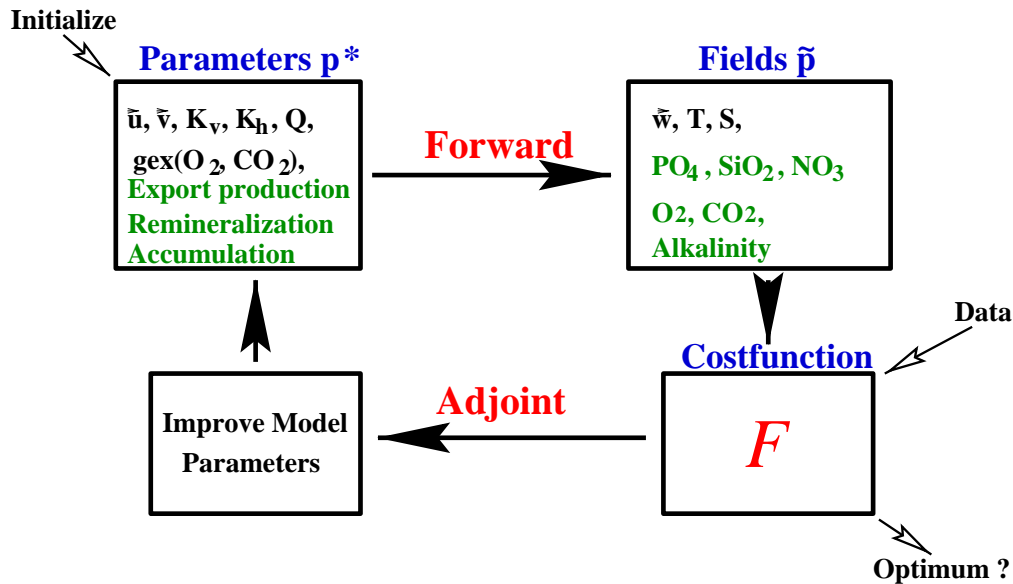


Figure 2.1: Schematic sketch of the adjoint model

Initially, a 3D model grid is set up to represent the area of interest with desired resolution. Within this grid, all independent model parameters p^* are initialized. For the current field, the model is initialized by setting horizontal velocities \vec{u}, \vec{v} for all model boxes, horizontal and vertical mixing coefficients K_h, K_v , and surface heat fluxes Q . Particle fluxes are initialized by setting rates for export production, remineralization and accumulation of surface sediments for each water column. In the so-called forward mode, the model equations are solved (c.f. Section 2.5). The resulting fields of vertical velocities \vec{w} , temperature T , salinity S , and dissolved nutrients $\text{PO}_4, \text{SiO}_2, \text{NO}_3, \text{O}_2, \text{CO}_2$, and *Alkalinity* are called dependent parameters \tilde{p} . The property fields are then compared with data and all deviations are accumulated in a costfunction $F(p^*, \tilde{p})$ which depends on all independent and dependent parameters. Additionally, $F(p^*, \tilde{p})$ contains penalty terms for deviations from geostrophic shear, smoothness constraints etc. (see, e.g. Schlitzer (1993), Schlitzer (1995), Thacker (1988)). The complete set of penalty terms of costfunction $F(p^*, \tilde{p})$ in this study is listed in Section 2.8.1. The costfunction is a scalar function which measures the quality of the model solution. The smaller the costfunction, the better the model complies with the desired features (terms in $F(p^*, \tilde{p})$). All terms in $F(p^*, \tilde{p})$ are multiplied with weight factors, allowing to align the individual terms for special demands. In this model, the agreement of model distributions and data of temperature, salinity, and dissolved nutrients was taken as the main criterion for a 'good' solution. A smaller costfunction indicates that the model solution yields

property fields which are closer to measurements and thus more realistic. A smaller costfunction is calculated in the 'adjoint mode', where new parameters p^* are determined. This is done by calculating the gradient of $F(p^*, \tilde{p})$ with respect to the independent model parameters and following the negative gradient in parameter space. Thus, a model solution is obtained which is 'better' in the sense, that model properties closer accomplish with the features defined in the costfunction. Using a quasi-Newton algorithm, this procedure is iterated and guarantees a decreasing costfunction. The iteration is repeated until $F(p^*, \tilde{p})$ is at its minimum or model features are satisfyingly.

Finally, the model solution gives the mean, large-scale ocean circulation together with mean particle fluxes minimizing the costfunction $F(p^*, \tilde{p})$.

2.2 Optimization

Formally, the minimization of $F(p^*, \tilde{p})$ is identical to constrained optimization. In this model the well known method of Lagrangian Multipliers is used (e.g. Tarantola (1987)).

Costfunction $F(p^*, \tilde{p})$ is to be minimized under constraints:

$$E_k = 0 \tag{2.2}$$

(budget equations, c.f. Section 2.5). Equations (2.2) are fulfilled exactly and are named 'hard constraints'.

$F(p^*, \tilde{p})$ can be imagined as a surface in an orthogonal space of dimension $N_{(p^*)}$ (number of independent parameters). Constraints (2.2) are implicit parameter curves. Projection of these curves on the surface $F(p^*, \tilde{p})$ gives all points in space which fulfill the hard constraints exactly. The subset of points defined by these equations span the subspace of possible parameter values p^* . This subspace has dimension N_{p^*} . The method is visualized with a two-dimensional example. In Fig. 2.2, $F(x, y)$ is to be minimized under the constraint $E(x, y) = 0$. The implicit curve has an image $E'(x, y)$ on the plane $F(x, y)$ and another image $E''(x, y)$ in the x-y-plane. All points on either curves fulfill the constraint given by $E(x, y) = 0$. Minimum of $F(x, y)$ under constraint $E(x, y) = 0$ is a point on the implicit curve $E(x, y)$ which gives the smallest value of $F(x, y)$.

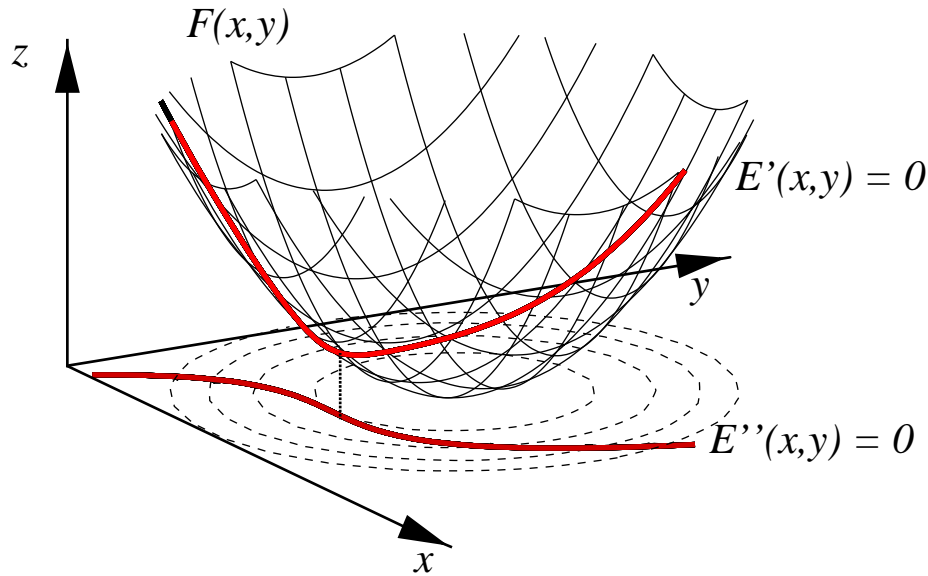


Figure 2.2: Example functions for constrained optimization

Calculating $F(x, y) = z = \text{const.}$ gives isolines on the plane $F(x, y)$ and curves $F(x, y) - z = 0$ in the x-y-plane. One particular curve $F(x, y) - z_0 = 0$ touches the curve $E''(x, y)$ at the minimum of $F(x, y)$ under constraint $E(x, y)$. At this point, the tangents (and so the derivatives within the x-y-plane) of E'' and $F(x, y) - z$ are equal. Thus, the gradient becomes

$$a = -\frac{E_x(x, y)}{E_y(x, y)} = -\frac{F_x(x, y)}{F_y(x, y)}. \quad (2.3)$$

From Equation (2.3) directly follows that nominator and denominator are proportional:

$$E_x(x, y) = -\lambda F_x(x, y) \quad \text{and} \quad E_y(x, y) = -\lambda F_y(x, y). \quad (2.4)$$

The coefficient λ is called **Lagrangian multiplier**.

The **Lagrangian** L is defined as

$$L(x, y, \lambda) = F(x, y) + \lambda E(x, y). \quad (2.5)$$

Note that the Lagrangian is a function of x, y , and λ .

The minimum of L is given where all partial derivatives vanish:

$$L_x(x, y, \lambda) = F_x(x, y) + \lambda E_x(x, y) = 0 \quad (2.6)$$

and

$$L_y(x, y, \lambda) = F_y(x, y) + \lambda E_y(x, y) = 0. \quad (2.7)$$

$$L_\lambda(x, y, \lambda) = E(x, y) = 0. \quad (2.8)$$

(2.6) and (2.7) are identical with (2.4), and (2.8) reveals the constraint $E(x, y) = 0$. Thus, at minimum of $L(x, y, \lambda)$, $F(x, y)$ is minimal, too.

Analogous considerations yield the n-dimensional extension of costfunction $F(p^*, \tilde{p})$

under constraints $E_k(p^*, \tilde{p})$. The partial derivatives $\partial/\partial p^*$ and $\partial/\partial \tilde{p}$ of $F(p^*, \tilde{p})$ and $E(p^*, \tilde{p})$ give the relations

$$\frac{F_{p_i^*}(p_i^*, \tilde{p}_j)}{F_{\tilde{p}_j}(p_i^*, \tilde{p}_j)} = \frac{E_{k_{p_i^*}}(p_i^*, \tilde{p}_j)}{E_{k_{\tilde{p}_j}}(p_i^*, \tilde{p}_j)} \quad k \in [1, n_e] \quad (2.9)$$

with n_e = number of constraints. Coefficients λ given by

$$F_{p_i^*}(p_i^*, \tilde{p}_j) = -\lambda_k E_{k_{p_i^*}}(p_i^*, \tilde{p}_j) \quad (2.10)$$

and

$$F_{\tilde{p}_j}(p_i^*, \tilde{p}_j) = -\lambda_k E_{k_{\tilde{p}_j}}(p_i^*, \tilde{p}_j). \quad (2.11)$$

yield the **Lagrangian**

$$L = F + \sum_{k=1}^{n_e} \lambda_k E_k. \quad (2.12)$$

Equation (2.12) again reveals that equations (2.10) and (2.11) describe the partial derivatives of the Lagrangian L with respect to parameters p_i^*, \tilde{p}_j at a stationary point $L' = 0$:

$$L_{p_i^*} = F_{p_i^*}(p_i^*, \tilde{p}_j) + \lambda_k E_{k_{p_i^*}}(p_i^*, \tilde{p}_j) = 0 \quad (2.13)$$

$$L_{\tilde{p}_j} = F_{\tilde{p}_j}(p_i^*, \tilde{p}_j) + \lambda_k E_{k_{\tilde{p}_j}}(p_i^*, \tilde{p}_j) = 0 \quad (2.14)$$

Again, differentiation with respect to λ_k reveals constraints $E_k = 0$:

$$L_{\lambda_k} = E_k = 0 \quad (2.15)$$

A stationary point (a vector $[p^*, \tilde{p}]$) of $L(p^*, \tilde{p}, \lambda)$ is stationary in $F(p^*, \tilde{p})$, too. Equations (2.13) and (2.14) are called **adjoint equations**. Finding the minimum of $F(p^*, \tilde{p})$ is equivalent to solving Equations (2.13), (2.14), and (2.15) at the same time.

In practice, a minimum value of costfunction $F(p^*, \tilde{p})$ is found iteratively:

In a first step, Equation (2.14) is solved for the Lagrange multipliers by setting the partial derivatives $L_{\tilde{p}_j}$ to zero. The λ_k are then introduced in Equation (2.13). This gives the gradient $F_{p_j^*}$ with respect to the independent model parameters. It should be noted here that this algorithm guarantees that costfunction $F(p^*, \tilde{p})$ decreases but the model does not necessarily converge to a global minimum. As in most quasi-gradient algorithms, the nearest minimum is found. Depending on the 'roughness' of costfunction $F(p^*, \tilde{p})$, this minimum can be quite different from the global minimum.

2.3 Data and model geometry

The most important terms in $F(p^*, \tilde{p})$ require closeness of model fields of temperature, salinity, and dissolved nutrients to data. Schlitzer (in press) compiled a huge amount of measurements for comparisons in the model. The data set includes more than 14,000 stations of measurements of dissolved phosphate and more than 25,000 top-to-bottom profiles of temperature and salinity. The overall spatio-temporal data

coverage is good except in the polar regions where data are biased towards summer values. Fig. 2.3 shows station points of profiles of temperature, salinity, and nutrients.

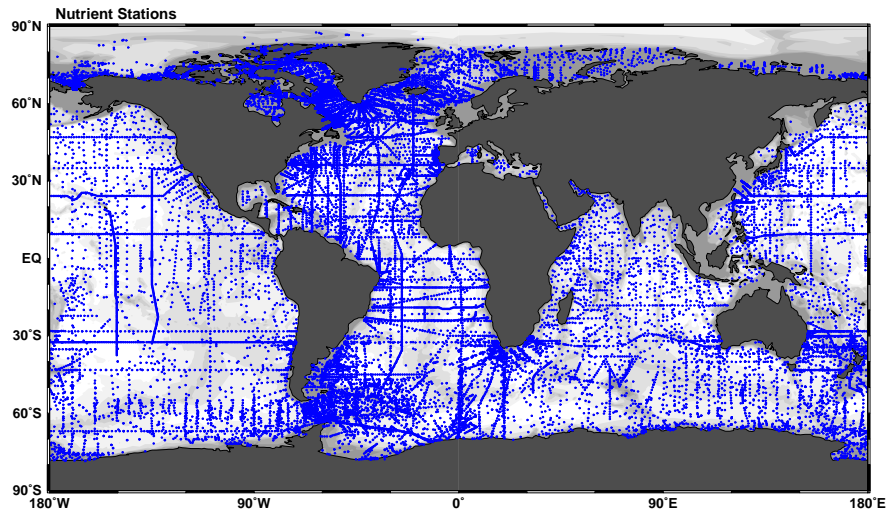


Figure 2.3: Global distribution of stations with nutrient data

Fig. 2.4 shows the model grid used in this work. The grid is non-uniform for the global model domain. Resolution varies from 2.5×2 degrees to 60×4 degrees at the very high latitudes in the north with a default of 5×4 degrees in most regions of the world ocean. The model grid allows high resolution calculation of currents and biogeochemical processes in areas with strong currents, pronounced upwelling, and/or high property gradients without having high computational costs within the whole model domain.

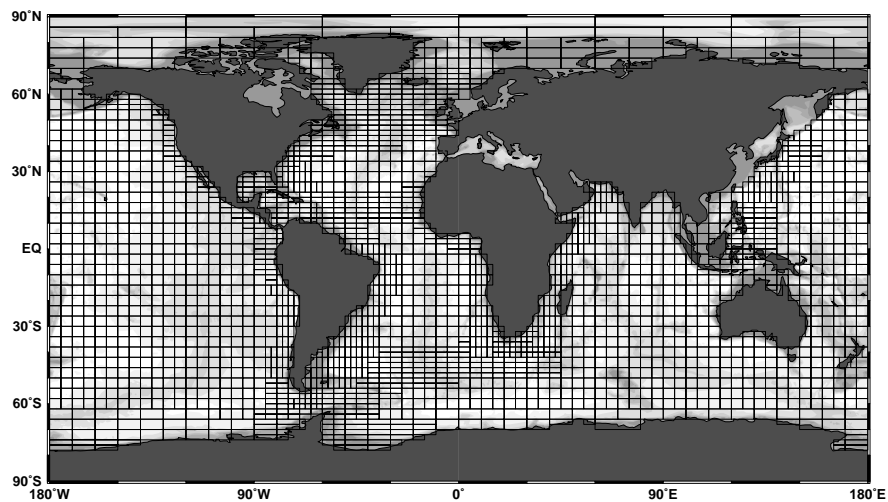


Figure 2.4: Model grid

The vertical resolution decreases top to bottom. At the surface, layer thickness is 61m which increases to about 500m at the deepest layers (deeper than ≈ 4000 m). Individual layer depths are 0, 61, 133, 219, 320, 436, 568, 719, 888, 1078, 1289, 1522, 1779, 2060, 2368, 2702, 3064, 3456, 3879, 4332, 4819, 5339, 5895, 6486, 7115, and 7783 meters, respectively.

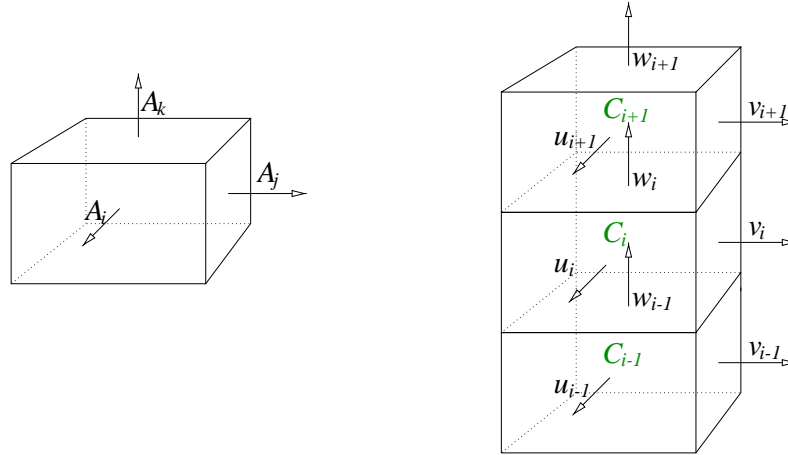


Figure 2.5: Definitions within the model grid

Fig. 2.5 shows definitions within the model grid. $A_{i,j,k}$ are signed box surfaces. Due to the irregular grid, boxes can have more than 6 surfaces. This is important for the setup of the advection/diffusion matrix (see Section 2.5). Horizontal and vertical velocities are defined at the corresponding surface, whereas concentrations are defined in the center of a box (Arakawa C-grid).

2.4 Model parameters

In the adjoint model, independent parameters p^* are varied to minimize costfunction $F(p^*, \tilde{p})$ as described above. The independent model parameters defined on the grid described in Section 2.3 are summarized in Table 2.1. The independent 'physical' model parameters p_{phys}^* are horizontal velocities \vec{u}, \vec{v} , horizontal and vertical mixing coefficients K_h, K_v , surface heat fluxes Q , and gas exchange rates at the surface for O_2 and CO_2 .

Independent parameters p_{bio}^* for the biological processes are export-, remineralization- and accumulation rates of biogeous particles (α, β, s) . Parameters α, β for export production and remineralization correspond to export production and remineralization rates mentioned in Section 1.1, the accumulation of biogeous surface sediments s is described further below.

Independent parameters p^*	Meaning
\vec{u}, \vec{v}	horizontal velocities, defined on all vertical box boundaries
K_h, K_v	horizontal and vertical mixing coefficients, globally constant
$gex(O_2, CO_2)$	gas exchange rates at sea surface, defined for each column
Q	surface heat fluxes, defined for each column
α, β, s	parameters determining vertical particle fluxes, defined for each column

Table 2.1: Independent model parameters

The parameters p_{bio}^* are calculated for C_{org} , $CaCO_3$, and *Opal* separately. The vector of independent model parameters becomes:

$$p^* = p_{phys}^* + p_{bio}^*. \quad (2.16)$$

These parameters define a 3D current field and a 2D field of gas exchange and vertical particle fluxes on the grid shown in Fig.2.4.

The independent model parameters together with hard constraints (see Equations (2.18) below), namely budget equations for mass, heat, salt, and nutrients, yield the dependent parameters \tilde{p} . Within the whole model domain, property fields of temperature, salinity, and dissolved nutrients (all \tilde{p} 's) are determined by solving a linear system

$$\mathcal{A}\vec{c} = \vec{q} \quad (2.17)$$

where \mathcal{A} is an advection/diffusion matrix, \vec{c} denotes any property of interest and \vec{q} source and/or sink terms of that property, respectively. The setup of the advection/diffusion matrix \mathcal{A} is described in Section 2.5, sources and sinks in subsequent Sections 2.6 and 2.7.

The dependent parameters \tilde{p} are fully deterministic variables which automatically change during the optimization because the independent parameters p^* are modified. Table 2.2 summarizes all modeled variables (dependent parameters).

Dependent parameters \tilde{p}	Meaning
\vec{w}	vertical velocity, results from mass conservation, at surface identical with evaporation and precipitation
$PO_4, NO_3, SiO_2, TALK$	result from advection/diffusion, and biogenic particle fluxes
$O_2, \sum CO_2$	result from advection/diffusion, biogenic particle fluxes, and air-sea exchange rates

Table 2.2: Dependent model parameters

2.5 Advection-/diffusion matrix

The budget equations for mass, heat, salinity, and dissolved nutrients are fulfilled exactly. The hard constraints $E(p^*, \tilde{p})$ are formulated with equations

$$E_k = 0. \quad (2.18)$$

The conservation of mass becomes

$$E = \sum_i A_i u_i + \sum_j A_j v_j + \sum_k A_k w_k = 0. \quad (2.19)$$

Advection and diffusion of any property c for each box leads to steady state form of equations::

$$\begin{aligned} E = & \sum_i A_i \left(u_i c_i^* - \frac{K_h \Delta c_i}{L} \right) + \\ & \sum_j A_j \left(u_j c_j^* - \frac{K_h \Delta c_j}{L} \right) + \\ & \sum_k A_k \left(w_k c_k^* - \frac{K_v \Delta c_k}{L} \right) - q = 0. \end{aligned} \quad (2.20)$$

Here, $A_{i,j,k}$ are signed box surfaces (c.f. Fig. 2.5), Δc denotes the difference concentration of two adjacent boxes, and L measures the distance between box centers.

To compute the advective term, one has to know the concentration *at the box surface*, where the velocity is defined. Therefore, a weighted-mean scheme is used: The mean concentration $c_{i,j,k}$ for velocities $\vec{u}, \vec{v}, \vec{w}$ becomes

$$c^* = f_u c_u + (1 - f_u) c_d \quad (2.21)$$

Here, c_u is the concentration in the 'upwind box' and c_d is the concentration in the 'downwind box'. According to Schlitzer (1999), in this model, a factor $f_u = 0.7$ was chosen. Consequences of the choice of different upwind factors are discussed in (Schlitzer, 1995).

Summation is over all box boundaries and the number of box surfaces is not equal for all boxes due to the irregular model grid (c.f. Section 2.3). q denotes the source term (resp. sink term) for a property in a box.

At the surface, O_2 and CO_2 fluxes are calculated. Sinks of dissolved nutrients (formation of particles) are located in the two uppermost boxes (the euphotic zone), sources of dissolved nutrients (rem mineralization of particles) are set in the underlying water column. The exact definition of biogeochemical sources and sinks is given in Section 2.7.

All equations (2.20) build the matrix \mathcal{A} representing the model (Equation (2.17)):

$$\mathcal{A}\vec{c} = \vec{q}$$

The matrix elements of \mathcal{A} contain horizontal and vertical mixing coefficients and velocities and build partly the vector of independent model parameters p^* (c.f. Equation (2.16)). Remaining independent parameters of p^* give surface heat fluxes, gas exchange rates, and biogeochemical fluxes. These parameters define the source/sink terms q and contribute to the right hand side of equations 2.17 only. This has the advantage, that the same advection/diffusion matrix \mathcal{A} can be used for all properties (phosphate, silicate, salinity, etc.).

The solution of equations (2.17) yields the dependent parameters \tilde{p} , namely vertical velocities, temperature, and concentrations of salinity, phosphate, nitrate, silicate, alkalinity, oxygen, and carbon dioxide.

The vertical velocities \vec{w} are calculated as follows: At the bottom, vertical velocity is zero. The divergence resulting from independent parameters \vec{u}, \vec{v} (Equation (2.19)) gives the velocity \vec{w} at the upper box surface. Vertical velocities are calculated successively bottom to top. At the sea surface, vertical velocities represent evaporation and precipitation, respectively.

Once all velocities are calculated, solution of (2.17) gives the distribution of all other properties.

The dependent model parameters become

$$\tilde{p} = \tilde{p}_{phys,bio} = [\vec{w}_{n_b}, T_{n_b}, S_{n_b}, PO_{4,n_b}, NH_{4,n_b}, SiO_{2,n_b}, O_{2,n_b}, CO_{2,n_b}, TALK_{n_b}]. \quad (2.22)$$

The number of dependent parameters becomes $9 \times n_b$ ($n_b =$ number of boxes) Combining the independent (Equation. (2.16)) and dependent (Equation. (2.22)) parameters gives the complete model vector

$$\vec{p} = [p^*, \tilde{p}]. \quad (2.23)$$

Together with the model grid, this vector is a full description of a model solution (a model state).

2.6 Gas exchange and heat flux

Gas exchange is calculated at the surface for O_2 and CO_2 . A positive flux J (into the atmosphere) manifests in a sink of O_2 and/or CO_2 , a negative flux (into the ocean) in a source of gas in the top box n_t of a water column.

$$q_{n_t} = -J(O_2, CO_2) \quad (2.24)$$

Analogous, surface heat flux appears as source (or sink, respectively) of heat in top boxes.

$$q_{n_t} = -J(Q) \quad (2.25)$$

2.7 Model particle fluxes

Property fields of dissolved nutrients are calculated with the advection/diffusion matrix and biogeochemical sources and sinks:

$$\mathcal{A}\vec{c} = \vec{q}$$

Here, \mathcal{A} is the advection/diffusion matrix (c.f. Section 2.5), \vec{c} is the concentration vector of the property of interest and \vec{q} the corresponding source term (which is negative for sinks). Sources describing the particle fluxes resolve as follows:

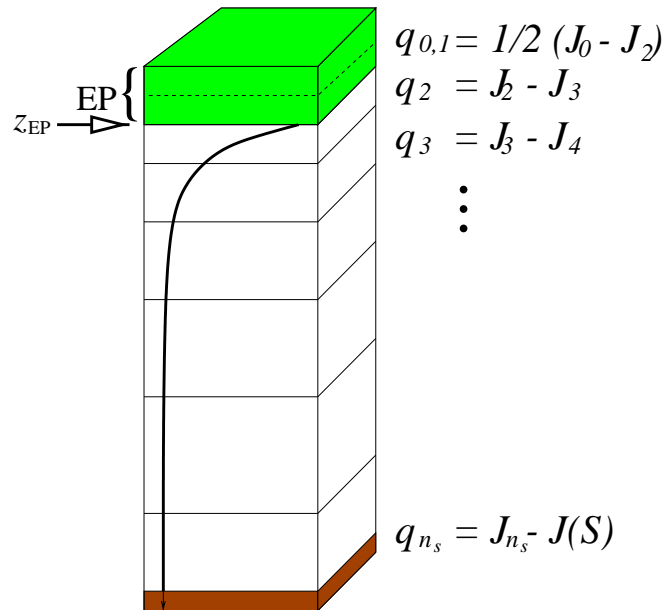


Figure 2.6: Water column with sources and sinks

Biogenic particles are formed in the two uppermost layers of the model (representing the euphotic zone EP) resulting in sinks of dissolved nutrients (exceptions are discussed in Appendix A). Within the euphotic zone, particle fluxes are not defined. Particle flux $J(z)$ is defined *below* the euphotic zone, i.e. for $z \geq z_{EP}$. The flux

$J(z_{EP}) = J_2$ measures the export flux at the base of the euphotic zone.

The export of nutrients results in sinks in the two euphotic zone layers and, assuming that both layers contribute to the same amount of production, the sink terms become:

$$q_{0,1} = -\frac{1}{2}J_2 \quad (2.26)$$

In the next box, the nutrient source q_2 is given by the flux *into* the box (J_2) minus the flux *out* of the box 2 into box 3 (J_3). In this way, all sources of dissolved nutrients are gradually calculated top down the water column.

$$q_n = J_n - J_{n+1} \quad (2.27)$$

In the lowest box n_s , sediment accumulation is modeled with particle flux $J(\mathcal{S})$ (flux to the sediment).

$$J(\mathcal{S}) = s \cdot J_{n_s} \quad (2.28)$$

Maximum accumulation occurs if all particles reaching the bottom layer are removed from water column ($s = 1$), minimum accumulation, if no particles accumulate ($s = 0$). The parameter s regulates accumulation within bounds $[0 : 1]$ to allow for percentual removal of particles:

Nutrient source is again the particle flux reaching the bottom layer minus the particle flux leaving the bottom layer.

$$q_{n_s} = J_{n_s} - J(\mathcal{S}) = (1 - s) \cdot J_{n_s} \quad (2.29)$$

Whereas particle flux into the bottom layer manifests in a source of dissolved nutrients in the bottom box, accumulation of surface sediments is a net sink. The total sink due to accumulation of surface sediments is balanced with riverine input of dissolved nutrients (this is discussed in greater detail in Appendix A).

Combination of Equations (2.26), (2.27), and (2.29) gives the overall definition of source and sink terms due to particle fluxes in the water column:

$$\begin{aligned} q_n &= \frac{1}{2}[J_0 - J_2] & n = 0, 1 \\ q_n &= J_n - J_{n+1} & 1 < n < n_s \\ q_n &= J_n - J(\mathcal{S}) & n = n_s \end{aligned}$$

So far, this formulation is independent of the particular functional form of particle fluxes $J(z)$.

Honoring former work of various scientists (c.f. Section 1), particle fluxes are described using functions (2.1):

$$J(x, y, z) = \alpha(x, y)z^{-\beta(x, y)} \quad z \geq z_{EP}$$

For organic carbon, this description is well established and thus allows direct comparison with estimates derived with other methods. In contrast, $CaCO_3$ and *Opal* dissolution in water column is a major point of interest in modern studies (Rague-neau et al., 1997) and is currently not well understood. In biogeochemical models,

these fluxes are sometimes described with exponentially decreasing formulae (c.f. Section 1.2).

The exponential form of particle fluxes is more convenient in computational models but nevertheless in this study all components of biogeochemical material are computed with Equations (2.1). The difference between fluxes $\propto 1/z$ and $\propto \exp(z)$ is depicted in Fig. 2.7.

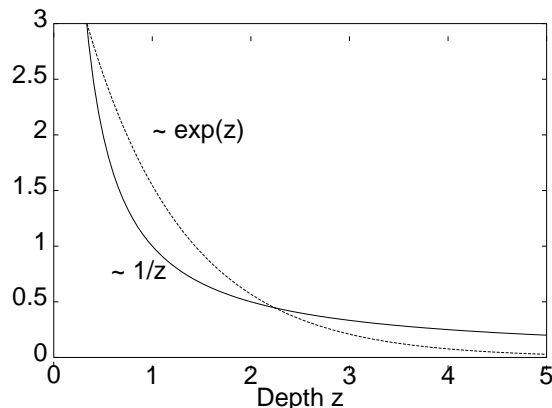


Figure 2.7: Functions describing particle fluxes decreasing with depth exponentially and $\propto 1/z$, respectively (arb. units)

Exponentially decreasing particle fluxes correspond to the physical/chemical processes of degradation in the water column: Particle remineralization is proportional to particle abundance.

Regarding the fact that biological activity is highest in the upper parts of the ocean where biogenic material is fresher and thus more reactive leads to a preference for the other alternative: Equations $\propto 1/z$ describe highest redissolution in the upper layers and almost no decrease in particle flux in the very deep ocean.

All parameters are bound to positive values to avoid negative exports, increasing particle fluxes, and negative accumulation.

In the following, definitions for α , β , and s are given in detail.

2.7.1 Export production

Export production (EP) appears as a sink of dissolved nutrients in the euphotic zone. The amount of nutrients exported is optimized by the model. Simplifying one could say, that nutrient excess (compared to data) physically transported into the euphotic zone due to advection and diffusion is removed simulating particle formation. The sink $q_{0,1}$ is that part of primary production which is not recycled within the euphotic zone but sinks out, and the size of sink $q_{0,1}$ is described with parameter α . As already mentioned in Section 1.1, the ratio $\frac{\text{ExportProduction}(EP)}{\text{PrimaryProduction}(PP)}$ is sometimes called 'f-ratio' and describes the relative portion of exported primary production. Export production can thus be written as 'f-ratio' $\cdot PP$ and this expression is more common in literature. To make comparisons more convenient, a new parameter

$\gamma \propto \alpha$ is introduced which describes a relation of model export production to literature primary production.

- **Organic carbon**

The most classical definition of export production α for organic carbon was introduced by Eppley and Peterson (1979). They derived an empirical relationship for the 'f-ratio' using assimilation- and export flux measurements of nitrate and ammonium:

$$EP/PP = \frac{1}{410} \cdot PP \implies EP = \frac{PP^2}{410} \quad (2.30)$$

Using this equation and primary production PP from Berger (1989) the parameter γ gives a relative portion describing how much of Eppley and Peterson's (1979) export production is exported (i.e., $\gamma = 1$ means model export equals Eppley and Peterson's (1979) export).

$$EP_{Model} = \gamma_{C_{org}} \cdot EP_{Eppley} = \gamma_{C_{org}} \cdot \frac{PP_{Berger}^2}{410} \quad (2.31)$$

At the base of the euphotic zone, particle flux J is equivalent to export production. Normalization of particle fluxes to depth of export z_{EP} leads to:

$$\begin{aligned} J(z) &= \alpha z^{-\beta} \quad z \geq z_{EP} \\ J(z_{EP}) &= \gamma_{C_{org}} \frac{PP^2}{410} = EP \\ \implies \alpha &= \gamma_{C_{org}} \frac{PP^2}{410} z_{EP}^{\beta} \end{aligned} \quad (2.32)$$

Modeled properties related to organic carbon are nitrate, phosphate, carbon, oxygen, and alkalinity. Relative contributions are calculated using Redfield's ratios (Codispoti (1989), Redfield et al. (1963)):

$$N : P : C : O = 16 : 1 : 106 : -138 \quad (2.33)$$

I.e., the molar ratio in a compound of organic carbon is constant and for each phosphate assimilated, $16N$ and $106C$ are used up whereas 138 oxygen atoms are set free due to photosynthesis. Instead of a single sink term for 'organic carbon'

$$q_{0,1C_{org}} = -\frac{1}{2}\alpha_{C_{org}}, \quad (2.34)$$

four definitions are given for the corresponding properties with coefficient rdf (= Redfield ratio):

$$q_{0,1N,P,C,O} = -rdf \cdot \frac{1}{2}\alpha_{C_{org}} \quad rdf = 16, 1, 106, -138 \quad (2.35)$$

Further, organic carbon production affects total alkalinity ($TALK$) in amounts

$$q_{0,1TALK} = +rdf \cdot \frac{1}{2}\alpha_{C_{org}} \quad rdf = 16 \quad (2.36)$$

- **Calcite**

For calcite ($CaCO_3$), the parameter γ gives the portion of 5% of primary production which is exported (i.e., $\gamma = 1$ means that the molar ratio of $CaCO_3$ to primary produced C is 5/100). Normalization to depth of export gives:

$$\begin{aligned} J(z) &= \alpha_{CaCO_3} z^{-\beta_{CaCO_3}} & z \geq z_{EP} \\ J(z_{EP}) &= \gamma_{CaCO_3} \frac{PP}{20} = EP_{CaCO_3} \\ \implies \alpha_{CaCO_3} &= \gamma_{CaCO_3} \frac{PP}{20} z^\beta \end{aligned} \quad (2.37)$$

$CaCO_3$ formation effects total alkalinity ($TALK$) and C . The sinks become

$$q_{0,1C} = -\frac{1}{2}\alpha_{CaCO_3} \quad (2.38)$$

$$q_{0,1TALK} = -\alpha_{CaCO_3} \quad (2.39)$$

- **Opal**

For *Opal*, the parameter γ gives the portion of 5% of primary production which is exported (i.e., for $\gamma = 1$, the molar ratio of Si to primary produced C equals 5/100). Normalization to depth of export gives:

$$\begin{aligned} J(z) &= \alpha_{Opal} z^{-\beta_{Opal}} & z \geq z_{EP} \\ J(z_{EP}) &= \gamma_{Opal} \frac{PP}{20} = EP_{Opal} \\ \implies \alpha_{Opal} &= \gamma_{Opal} \frac{PP}{20} z^\beta \end{aligned} \quad (2.40)$$

Biogenic silica production is calculated independently of other elements than silica. The sink term is simply defined as

$$q_{0,1Si} = -\frac{1}{2}\alpha_{Opal} \quad (2.41)$$

2.7.2 Remineralization

The depth of remineralization is given by parameter β . A large value of β indicates shallow remineralization, at smaller values particles are sinking to greater depth. Due to remineralization in the water column, dissolved nutrients are set free (sinking particles as sources of dissolved nutrients, c.f. Equations (2.30) and (2.27)) and sources vary in magnitude depending on both parameters α and β . In this model, sources of nutrients are set to reproduce Equations (2.1) as follows:

- **Organic carbon**

To match the desired flux equations, water depths for levels n must be taken into account. The source in box n becomes the flux into that box $J(z_n)$ ($z_n =$

depth of upper box boundary) minus the flux out of box n at depth z_{n+1} (lower box boundary). Obeying definitions from Equations (2.27) the source term for organic carbon becomes

$$q_{n_{C_{org}}} = \alpha_{C_{org}} z_n^{-\beta_{C_{org}}} - \alpha_{C_{org}} z_{n+1}^{-\beta_{C_{org}}} \quad (2.42)$$

Analogous to equations 2.35 this gives four sink terms linked to organic matter redissolution for each box:

$$q_{n_{N,P,C,O}} = rdf \quad q_{n_{C_{org}}} \quad rdf = 16, 1, 106, -138 \quad (2.43)$$

and effects on *TALK*

$$q_{n_{TALK}} = -rdf \quad q_{n_{C_{org}}} \quad rdf = 16 \quad (2.44)$$

- **Calcite**

$CaCO_3$ remineralization is defined in the same way and again properties affected are carbon and *TALK*:

$$q_{n_C} = \alpha_{CaCO_3} z_n^{-\beta_{CaCO_3}} - \alpha_{CaCO_3} z_{n+1}^{-\beta_{CaCO_3}} \quad (2.45)$$

$$q_{n_{TALK}} = -2 \cdot (\alpha_{CaCO_3} z_n^{-\beta_{CaCO_3}} - \alpha_{CaCO_3} z_{n+1}^{-\beta_{CaCO_3}}) \quad (2.46)$$

- **Opal**

Opal remineralization is defined in the same manner and again the only property affected by *Opal* remineralization is dissolved silicate giving:

$$q_{n_{Si}} = \alpha_{Opal} z_n^{-\beta_{Opal}} - \alpha_{Opal} z_{n+1}^{-\beta_{Opal}} \quad (2.47)$$

2.7.3 Accumulation

Accumulation of surface sediments is modeled as particle flux through the water-sediment interface. Particle flux reaching the bottom box is not fully remineralized but maximum 100% are virtually transferred to the sediment. Particles accumulated in the sediment are no longer available to serve as nutrient source. Thus, a small fraction of originally exported biomass leaves the water column and the sediment appears as a sink of nutrients. Parameter s regulates the flux into the sediment and describes the portion of the particle flux which is *not* remineralized (c.f. Equation (2.28)). The flux into the sediment becomes:

$$J(\mathcal{S}) = s \cdot J(z_{n_s}) \quad (2.48)$$

Analogous to definitions in Section 2.7.2, the source is defined by the flux into the bottom box n_s minus the flux out of the bottom box, which here is the flux to the sediment $J(\mathcal{S})$.

$$q_{z_{n_s}} = J(z_{n_s}) - J(\mathcal{S}) \quad (2.49)$$

The nutrient source in the bottom box becomes:

$$\begin{aligned} J(z_{n_s}) &= \alpha z_{n_s}^{-\beta} \\ J(\mathcal{S}) := s \cdot J(z_{n_s}) &= s\alpha z_{n_s}^{-\beta} \\ \implies q_{n_s} &= (1-s)\alpha z_{n_s}^{-\beta} \end{aligned} \quad (2.50)$$

- **Organic carbon**

The source term for organic carbon in the bottom box n_s becomes

$$q_{n_s, C_{org}} = (1 - s_{C_{org}})\alpha_{C_{org}} z_{n_s}^{-\beta_{C_{org}}} \quad (2.51)$$

which again leads to four associated sources

$$q_{n_s, N, P, C, O} = rdf \cdot q_{n_s, C_{org}} \quad rdf = 16, 1, 106, -138 \quad (2.52)$$

and the effect on *TALK*

$$q_{n_s, TALK} = -rdf \cdot q_{n_s, C_{org}} \quad rdf = 16 \quad (2.53)$$

- **Calcite**

$CaCO_3$ remineralization in the bottom box gives the source for dissolved silica

$$q_{n_s, C} = (1 - s_{CaCO_3})\alpha_{CaCO_3} z_{n_s}^{-\beta_{CaCO_3}} \quad (2.54)$$

$$q_{n_s, TALK} = 2 \cdot (1 - s_{CaCO_3})\alpha_{CaCO_3} z_{n_s}^{-\beta_{CaCO_3}} \quad (2.55)$$

- **Opal**

Opal remineralization in the bottom box gives the source for dissolved silica

$$q_{n_s, Si} = (1 - s_{Opal})\alpha_{Opal} z_{n_s}^{-\beta_{Opal}} \quad (2.56)$$

2.7.4 River input

To guarantee conservation of nutrients, removal of nutrients at the sediment-water-interface has to be balanced by any input of the same magnitude. This is done by river input. Therefore, sources of dissolved nutrients are set geographically close to river mouths. In the corresponding boxes, nutrients are added depending (a) on the contribution of the particular river to total river input (percentage), and (b) on the total amount of particles accumulated in the sediments. The relative contribution of a river to total riverine input depends on the choice of how many and which rivers are taken into account. The particular choice for the experiments is discussed in Appendix A. The sum of accumulated particles over all columns amounts to the global annual flux to the sediment Acc_{global} for *C_{org}* and *Opal*, respectively.

$$Acc_{global} = \sum_{columns} J(\mathcal{S}) \quad (2.57)$$

Dissolved nutrients are added in the uppermost box of a 'column at a river'. Let i be the number of rivers taken into account and the relative contribution of a river is r_i with

$$r_i \in [0 : 1] \quad \text{and} \quad \sum_i r = 1 \quad (2.58)$$

The relative contribution of the rivers can be set for organic carbon, inorganic carbon, and silicate separately. According to the redfield ratios, the additional source terms in boxes near rivers n_r become:

$$q(n_{r,i})_{N,P,C,O,Si,TALK} = r_i \sum_{\text{columns}} J(\mathcal{S})_{N,P,C,O,Si,TALK} \quad (2.59)$$

2.7.5 Comment on the constraints of model particle fluxes

The amount of data available associated with a given parameter determines how well the parameter is constrained. All model particle fluxes determined with the adjoint model depend on data of dissolved nutrients, no additional a priori knowledge is regarded. As can be seen in the definitions of biogeochemical particle fluxes, organic carbon is constrained by phosphate, nitrate, oxygen, total carbon, and alkalinity. C_{org} particle formation and remineralization is determined using the total information about sources and sinks of these properties in the water column. The relation of data density to the number of parameters to be optimized is thus quite good for organic carbon. Silicate measurements are also quite common but the constraint for *Opal* fluxes is vaguer compared to organic carbon. The parameter weakest constrained are export production, remineralization, and accumulation of $CaCO_3$. Measurements of total carbon and alkalinity are rare and not evenly distributed over the world ocean. This should be kept in mind when interpreting the results presented later on and when comparing these results with other models. The dynamic model of Maier-Reimer (1993) assumes deterministic ratios of shell material to soft tissue ($\frac{Opal+CaCO_3}{C_{org}}$) with limitations to *Opal* production (availability of silica). This gives a much stronger constraint for $CaCO_3$ fluxes because data of dissolved silicate are used to determine calcite formation. In the model presented here, all particle fluxes are calculated on the basis of data of the constituents involved in particle formation and remineralization only.

2.8 Costfunction

Once all parameters are set in the advection/diffusion matrix and for source terms in Equation (2.17), the system is solved for all properties of interest. This gives the model distributions of vertical velocities, temperature, salinity, oxygen, carbon dioxide, and dissolved nutrients (all dependent parameters \tilde{p}). Once the model state (the complete vector $p = [p^*, \tilde{p}]$) is determined, the solution is evaluated by calculating the costfunction $F(p^*, \tilde{p})$. The costfunction $F(p^*, \tilde{p})$ is a scalar function of all model parameters and might contain any undesired feature formulated in terms of functions of independent and dependent parameters. These features must not be

fulfilled exactly but 'as good as possible' and terms in $F(p^*, \tilde{p})$ are consequently named 'soft constraints'. How close a particular constraint is fulfilled by the model can be adjusted by multiplying the individual terms by weight factors.

2.8.1 Terms of costfunction $F(p^*, \tilde{p})$

All terms of the costfunction used in this study are described below. Most terms of the costfunction are discussed in detail in earlier publications of Schlitzer (1993, 1999). Here, only a short review of terms used in this study is given. New and/or refined terms of the costfunction are marked †.

1. Deviations from initial geostrophic shear

Outside the equatorial band ($10^\circ S - 10^\circ N$), the vertical shear $u_z = \partial u / \partial z$ and $v_z = \partial v / \partial z$ of the horizontal velocities is required to be close to original geostrophic shear $u_z^* = \partial u^* / \partial z$ and $v_z^* = \partial v^* / \partial z$ computed from geostrophic flow calculations. α_p is a spatially varying weight factor depending on statistical information (quality indicator) and σ is a normalization factor.

$$\sum \left[\left(\frac{u_z - u_z^*}{\alpha_p \sigma u_z^*} \right)^4 + \left(\frac{v_z - v_z^*}{\alpha_p \sigma v_z^*} \right)^4 \right] \quad (2.60)$$

2. Deviations of mixing coefficients from 'mixing coefficient data'

Mixing coefficients are kept close to 'mixing coefficient data' from literature and/or earlier model calculations especially performed to determine best values.

$$\left[\frac{p_k - P_k}{\sigma_{P_k}} \right]^2 \quad (2.61)$$

3. Pointwise deviations from data

For data of temperature, salinity, oxygen, phosphate, nitrate, silicate, total carbon, and total alkalinity, deviations of model fields X_{mod} (or dependent parameters \tilde{p}) to measurements X_{data} are computed pointwise. σ denotes measurement errors.

$$\sum \left(\frac{X_{mod} - X_{data}}{\sigma_X} \right)^2 \quad (2.62)$$

4. Systematic deviations from data

For the same properties, the bias is calculated by computing the systematic deviation within the neighborhood of a box.

$$\sum \left(\sum_j \frac{X_{j,mod} - X_{j,data}}{\sigma_{X_j}} \right)^2 \quad j \in [\text{next neighbors}] \quad (2.63)$$

5. Deviations from sediment trap data †

Particle fluxes are now explicitly calculated in the model. Flux parameters

α, β, s give fluxes for the whole model domain and in boxes where trap data exist, the deviations to data are calculated. A detailed discussion of sediment trap data J_{data} and model fluxes J_{mod} is given in Section 4. The general form of this term is analogous to other terms penalizing deviations to data. σ denotes measurement error.

$$\sum \left(\frac{J_{mod} - J_{data}}{\sigma_J} \right)^2 \quad (2.64)$$

6. Smoothness constraints (linear)

The second derivative of parameters p^* and \tilde{p} is used to enforce spatial smoothness of vertical velocities \vec{w} , surface heat fluxes, and gas exchange rates. Here, p denotes the respective parameter and p_e, p_w, p_n, p_s are the parameter values of the next neighbors in eastern, western, northern, and southern direction, respectively.

$$\sum [(p_e - 2p + p_w)^2 + (p_s - 2p + p_n)^2] \quad (2.65)$$

7. Smoothness constraints (squared) †

The second derivative is used to enforce spatial smoothness of biogeochemical parameters. The parameters are squared prior penalizing the second derivative because all biogeochemical parameters contribute with their square value to the model fields. This simply reflects the 'true' appearance of export production, remineralization, and accumulation.

$$\sum [(p_e^2 - 2p^2 + p_w^2)^2 + (p_s^2 - 2p^2 + p_n^2)^2] \quad (2.66)$$

8. Deviations from a priori values (global)

For all independent parameters p^* deviations from a priori knowledge can be penalized (i.e., if one knows that a parameter value *must* be close to a certain number P).

$$\sum \left[\frac{p^* - P}{\sigma_P} \right]^4 \quad (2.67)$$

9. Deviations from a priori volume transports

Deviations from a priori volume transports are penalized by integrating the horizontal velocities over prescribed surfaces and calculating the differences to a priori transports \mathcal{T} .

$$\left(\sum_i \vec{u}A_i - \mathcal{T}_i \right)^2 + \left(\sum_j \vec{v}A_j - \mathcal{T}_i \right)^2 \quad (2.68)$$

2.8.2 Weighting of costfunction $F(p^*, \tilde{p})$

$F(p^*, \tilde{p})$ is a measure for the 'quality' of a model solution with respect to all individual terms. A large value of $F(p^*, \tilde{p})$ indicates that the model solution does *not* fulfill the features desired by the penalty terms. The individual terms of $F(p^*, \tilde{p})$ are multiplied by weight factors to force the model in special directions. Table 2.3

summarizes weight factors used in this study. The weights are very different, ranging from 0.1 to 10^6 . This does not mean that, for instance, a priori transports are much more important than salinity data. The minimization respects the absolute value of weight factor multiplied with the penalty term. Low weight factors for deviations to data are mostly compensated by a high density of measurements. The absolute values are within the same range. Most of the weight factors were kept constant throughout all model runs. Changes due to the variation of weight factors are discussed in Section 4.2.

Term	Weight	Notes
Dev. from initial geostr. shear	0.01	
Smoothness of \vec{w}	1.0	
Dev. from a priori vol. transports	10^6	See Table 2.4
Dev. from initial p_{K_h}	10^4	Initial mixing coefficients were taken from Schlitzer (1995)
Dev. from initial p_{K_v}	10^4	
Dev. from heat-flux data Q_{data}	10	
Smoothness of heat-flux Q_{mod}	2	
Smoothness of parameter $\gamma_{C_{org}}$	1, var	Different weight factors were used to smooth out export production and remineralization in experiments SLAT and SLANT (see Section 2.9)
Smoothness of parameter $\beta_{C_{org}}$	1, var	
Smoothness of parameter γ_{CaCO_3}	1, var	
Smoothness of parameter $\beta_{C_{org}}$	1, var	
Smoothness of parameter γ_{Opal}	1, var	
Smoothness of parameter β_{Opal}	1, var	
Dev. from data ($X_{mod} - X_{data}$)	0.1	Modeled properties
Bias of $X_{mod} - X_{data}$	0.1	$T, S, O_2, PO_4, NO_3, Si, TALK$
Dev. from $\sum CO_2$ data	0.5	Weight factor high because data density of $\sum CO_2$ is low
Bias of $\sum CO_{2,mod} - \sum CO_{2,data}$	0.5	
Dev. from $TALK$ data	0.5	Weight factor high because data density of $TALK$ is low
Bias of $TALK_{mod} - TALK_{data}$	0.5	
Dev. from trap data C_{org}	var	Different weight factors were used in the experiments, see Section 2.9
Dev. from trap data $CaCO_3$	var	
Dev. from trap data $Opal$	var	

Table 2.3: Weight factors in costfunction $F(p^*, \tilde{p})$. Var: variable, see text

Prescribed top-to-bottom flows were the same for all experiments and are summarized in Table 2.4.

Area	Sv	Notes
Total inflow into Mediterranean Sea	0	Open model boundary
Total inflow into Red Sea	0	Open model boundary
Total inflow into Persian Gulf	0	Open model boundary
Baffin Bay export of arctic waters	1	
Florida Current	30	
Drake Passage	130	
NADW across the equator	-18	
Indonesian Passage	-10	

Table 2.4: A priori volumes transports prescribed for all experiments

2.9 Experiments

Several experiments have been carried out to obtain optimum ocean circulation and biogeochemical particle fluxes. Main objective in all model runs was to find parameters for export production, remineralization, and accumulation rates of biogeneous particles which are consistent with nutrient data. The sensitivity of model particle fluxes to the assimilation of sediment trap data is investigated by running experiments with and without these -new- modeled properties. Also, differences arising from the implementation of sediment accumulation is investigated. The individual experiments presented here are:

- **REF**

A reference experiment (REF) was performed in the models most simple mode. No sediment trap data are assimilated and no accumulation of surface sediments is considered. This model setup is comparable with Schlitzer's (1999) experiments. This experiment is chosen as the reference to compare for changes due to model modifications. General model results and distributions from experiment REF are presented in Section 3.

- **HANT**

In experiment HANT (High Accumulation, No Traps), accumulation rates of biogeneous surface sediments are calculated. No sediment trap data constraint was applied. It turned out that initial values of relative accumulation rates were chosen too high (see discussion in Section 5). The model reduced the parameter s for *Opal*. In subsequent model runs, initial values for accumulation of surface sediments were set lower. Results from experiment HANT are presented in Section 5.

- **LAT, SLAT, SLANT**

Experiment LAT was initialized with lower values for sediment accumulation than HANT and was constrained to reproduce sediment trap data (LAT: Low Accumulation and Traps). The weight factors for deviations from sediment trap data were set to very high values (three orders of magnitude larger than for other terms) to force the model to strictly reproduce the data. This led to unrealistic patterns in the parameter fields.

Experiment SLAT is a subsequent model run of LAT. Here, weight factors for the reproduction of sediment trap data were reduced whereas smoothness constraints for the biogeochemical parameters were increased to 'smoothen out' the parameter distributions (SLAT: Smooth Low Accumulation with Traps). After a smooth solution of experiment SLAT was gained, weight factors for the reproduction of sediment trap data were set to almost zero (SLANT: Smooth Low Accumulation, No Traps). The assimilation of sediment trap data, effects of smoothing and the 'release' of the model from sediment trap data is described in Section 4.

Initial fields for parameters α, β , and the current field were taken from Schlitzer (1999) and were identical for experiments REF, HANT, and LAT. The differences are summarized in Table 2.5 below.

Name	Number of iterations	Trap data	$s_{C_{org}}$ initial value	s_{CaCO_3} initial value	s_{Opal} initial value
REF	70,000	-	-	-	-
HANT	70,000	-	0.09	0.16	0.25
LAT	70,000	+	0.09	0.16	0.04
SLAT	70,000	+	LAT	LAT	LAT
SLANT	10,000	-	SLAT	SLAT	SLAT

Table 2.5: Different experiments, explanation see text

3 General model results and reference experiment

The different experiments show very similar patterns for all parameters and properties on a global scale. The general similarity is also seen by evaluating the costfunction. Figure 3.1 shows absolute values of selected terms in the costfunction at the end of the iterations. When evaluating the costfunction one has to keep in mind that not all experiments were run for the same number of iterations. Experiments SLAT had 70,000, experiment SLANT 80,000 iterations more to find 'the best solution'. None of the experiments described here were terminated at a global minimum but after a certain number of iterations. The costfunction thus measures the model solution *at the state after termination which is not necessarily identical with the best solution which could be obtained* for this costfunction.

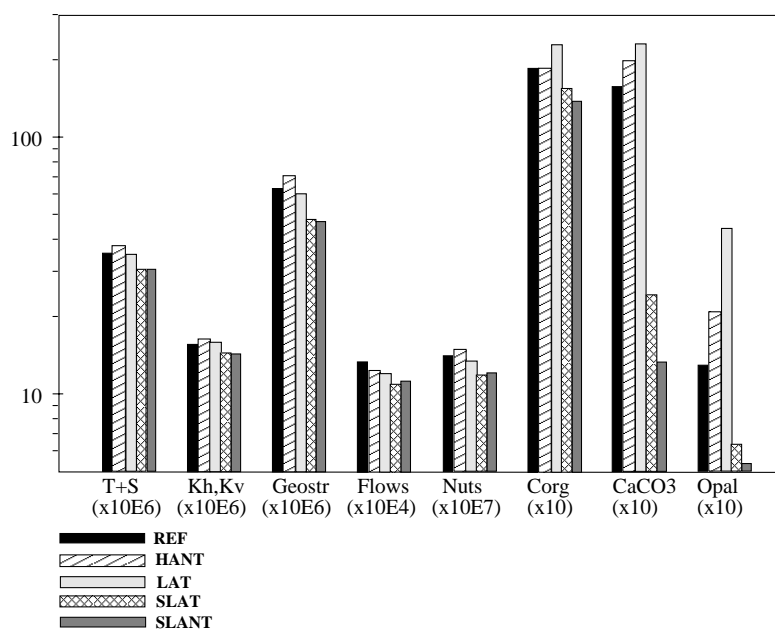


Figure 3.1: Absolute values of terms of costfunction after termination of the optimization. For explanation, see text

The value of 'T+S' in Fig. 3.1 is the sum of terms penalizing deviations and bias of model temperature and salinity compared to data, 'Kh,Kv' denotes deviations from initial 'mixing coefficient data'. The value of 'Gestr' denotes deviations from initial geostrophic shear, 'Flows' belongs to the sum of all deviations from prescribed volume transports. The different experiments show quite similar values for these 'physical' constraints, but experiment HANT systematically has the highest values. A possible explanation for this is that experiment HANT started with relatively high accumulation rates for *Opal* and *CaCO₃*. The parameters for accumulation were drastically reduced in this experiment (see Section 5). The gradient of $F(p^*, \tilde{p})$ in this experiment might have been dominated by terms related to sediment accumulation rates, at least at the beginning of the model run. Thus, experiment HANT 'had not had the time' to optimize the current field as well as the other experiments,

especially with respect to the closeness to geostrophic shear.

Larger differences between the experiments occur for the terms 'Corg', 'CaCO₃', and 'Opal' which measure the smoothness of parameters α and β . Experiments REF, HANT, and LAT were run with the same weight factors for the smoothness constraints. It can be clearly seen that experiment LAT bears highest values for these terms. This was caused by the assimilation of sediment trap data and forcing the model to exactly reproduce measured fluxes. This experiment produced strong local changes in the parameter fields (see also discussion in Section 4.2) and therefore smoothness constraints were increased for the subsequent experiments SLAT and SLANT. Both experiments bear values of the smoothness constraints which are even smaller than the experiments 'which have never seen sediment trap data' REF and HANT.

The changes due to the assimilation of sediment trap data are discussed in greater detail in Section 4.

The current field and distributions of temperature, salinity, and dissolved nutrients are presented with examples from the experiment REF in the next section.

3.1 Current field

Figure 3.2 shows the transports in surface (Surface $-\sigma_0 = 26.8$), intermediate ($\sigma_0 = 26.8 - \sigma_0 = 36.75$), deep ($\sigma_0 = 36.75 - \sigma_0 = 45.9$), and bottom ($\sigma_0 = 45.9 - \text{Bottom}$) water.

All major current systems of the Atlantic are reproduced. Surface currents as the subtropical gyres, the Benguela Current in the South Atlantic, and the Gulf Stream in the North Atlantic can be seen in Fig. 3.2(a). The deeper parts of the Gulf Stream can also be seen in Fig. 3.2(b). The western boundary counter current and large transports of North Atlantic Deep Water (NADW) across low latitudes appear in Fig. 3.2(c). Bottom waters from the Iceland-Scotland-Overflow and the Denmark Strait are seen in Fig. 3.2(d). Antarctic Bottom Water (AABW) flows northwards mainly in the western part of the Atlantic. The Weddell gyre turns south-westwards at about $30^\circ E$.

The very strong Antarctic Circumpolar Current (ACC) flows eastwards in all layers.

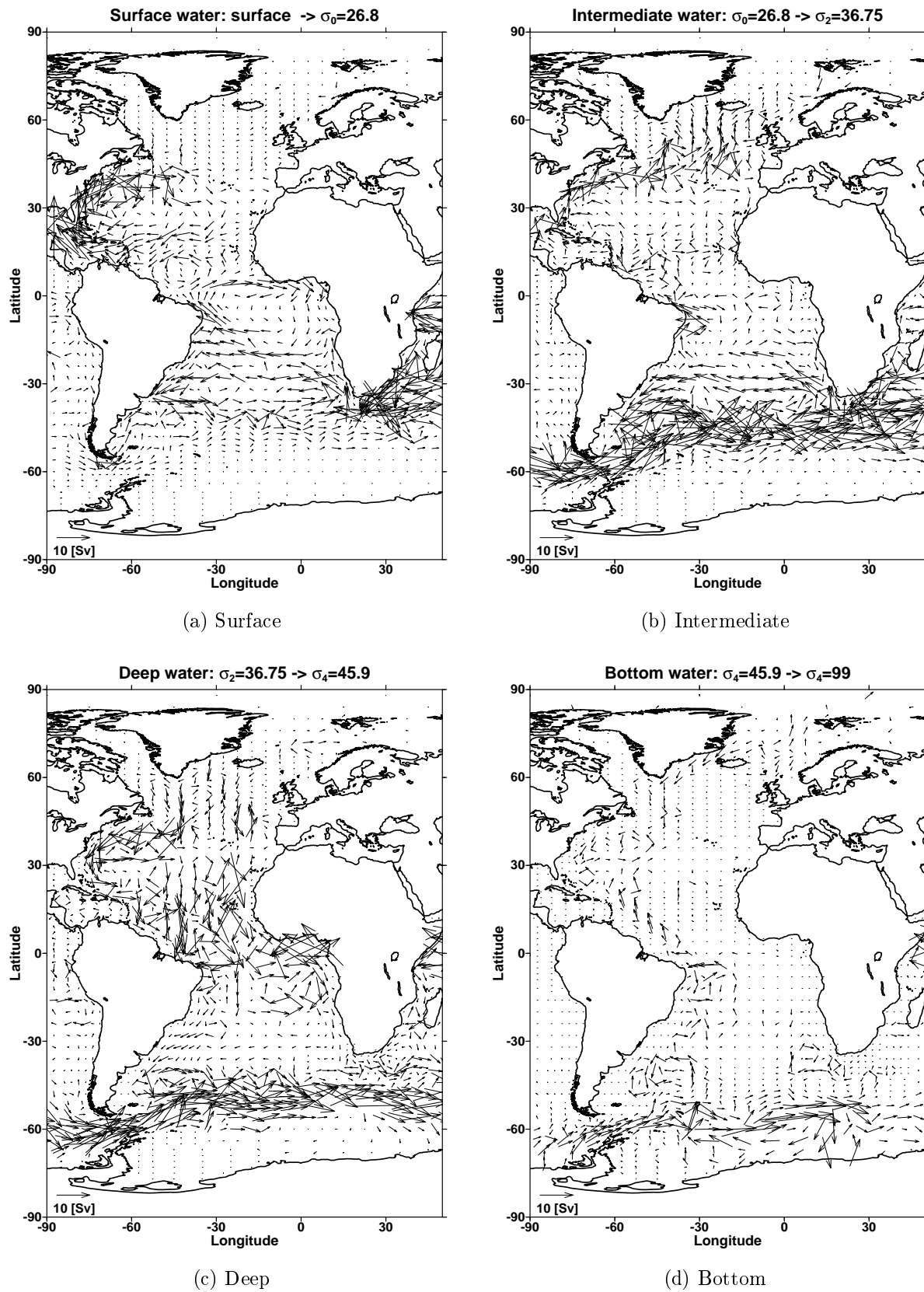


Figure 3.2: Horizontal current field from experiment REF

Figure 3.3 shows the vertical velocities in the Atlantic.

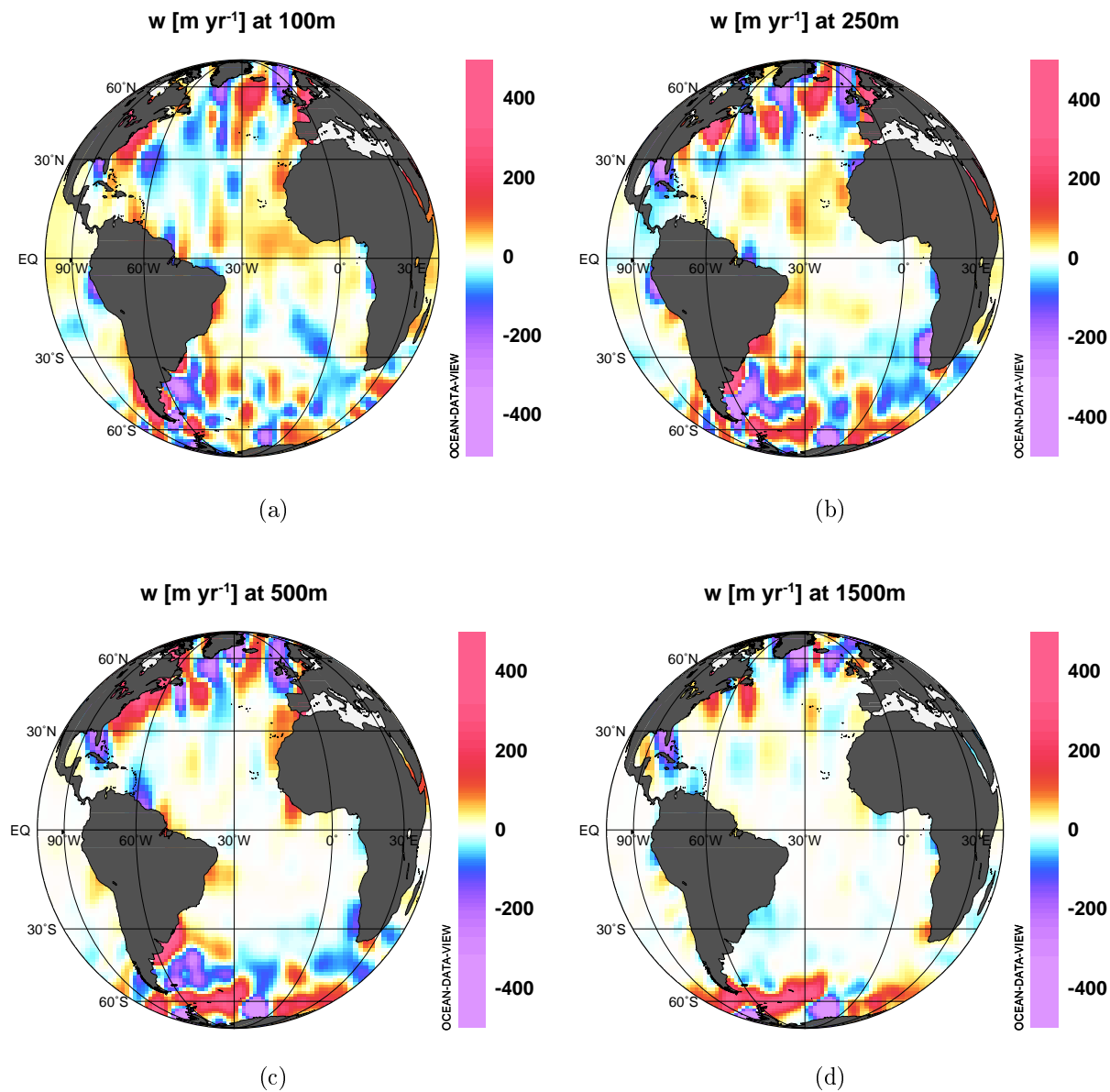


Figure 3.3: Vertical velocities in the Atlantic from experiment REF

In Fig. 3.3(a) to (d) the Antarctic Circumpolar Current (ACC) can be clearly seen. North of the Polar Front (PF) at about $50^\circ S$, the general pattern reflects a zonal downwelling through all layers whereas south of the PF upwelling dominates. This is in accordance with the observation of maximum wind stress at $50^\circ S$ (Toggweiler and Samuels, 1993) causing this convergence and divergence, respectively. The upwelling in the Southern Ocean is very deep which results in an effective transport of silicate-rich deep water (c.f. silicate distribution in Fig. 1.1) and is in agreement with deep strong property gradients found in the Polar Frontal Zone (Orsi et al., 1995). The equatorial upwelling in the eastern Atlantic is much weaker and shallower. At 500m

water depth, no upwelling is seen off the coast of West Africa. It is currently not known whether the upwelling off the southwestern coast of Africa is persistent or seasonal (Summerhayes et al., 1995). The upwelling off the Namibian coast originates from several hundred meters water depth only (Sültenfuß, 1998).

It should be noted that the determination of absolute vertical velocities bears large unavoidable uncertainties. Velocities determined with circulation models strongly depend on model resolution and the spatio-temporal extent of upwelling events. In the model presented here, the annual mean vertical velocity is calculated as the divergence of annual mean horizontal transports divided by the surface of a box. Horizontal velocities are orders of magnitude larger than vertical velocities and a minor change in horizontal velocities can lead to major changes in the respective vertical velocity. This can lead to unrealistic values in small boxes and/or near model boundaries.

Determination of upwelling velocities with other methods (for instance transient tracers or radionuclides) bears similar problems because the spatio-temporal extent of upwelling is difficult to determine. At mid-latitudes, coastal upwelling velocities are in the order of $10^{-4} \frac{cm}{s}$ to $10^{-2} \frac{cm}{s}$ corresponding to ca. $35 \frac{m}{y}$ to $3500 \frac{m}{y}$ (Smith, 1995). Eddies detected in coastal upwelling areas using satellite remote sensing data were associated with small-scale up- and downwelling ranging from $300 \frac{m}{y}$ to $-300 \frac{m}{y}$ (Abbot and Barksdale, 1995). The range of vertical velocities is thus quite large and comparisons of absolute values are difficult.

The vertical velocities determined with the adjoint model are in the range of $-5000 \frac{m}{y}$ to $5000 \frac{m}{y}$ with most velocities between $-500 \frac{m}{y}$ and $500 \frac{m}{y}$ and are thus within the range of independent measurements.

Integrated transports give more stable estimates to characterize the current field. A comparison of different models to calculate mean near-surface upwelling in the equatorial Atlantic ($15^{\circ}S$ to $15^{\circ}N$) was given by Wunsch (1984). He calculated the upwelling at 100m depth in a quasi-geostrophic current field constrained with bomb radiocarbon budgets to be $7Sv - 10Sv$. In this area (Atlantic between $15^{\circ}S$ and $15^{\circ}N$) experiment REF has an integrated upwelling of ca. $11Sv$ at 100m water depth which is very close to Wunsch's (1984) results. Table 3.1 gives horizontal volume transports across selected sections in the Atlantic for all experiments. The transports are within the range of the model results published earlier by de las Heras and Schlitzer (1999). A detailed discussion of the different water paths and also heat transports is given in de las Heras and Schlitzer (1999). The differences between the different experiments are generally smaller than 5%.

Experiment	REF	HANT	LAT	SLAT	SLANT
30°N	-1.0	-1.0	-1.0	-1.0	-1.0
Surface	8.8	8.4	8.5	8.4	8.4
Intermediate	2.0	2.5	2.2	1.9	1.9
Deep	-15.3	-15.8	-15.2	-14.5	-14.5
Bottom	3.5	3.9	3.6	3.2	3.2
Equator	-0.9	-0.8	-0.8	-0.8	-0.8
Surface	1.9	2.2	2.0	1.8	1.8
Intermediate	5.9	6.3	5.9	5.6	5.5
Deep	-11.9	-12.4	-12.0	-11.4	-11.3
Bottom	3.2	3.2	3.2	3.2	3.1
30°S	-0.5	-0.5	-0.5	-0.5	-0.5
Surface	2.0	2.6	2.0	2.0	1.9
Intermediate	6.2	6.0	6.2	5.9	5.8
Deep	-9.6	-9.8	-9.6	-9.1	-9.1
Bottom	0.9	0.8	0.9	0.8	0.8
Drake Passage	126.7	129.0	128.5	125.7	125.6

Table 3.1: Volume transports in Sverdrups ($1Sv = 10^6 m^3/s$) across selected sections in the Atlantic from all experiments. Positive (negative) values indicate northwards (southwards) and eastwards (westwards) transports.

Definitions of water masses:

Surface: Surface $-\sigma_0 = 26.8$, Intermediate: $\sigma_0 = 26.8 - \sigma_0 = 36.75$, Deep: $\sigma_0 = 36.75 - \sigma_0 = 45.9$, Bottom: $\sigma_0 = 45.9 - \sigma_0 = 45.9$ - Bottom

The differences between total northwards and total southwards flows are balanced by inflows from Arctic waters, differences between flows through the Drake Passage and between South Africa and Antarctica, and differences in evaporation minus precipitation.

Experiment HANT yields higher transports compared to the other solutions. An explanation is that all experiments have the tendency 'to slow down' ocean circulation during the optimization course. The experiment HANT to have the fastest circulation is consistent with ideas given above. In experiment HANT, predominant changes were applied to the parameters related to sediment accumulation.

The reasons for the 'quietening' of the ocean are not yet clear but this problem might be partly minimized by introducing dissolved organic matter into the model calculations (Schlitzer, pers. comm.).

3.2 Property distributions

In the following, some examples of model distributions and a comparison to data are given.

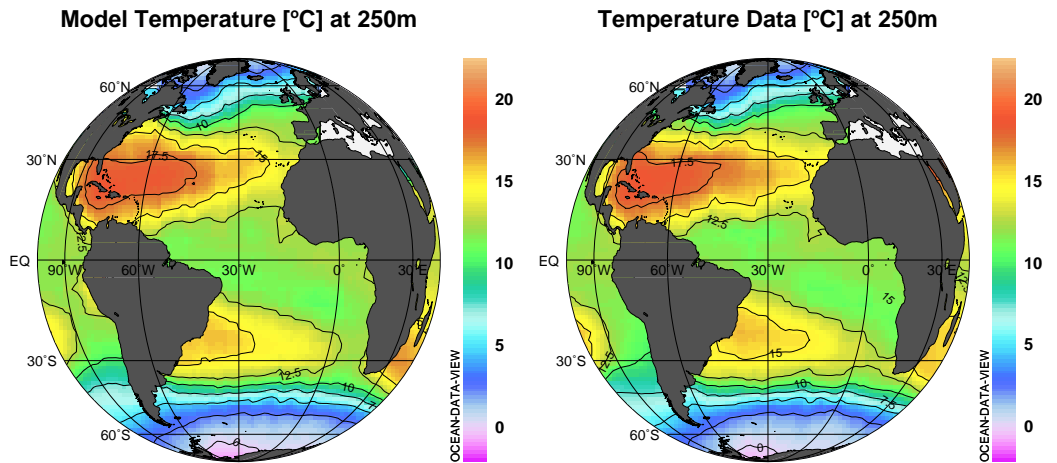


Figure 3.4: Model temperatures (left) and data (right)

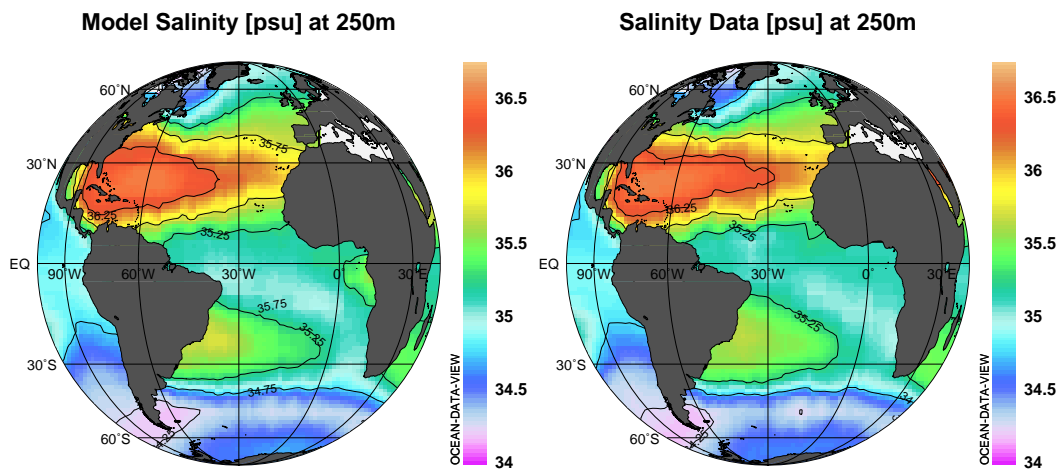


Figure 3.5: Model salinities (left) and data (right)

Deviations of model distributions of temperature, salinity, and nutrients contribute to a considerable amount to the total costfunction. The model is driven to reproduce the assimilated data (c.f. Section 2). I.e., the current field described above was optimized to give small model-data misfits. In the examples, model property distributions from 250 m water depth are shown on the left side and corresponding data are shown on the right side of the figures. Gridding and visualizing of model properties and data was performed using the Ocean Data View software (Schlitzer, 1999b).

The current field from Fig. 3.2 together with surface fresh water fluxes yields temperatures and salinities at 250m as displayed in Fig. 3.4 and 3.5. The physical model fields of temperature and salinity are in excellent agreement with data. Within the

subtropical gyres, temperature and salinities are highest with maximum temperatures and salinities in the Sargasso Sea. Strong temperature gradients are found at the northern boundary of the Antarctic Circumpolar Current and around $50^{\circ}N$ where the contour lines are well reproduced in position and magnitude. Minimum salinities are found in the Antarctic Circumpolar Current at about $50^{\circ}S$.

Dissolved nutrient fields depend on the current field *and* source and sink terms describing export and remineralization of particulate biogenic matter (c.f. Section 1.1 and Section 2.7). Resulting distributions are also very close to observations. As an example, the phosphate distribution at 250m water depth is given in Fig. 3.6. Generally, the large scale features are well reproduced. High phosphate concentrations can be seen near the equator decreasing from east to west, and south of about $50^{\circ}S$. Minimum phosphate concentrations are found in the Sargasso Sea. Model phosphate concentrations are slightly higher than measurements near the equator and in mid-latitudes but absolute deviations rarely exceed $0.1\mu\text{mol}/\text{kg}$.

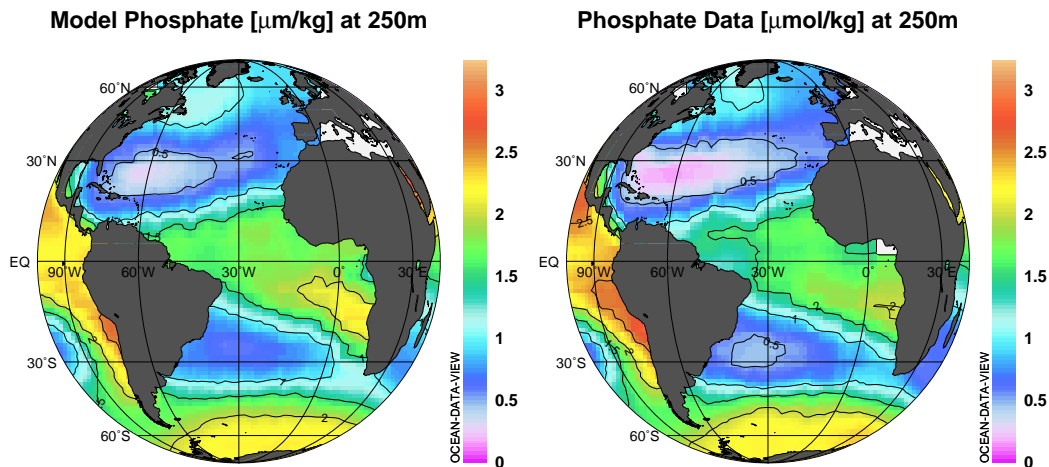


Figure 3.6: Model phosphate (left) and data (right)

Model oxygen distributions depend on the current field, biogeochemical particle fluxes, and gas exchange at the surface. The oxygen distribution in 250m water depth (Fig. 3.7) also is in close agreement with measurements. In low and mid-latitudes, high phosphate concentrations coincide with low oxygen concentrations. This anti-correlation reflects the decomposition of sinking particles: Remineralization of sinking organic matter releases phosphate whereas oxygen is utilized. In the high latitudes the anti-correlation is not seen and oxygen concentrations are high due to intense ventilation.

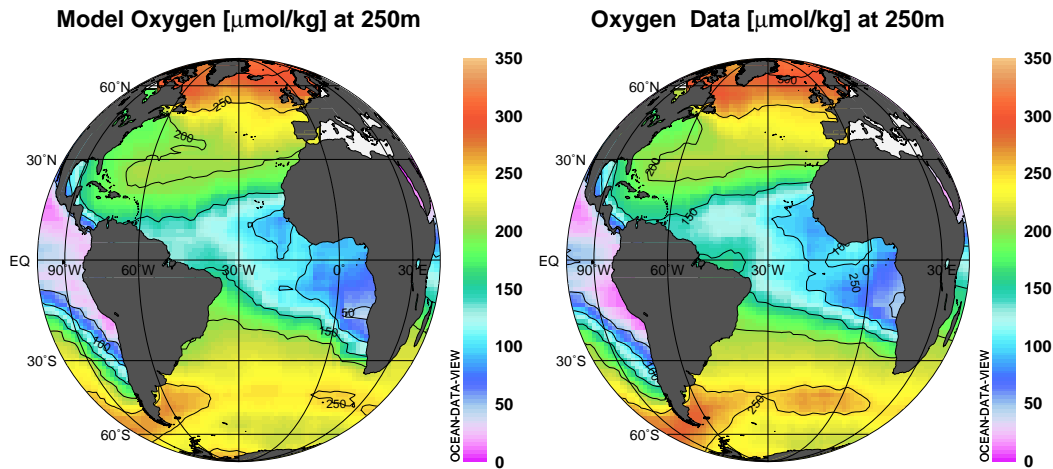


Figure 3.7: Model oxygen (left) and data (right)

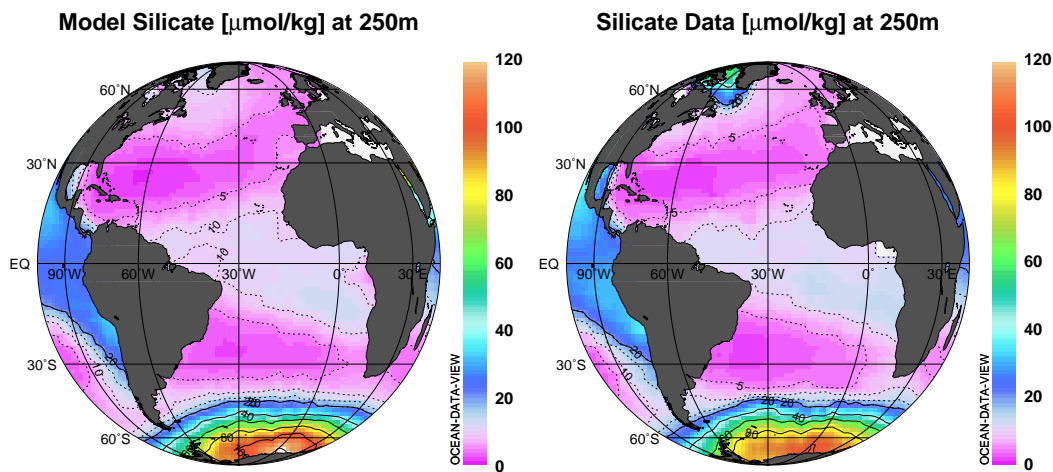


Figure 3.8: Model silicate (left) and data (right)

Data of dissolved silicate show very low concentrations in most parts of the Atlantic (below $20 \mu\text{mol}/\text{kg}$) which is well reproduced by the model. South of 50°S , silicate concentrations increase drastically. Comparing the contour lines of the model distribution (Fig. 3.8, left side) to measurements reveals that despite the nice general agreement the model produces silicate concentrations greater than $100 \mu\text{mol}/\text{kg}$ which are not seen in the data (Fig. 3.8, right side). The -large scale- pattern of dissolved silicate is satisfying and the overestimation of silicate concentration in the southernmost Atlantic is a comparably small misfit. All together, the large scale features of physical properties and nutrients calculated with the adjoint model are very close to observations. The -reasonable- current field together with biogeochemical processes and gas exchange yield model distributions which do coincide with

data. That means, it is indeed possible to find parameters which are in agreement with general oceanographic knowledge (reproduction of known large-scale currents while keeping model geostrophic shear close to 'observed' geostrophic shear). At the same time, biogeochemical parameters are determined which reproduce data of dissolved nutrients accurately.

3.3 Model particle fluxes

Integrated exports for the different experiments were calculated after termination of the optimization. Table 3.2 summarizes global export production and estimates from other authors. Generally, integrated exports are very similar for all experiments. That means, assimilation of sediment trap data has no recognizable effect on the total integral of global export production (experiments LAT and SLAT). As expected, also calculation of sediment accumulation does not alter the globally integrated fluxes of C_{org} and *Opal* (all experiments compared to REF). The only systematic change occurs for $CaCO_3$ which indicates that inclusion of $CaCO_3$ accumulation in sediments might be important for global calcite budgets. Export production rates are higher in all experiments with sediment accumulation rates. Compared to literature values, $CaCO_3$ export production is still much too low. But calcite formation, remineralization and accumulation are not well constrained because only few data of alkalinity and ΣCO_2 exist. One should be cautious to interpret this trend. By comparing model C_{org} export production with literature values it seems that model exports are far too high. Model export is a factor of about 2.5 to 3 higher than proposed by Eppley and Peterson (1979). Eppley and Peterson (1979) excluded polar regions from their calculation and their export was based on comparably low primary production. It was already mentioned that estimates of primary production have increased also about a factor two in recent studies. Even using Eppley and Peterson's (1979) relations would give higher C_{org} exports using re-estimated primary production. The model C_{org} fluxes are thus tendentially in agreement with current knowledge. Total model C_{org} export amounts to about 10 GtC/y which is well in the range as given by other global models (4.8 GtC/y – 15 GtC/y , c.f. Tab. 1.1 in Section 1.2).

	Literature		Model export production				
	PP	EP	REF	HANT	LAT	SLAT	SLANT
Global							
C_{org}	1550 ¹⁾ -3800 ^{2),3)}	280-390 ²⁾	840.3	833.6	843.0	838.0	838.6
$CaCO_3$	530 ⁵⁾	—	99.8	103.3	103.1	101.2	101.0
$Opal$	200-280 ⁴⁾	100-140 ⁴⁾	206.2	209.3	206.5	203.8	203.9

Table 3.2: Global literature estimates of primary and export production and globally integrated model export production at 133m depth from all experiments. Units in $[\frac{TmolC}{y}]$ for C_{org} and $CaCO_3$ and $[\frac{TmolSi}{y}]$ for $Opal$, respectively.

- 1) (Berger et al., 1987): PP 1550 - 2590, EP 20% of PP at 100m depth
- 2) (Eppley and Peterson, 1979): PP 1670 - 3750, EP 280 - 390
- 3) (Antoine and Morel, 1996): PP 3040 - 3800
- 4) (Nelson et al., 1995): PP 200 - 280, EP at 200m depth
- 5) (Milliman, 1993): PP 530

Model *Opal* export production is about 60% to 100% of global *Opal* production (surface) and higher than export production at 200m as proposed by Tréguer et al. (1995). Model export is calculated at 133m depth and its total amount is between Tréguers (1995) primary and export production but closer to primary production. Model *Opal* fluxes follow $\propto 1/z$ and so the main remineralization takes place in the upper model layers. The flux at 200m is thus smaller than at 133m but it is still higher than Tréguer et al.'s (1995) value.

In the following, the spatial distribution of export production and remineralization is discussed. Model parameters were optimized as percentage of primary production as given by Berger et al. (1987) (c.f. Section 2.7). Figure 3.9 shows primary production in the Atlantic to give an impression of the distribution of high/low productive areas. Highest primary production takes place along the eastern boundaries of the oceans and in a zonal band around Antarctica. Strong gradients separate these high production regions from the oceanic 'deserts' within the subtropical gyres. As stated in Section 1.1, mean, high productivity can only take place where advective processes transport dissolved nutrients into the surface layer. The annual mean vertical velocities in the upper ocean (c.f. Fig. 3.3 (a,b)) from the adjoint model show a similar pattern as primary production from Fig. 3.9. In the following, optimized export production and remineralization rates from experiment REF are given for C_{org} , $CaCO_3$, and *Opal*. In the literature, the (variable) 'f-ratio' is often used to calculate export production from primary production. Export production of organic carbon is expected to be related to primary production in a predictable way so patterns of export should be similar to primary production. The shells of phyto- and zoo-plankton built from $CaCO_3$ and *Opal* are not related to primary production in a chemical sense because primary production is calculated from chlorophyll which is part of organic carbon only. $CaCO_3$ and *Opal* production (and so export) patterns may be very different from observed chlorophyll distributions.

Primary production [mol C/m²/yr]

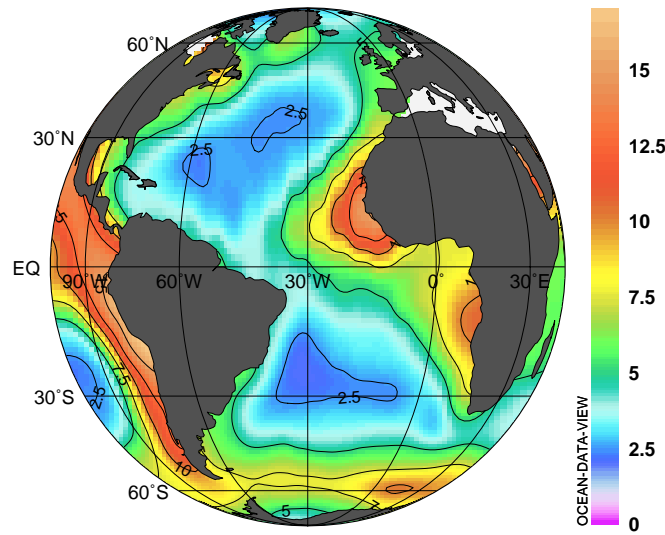


Figure 3.9: Primary production according to Berger et al. (1987)

The export production shown in Fig. 3.10(a) shows strong resemblance to primary production. The subtropical gyres appear as 'marine deserts' with very low export production rates. High export fluxes are found at the eastern boundaries and near the Antarctic Polar Frontal Zone (PFZ). The high productivity upwelling region off the west coast of Africa produces the phosphate maximum and oxygen minimum in the underlying water masses (c.f. Fig. 3.6 and Fig. 3.7) because large amounts of sinking detritus are remineralized.

The parameter β determines the 'steepness' of particle remineralization, i.e. the depth where remineralization takes place. β was set to one at the beginning of the optimization procedure as proposed by Suess (1980). In large areas ($15^{\circ}S$ to $50^{\circ}S$ and north-east of a section from north-west Africa to Canada) parameter β remains one or becomes even smaller in agreement with independent estimates (c.f. Section 1.1). But in distinct regions, parameter β becomes much larger than 1, almost reaching 2. That means that model particle remineralization is much faster than indicated by, for instance, sediment trap measurements. Few models regard the possibility that particle fluxes might decrease so fast with depth. Recent studies also indicate that a very fast remineralization can take place in high productive areas where opportunistic zoo-plankton feeds on sinking detritus in mid-water depths (Bishop, pers. comm.). The variation of parameter β seems to divide the Atlantic ocean into different areas which coincide partly with oceanographic/ecological provinces. Remineralization is fast where sea surface temperatures are comparably high (between $15^{\circ}S$ and $15^{\circ}N$) and/or in areas with intense upwelling along the eastern boundaries and south of the Polar Front (c.f. Fig. 3.3).

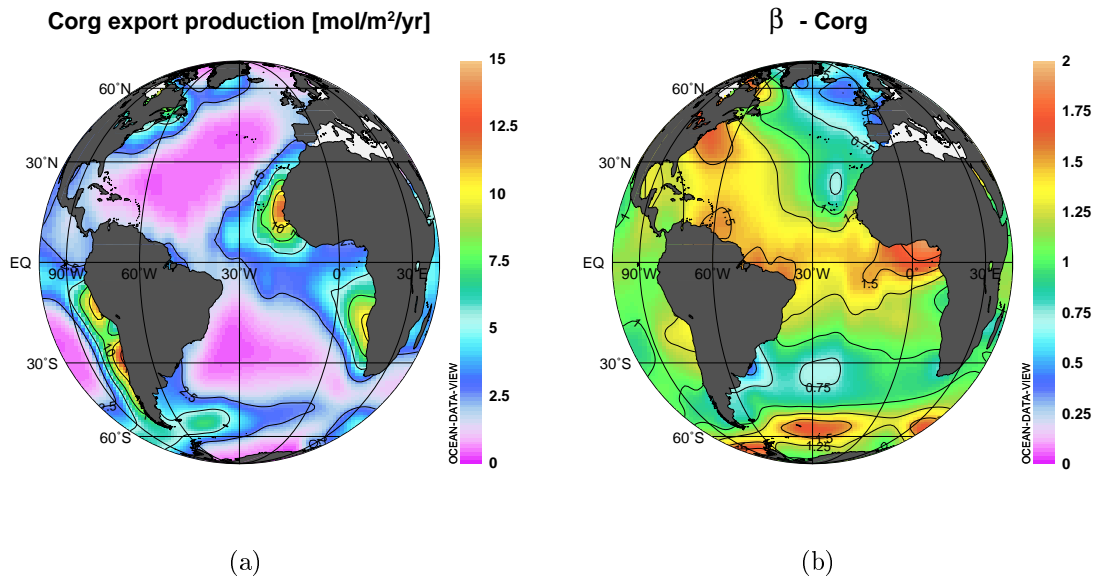


Figure 3.10: C_{org} export production (a) and remineralization scale length β (b)

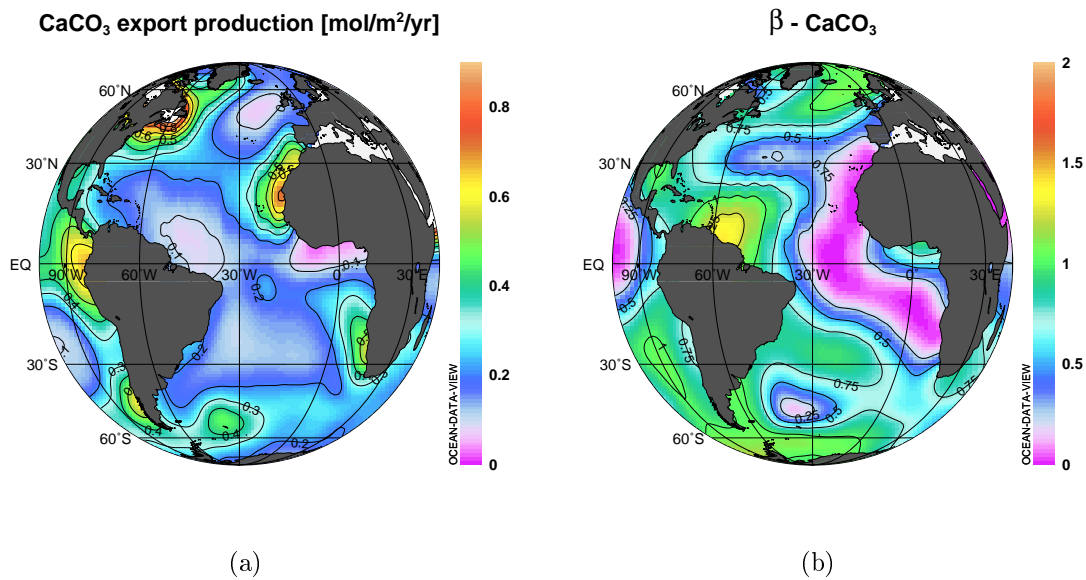


Figure 3.11: $CaCO_3$ export production (a) and remineralization scale length β (b)

Export production of $CaCO_3$ generally coincides with organic carbon export. High exports are found in upwelling regions and near the PFZ. The remineralization scale length for $CaCO_3$ is very different from remineralization of organic carbon. In a bow from North- to South Africa, parameter β ceases to almost zero resulting in higher deep sea fluxes in the eastern part of the Atlantic. That means that almost

all particles reach the very deep ocean (this east-west difference is also reflected in a strong gradient in $CaCO_3$ accumulation rates, see Section 5).

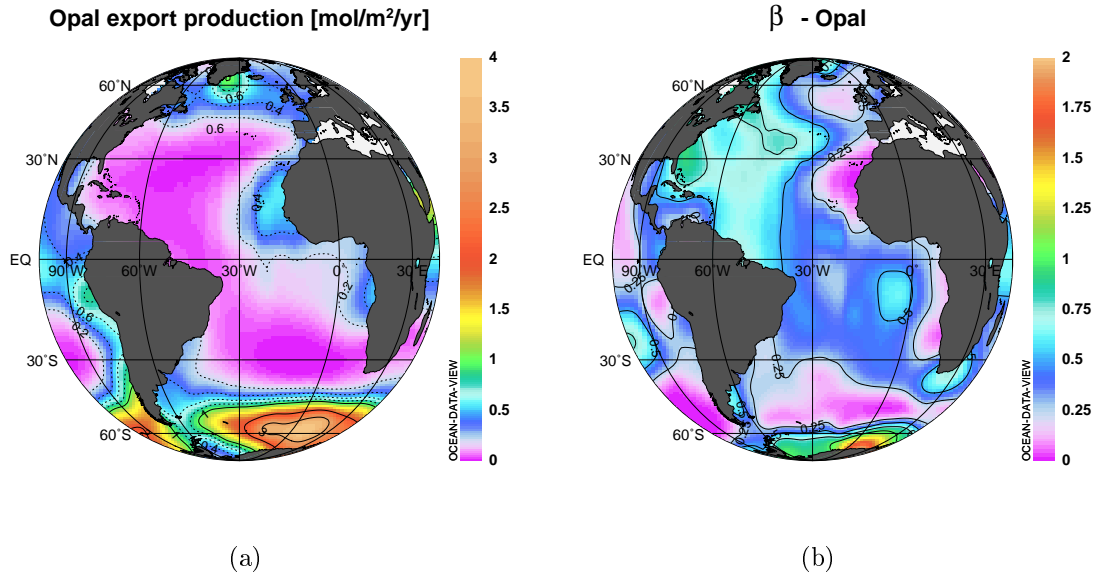


Figure 3.12: *Opal* export production (a) and remineralization scale length β (b)

Figure 3.12 shows model *Opal* export production and remineralization scale lengths. Two very different regimes of *Opal* flux are found in the Atlantic. North of approx. 40°S, *Opal* export is relatively low and coupled to export of organic carbon, i.e. export production is enhanced along the eastern boundaries and between Greenland and Scotland. Remineralization is moderate, *Opal* fluxes decrease slower than organic carbon ($\beta \leq 1$). This is in agreement with observations in sediment traps and surface sediments (see, for instance DeMaster (1991), Ragueneau et al.(1997)). It is generally found that particles become enriched in *Opal* relative to organic carbon during sinking and early diagenesis at the sea floor because of preferred C_{org} degradation.

South of ca. 40°S, *Opal* exports drastically increase and *Opal* remineralization is very fast south of ca. 55°S. The exceptionally high *Opal* exports and the dramatic change in remineralization rates in the South Atlantic is discussed in greater detail in Section 6.

Table 3.3 summarizes export production rates from experiment REF for the Atlantic averaged over latitudinal bands.

	90°N	60°N	30°N	EQ	30°S	60°S
	–	–	–	–	–	–
	60°N	30°N	EQ	30°S	60°S	90°S
Total Area [$10^{12}m^2$]	5.56	15.2	18.0	20.1	24.1	5.31
Literature						
PP $C_{org}[\frac{molC}{m^2y}]^{1)}$	4.19	4.22	9.22	4.77	5.62	6.18
EP $C_{org}[\frac{molC}{m^2y}]^{2)}$	0.59	0.62	1.97	0.82	1.07	1.27
Model export						
$C_{org}[\frac{molC}{m^2y}]$	1.49	1.62	2.48	2.73	2.43	1.49
$CaCO_3[\frac{molC}{m^2y}]$	0.22	0.29	0.19	0.19	0.25	0.23
$Opal[\frac{molSi}{m^2y}]$	0.34	0.22	0.14	0.11	1.06	1.33
Weight ratios ³⁾						
$CaCO_3/C_{org}$	0.15	0.18	0.08	0.07	0.10	0.16
$Opal/C_{org}$	0.54	0.31	0.13	0.10	1.02	2.09

Table 3.3: Mean export fluxes for latitudinal bands in the Atlantic (global model grid from 70°W to 30°O) from experiment REF.

1) PP: Primary production after Berger et al.(1987)

2) EP: Export production calculated from PP using Eppley and Peterson’s (1979) relation

3) Weight ratios are calculated from molar ratios using 1 mol $C_{org} \cong 12$ g and 1 mol $CaCO_3 \cong 100$ g

Model export production is higher for all bands in Table 3.3 compared to exports from Eppley and Peterson (1979). High exports are thus not due to a local effect but the model produces overall higher particle fluxes (compared to Eppley and Peterson (1979)) to obtain satisfying nutrient distributions. Export production of organic carbon is highest between the equator and 30°S where Eppley and Peterson’s exports are low. This discrepancy is mainly due to the very high model exports in the Namibia upwelling system.

North and south of these latitudes, C_{org} exports decrease about 2/3 of maximum productivities at high latitudes.

$CaCO_3$ exports are symmetrically around the equator with lowest specific export rates at low latitudes. $CaCO_3/C_{org}$ ratios tend to be higher in the North Atlantic which is in agreement with the general finding that the Atlantic, in particular the northern part, is a carbonate-dominated system. It should again be pointed out that results for $CaCO_3$ are not to be overrated (with respect to distribution and magnitude) because of weak constraints.

$Opal$ export production is generally higher in high latitudes with a strong trend of highest exports in the Southern Ocean. This finding is in agreement with distributions of dissolved silica which also show a strong north-south gradient (c.f. Fig. 3.8). Tréguer and van Bennekom (1991) report a mean production weight ratio $Opal/C_{org}$

of 0.3 in living phytoplankton which is lower than the global ratio derived with the adjoint model (≈ 0.5). As already mentioned above, many studies report an enrichment of *Opal* relative to organic carbon in sinking particles due to faster degradation of C_{org} . Since model export is the flux at 133m depth for the whole model domain, model results do not contradict common biological knowledge.

However, as can be seen in Table 3.3, *Opal*/ C_{org} -ratios are highly variable. The high regional variability with high values in the Southern Ocean is in agreement with recent findings (Nelson et al. (1995), Ragueneau et al. (1997)).

4 Particle fluxes in the water column: Sediment traps

In this section, particle fluxes measured in sediment traps are compared to model results. The assimilation of sediment trap data and sensitivity of the model with respect to these data is also discussed.

Sediment traps are used to measure lithogenic and biogenic particle fluxes in the ocean. Sediment trap measurements are the only way to directly record seasonality and interannual variability of particle fluxes in the deeper water column. Moorings are deployed for varying time periods to catch sinking particles. Ideally, at least two traps are positioned such that none of the traps is located within the mixed surface layer nor in the nepheloid layer near the seafloor. Usually the traps are moored for at least one year to measure the seasonal cycle of particle fluxes. Each trap contains several sample cups which are changed automatically under the sampling device. Time series with different resolution are obtained depending on the total sampling period.

Sediment trap measurements yield interesting information about total mass flux, composition of particulate matter, and changes of particle composition with depth. Many different methods have been tested to link sediment trap fluxes not only to export fluxes but also to primary production. This is crucial because estimates of primary production are updated frequently. Further, it turned out that export ratio (the *f*-ratio) and deep sea fluxes strongly depend on the particular environment. Seasonality (Berger and Wefer (1990), Bacon et al. (1985), Deuser et al. (1981), Fischer (1988)), particle size, and zooplankton grazing (Wassmann (1993), Wassmann and Slagstad (1993), Walsh et al. (1988)) seem to be important factors controlling the 'f-ratio', sinking, and conservation of particles.

An intercomparison of sediment trap data from different environments was given by Lampitt and Antia (1996). Despite of the conclusion that flux properties are highly variable they apply the flux equation of Martin et al. (1987) ($J \propto z^{-0.858}$) to 'normalize' measured fluxes to 2000m depth. After all they conclude that a link between fluxes to 2000m depth and primary production can be drawn. Looking at the raw data and original publications this conclusion seems to be obsolete. Usually authors calculate the degradation (the exponent of *z*) from the differences between upper and lower traps and a wide variety of parameter values for β is obtained. The results from adjoint modeling in Section 3 also indicated that a unique value (as in Martin et al.'s (1987) equation) probably does not exist for the the whole ocean.

Sediment trap data have relatively high errors and it is still questionable whether traps sample vertical particle fluxes quantitatively (c.f. the discussion in Section 4.1 and, e.g. Deuser et al. (1981), Baker (1988), Buesseler (1991), Gust et al. (1994), Murnane et al. (1996), Valdes et al. (1998)). 'Normalization' of sediment trap data is an elaborate problem and absolute values of vertical fluxes are difficult to interpret. Nevertheless, sediment trap data are included as direct flux measurements in the model calculations. The assimilation of sediment trap data in the model calculations can give indications whether non-normalized particle fluxes measured in sediment traps are consistent with general oceanography and budgets of dissolved

nutrients.

Another problem is that sediment trap data are point data and is it not clear whether they are representative for a larger area. Sediment traps are often deployed at very special locations where either exceptionally high fluxes and/or high seasonality is expected. Depending on model resolution, for many sediment trap locations the model grid might be too coarse. If sediment trap data agree with data of dissolved nutrients at a certain grid cell trap data will be reproduced easily. If, on the other hand, sediment trap data cannot be reproduced this can have several reasons:

- The grid is too coarse at that location (averaging over an area with strong gradients), respectively the sediment trap data are not representative for a larger area.
- Sediment fluxes were not collected quantitatively. It has been found in many studies that under- and oversampling of particles in sediment traps occurs (see also discussion below).
- The model produces unrealistic particle fluxes (e.g. due to an unrealistic upwelling). This might happen in areas with very strong hydrographic gradients.

Sediment trap data used for comparisons in this work, assimilation of data into the model, and experiments performed are described in the next sections.

4.1 Data

Within German Joint Research Project 261 (SFB261) sediment traps have been deployed in the South Atlantic since 1983. Fig. 4.1 shows the schedule for traps of SFB261. At some positions, traps were replaced several times for long-term studies but others were deployed for short-term observations only. Names of the sediment traps indicate trap positions. For instance, 'KG' stands for King George Island. Numbers indicate sampling period, i.e. numbers ≥ 1 are given for follow ups.

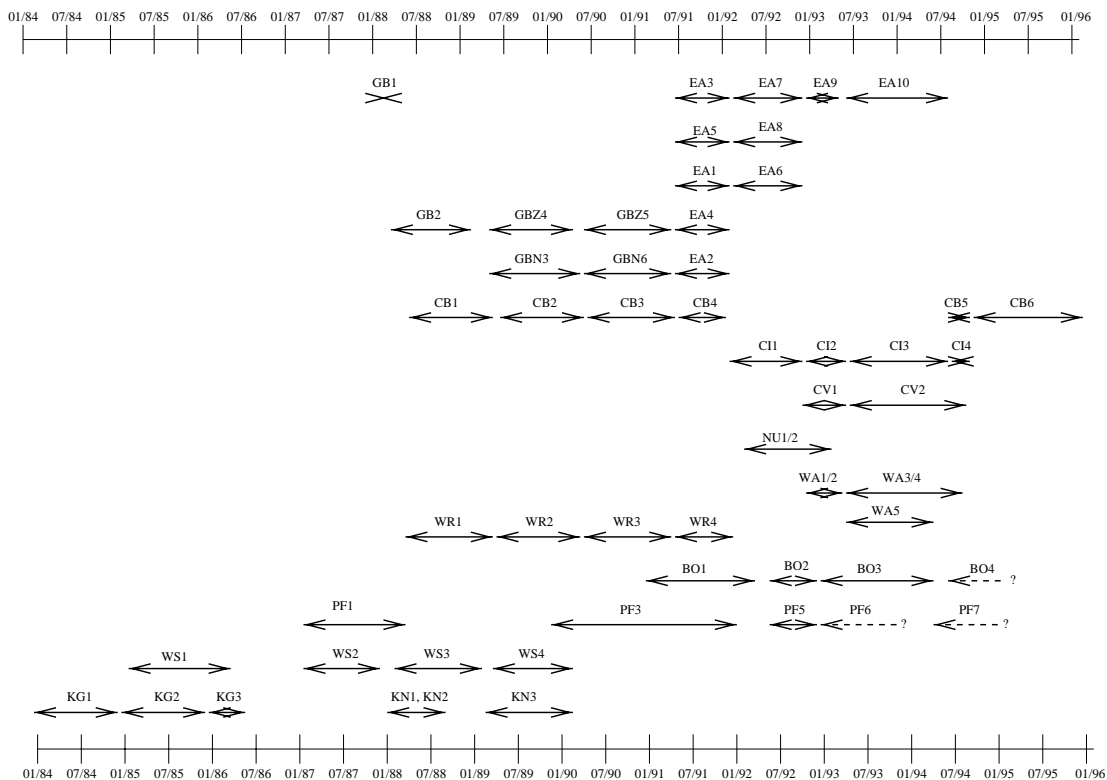


Figure 4.1: Schedule of sediment trap moorings deployed by SFB261

Moorings positions are shown in figure 4.2. Here, additionally the positions of the “JGOFS North Atlantic Bloom Experiment” (NABE) and “Bermuda Atlantic Time Series” (BATS) are given. For these traps, the raw data are available (NABE: (Honjo and Manganini, 1993), data: (NABE, 1998); BATS: (Deuser et al., 1981), data: (BATS, 1998)) and were assimilated together with data from SFB261 into an Ocean Data View collection (ODV: (Schlitzer, 1999b)) for further processing. The data from SFB261 data were supplied by Dr. G. Fischer (University Bremen) and are mostly published (Fischer (1988, 1996, 1998), Fischer and Wefer (1996, 1998), Fischer et al. (1996)).

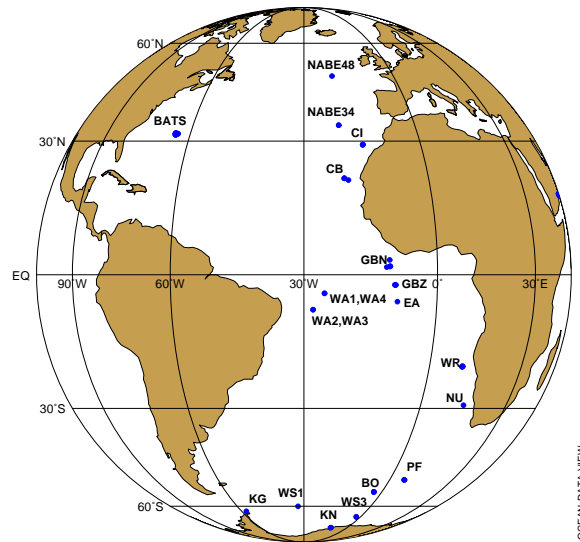


Figure 4.2: Sediment trap mooring positions in the Atlantic

Fig. 4.3 shows all flux data versus depth.

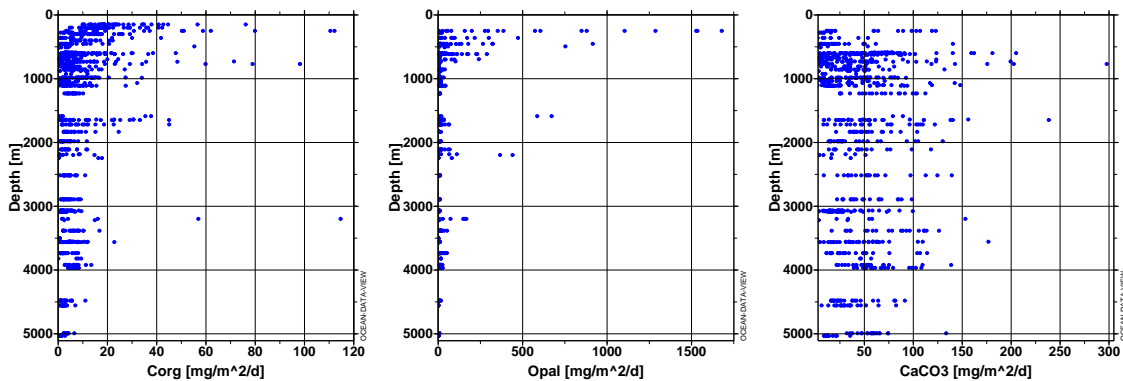


Figure 4.3: Fluxes of C_{org} , $Opal$, and $CaCO_3$ vs. depth

Generally, C_{org} and $Opal$ show fluxes decreasing with depth but the depth dependence of $CaCO_3$ fluxes appears rather unsystematic. Looking at the individual trap measurements reveals that fluxes of $CaCO_3$ and $Opal$ are often higher in deep traps. Lithogenic fluxes (not shown) show similar results indicating that either the upper traps do not catch effectively or lateral inputs are included in deep traps. Still, sediment traps bear interesting information about particle distribution in water column, particle composition and seasonality of particle fluxes. In Fig. 4.4, flux data are displayed over “day of year”. Date of a flux measurement is the start time of a sampling interval. Fig. 4.4(a) shows the time series of all sediment trap data in low and mid latitudes ($50^\circ N - 50^\circ S$). Particle fluxes are present throughout the year. The sediment traps south of $50^\circ S$ (c.f. Fig. 4.4(b)) show a very strong signal

in austral summer (December and January) with almost vanishing fluxes otherwise. The extremely high particle fluxes occur in a short period when sea ice is absent. Because of the different sampling periods of the sediment traps, all raw data were inspected carefully. Sampling intervals vary generally from 10 to 30 days but sometimes only one bottle was recovered giving the integral of a long time (max. 304 days).

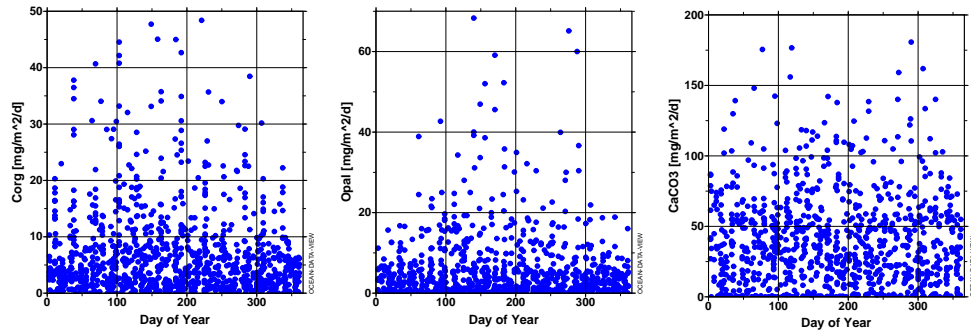
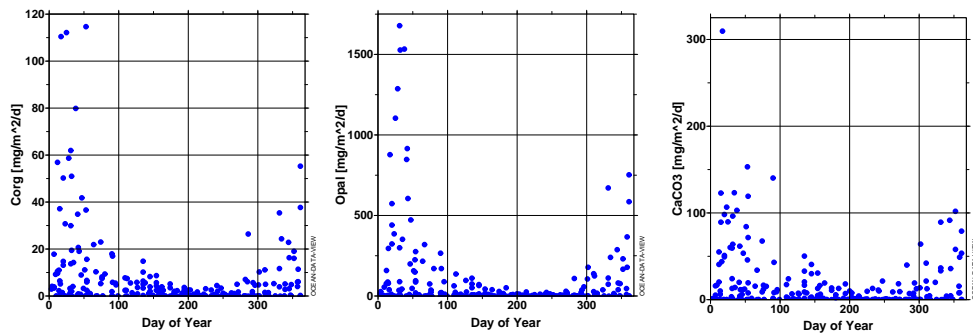
(a) $50^{\circ}N - 50^{\circ}S$ (b) $< 50^{\circ}S$

Figure 4.4: Particle fluxes over time

For the comparison with model particle fluxes (representing long-term mean fluxes), mean annual fluxes were calculated from the raw data of C_{org} , $Opal$ and $CaCO_3$. Table 4.1 summarizes all averaged sediment trap data. For moorings that were deployed for a whole year, annual mean fluxes are determined directly by integrating measured fluxes. Other moorings with short or irregular sampling were treated specially::

- KN1 trap was moored directly off Kap Norvegia, Antarctica. Data were collected in a period of 53 days only. Sea ice is present most of the year and thus the flux collected within 53 days of ice-free sea surface was taken as the integrated annual flux.
- EA8 (Eastern Equatorial Atlantic) was deployed for 296 days. Since the sea-

sonality is very low at the equator the flux was multiplied by 365/296.

- CV1 (181 days) and CV2 (498 days) (Cape Verde Islands) were deployed in a series. Integrated flux (679 days) was multiplied by 365/679.
- CB2 (374 days) and CB3 (379 days) (Cape Blanc) were also deployed in a series. Integrated flux (718 days) was multiplied by 365/718.
- BO1 (Bouvet Island) was deployed for 460 days between December 1990 and April 1992. This trap shows high seasonality with high particle fluxes from January to the end of March and low fluxes otherwise. The interannual variation was relatively high and two high-productive sequences were covered by that time series. The data were averaged (multiplied by 365/460) in order to get a better estimate for annual fluxes.
- WS1 (Weddell Sea) shows a seasonal signal with high particle fluxes in February. The mean particle flux was taken from Fischer (1988).
- BATS traps were deployed for up to two years. Here, seasonality was very low. Data (BATS, 1998) were averaged over the whole period.
- NABE traps show a seasonal signal, mean values were taken from Honjo and Manganini (1993).

Close inspection of particle fluxes in Table 4.1 reveals that the data do not represent vertical decreasing particle fluxes in all cases. For instance, trap EA8 shows higher fluxes in the middle trap at 1833m depth than in the shallow trap at 598m for all components. This *might* be due to undertrapping of the shallow trap *or* by lateral input into the middle trap. Fluxes *increasing* with depth are also found for other moorings: GBN3 ($CaCO_3$), GBN6 ($CaCO_3$, *Opal*), and WA4 ($CaCO_3$). Trap data for the assimilation into the model were selected in cooperation with G.Fischer who deployed and recovered the traps and also performed most of the measurements of C_{org} , $CaCO_3$, and *Opal*. Choices were made dependent on reliability of data and/or trap position (possibility of lateral inputs).

Trap	LAT ° N	LON ° E	Depth m	Days	Notes	Corg [$\frac{mol}{m^2y}$]	CaCO3 [$\frac{mol}{m^2y}$]	Opal [$\frac{mol}{m^2y}$]
KN1	-71	-12	250	53	+	0.1583	0.035	0.533
WS3	-65	-3	360	368	+	0.1942	0.02934	0.413
KG1	-62	-58	1600	360	+	0.3583	0.05	0.65
WS1	-62	-35	900	418	+	0.0025	0.0001	0.005
BO1	-54	-3	453	460	+	0.225	0.118	0.893
PF3	-50	6	700	366	+	0.2808	0.1137	0.398
NU2	-29	13	768	361	+	0.5762	0.3772	0.007
WR1	-20	9	1640	376	- ¹	0.5217	0.3386	0.147
WR2u	-20	9	608	360	- ²	0.4167	0.2182	0.067
WR2l	-20	9	1654	360	+	0.3142	0.2388	0.051
WR3	-20	9	1648	361	- ³	0.235		
WA3u	-8	-28	671	350	+	0.0792	0.0622	0.007
WA3l	-8	-28	5031	350	+	0.0246	0.0354	0.005
WA4u	-4	-26	808	375	- ²	0.155	0.1247	
WA4l	-4	-26	4555	375	+	0.0813	0.1353	
EA8u	-6	-9	598	296	- ⁴	0.2267	0.1745	0.023
EA8m	-6	-9	1833	296	+	0.1967	0.1912	0.03
EA8l	-6	-9	2890	296	- ⁵	0.1192	0.1874	0.024
GBZ4	-2	-10	696	365	- ⁶	0.093	0.055	0.013
GBZ5u	-2	-10	597	360	- ⁴	0.25	0.119	0.025
GBZ5l	-2	-10	3382	360	+	0.1917	0.263	0.097
GBN3u	2	-11	856	361	- ⁴	0.251	0.145	0.057
GBN3l	2	-11	3965	361	+	0.181	0.199	0.077
GBN6u	2	-11	859	360	- ²	0.25	0.166	0.103
GBN6l	2	-11	3965	360	- ⁷	0.175	0.241	0.077
CV1u,CV2u	11.5	-21	1000	679	+	0.2239	0.117	0.0582
CV1l,CV2l	11.5	-21	4500	679	+	0.106	0.103	0.0434
CB2,CB3	21	-20	3525	718	+	0.5042	0.692	0.095
BATS1	31.5	-64.1	150	785	+	0.776		
BATS2	31.5	-64.1	200	785	- ⁸	0.596		
BATS3	31.5	-64.1	300	785	- ⁸	0.429		
BATS4	31.5	-64.1	400	314	+	0.374		
NABE48	34	-21	4500	728	+	0.075	0.13	0.033
NABE34	48	-21	3700	728	+	0.0833	0.15	0.1

Table 4.1: Annual particle fluxes of C_{org} , $CaCO_3$ and $Opal$ (explanations concerning averaging procedure see above). Fluxes assimilated in the model are marked “+”, rejected values are indicated by “-”.

1 Alternative to trap WR2l, 2 $CaCO_3$ increases with depth, upper trap probably undertrapping, 3 Alternative to trap WR2l, data for C_{org} only, 4 $CaCO_3$ and $Opal$ increase with depth, upper trap probably undertrapping, 5 c.f. EA8u, EA8m most reliable (pers. comm. Dr. G. Fischer), 6 Alternative to GBZ5, 7 Alternative to GBN3u, 8 Vertical model resolution.

4.2 Experiments with assimilated sediment trap data

Sediment trap data marked '+' in Table 4.1 were assimilated into the model. Different experiments were carried out to test whether sediment trap data and budgets of dissolved nutrients are conflicting or yield the same information about particle fluxes. Sediment trap data are included as soft constraints (c.f. Section 2).

In this section, five model solutions are compared with respect to the trap constraint (REF, HANT, LAT, SLAT, and SLANT c.f. Tab. 2.5).

- **REF, HANT:**

In experiments REF and HANT, no sediment trap data were assimilated. Fluxes are exclusively determined by budgets of dissolved nutrients and smoothness constraints. The difference between these experiments is that sediment accumulation rates calculated in HANT. This is discussed in Section 5.

- **LAT:**

Experiment LAT was forced to accurately reproduce assimilated sediment trap data by setting very high weight factors in the costfunction. All other weight factors were kept as in experiment HANT. This led to 'singularities' in the parameter fields (see below). Initial parameter fields were the same as in experiment HANT.

- **SLAT:**

Experiment SLAT is a subsequent run of experiment LAT. Weight factors for sediment trap data were decreased. Weight factors for the smoothness constraints of export production and remineralization were increased.

- **SLANT:**

Experiment SLANT is a subsequent run of experiment SLAT. Weight factors for sediment trap data were reduced by 23 orders of magnitude, i.e. the model was effectively not longer forced to reproduce the data.

Experiments REF, HANT, LAT, and SLAT were run for about 70,000 iterations each. Experiment SLANT is a 'relaxation' from experiment SLAT and was run for 10,000 iterations only.

4.2.1 Organic carbon fluxes, some examples

The model fluxes and sediment trap data are compared for four positions in the South Atlantic to illustrate the different model solutions. WA3 is a sediment trap in the western Atlantic near the equator, WR3 (Walvis Ridge) is located in an eastern Atlantic upwelling region, BO (Bouvet Island) is moored in the western Weddell Sea, and WS1 (Weddell Sea) lies in the central western Weddell Gyre (c.f. Fig.4.2).

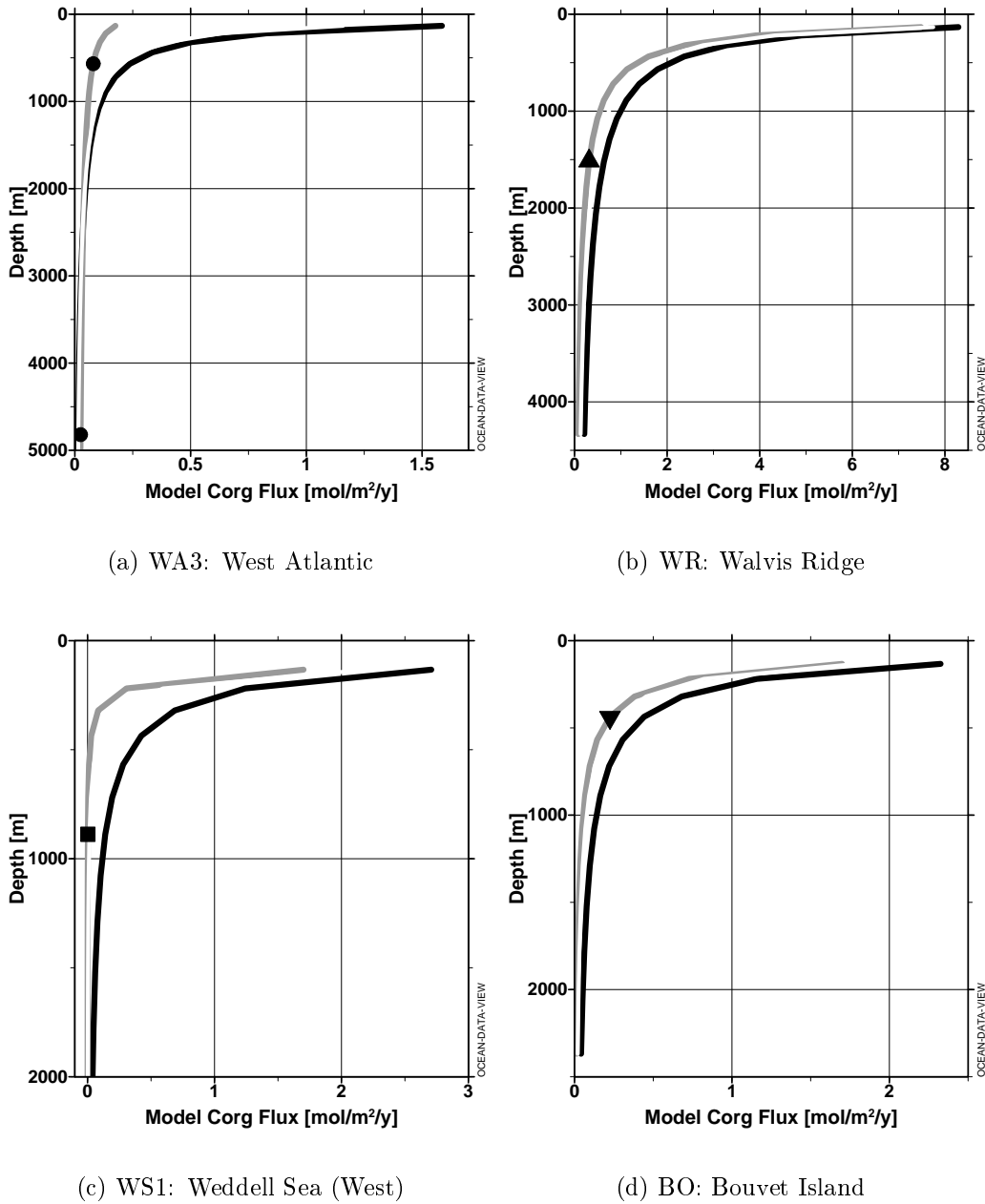


Figure 4.5: C_{org} model fluxes from experiment HANT (black) and LAT (grey). Sediment trap data are displayed as filled marks.

Fig. 4.5 shows model C_{org} fluxes at the four trap locations in the South Atlantic for experiments HANT (black line) and LAT (gray line). Fluxes from HANT and LAT were chosen because these fluxes exhibit largest resp. smallest deviations from sediment trap data. Sediment trap data are displayed as filled marks. Model fluxes start at 133m water depth, where export production is defined. Below this 'model euphotic zone', fluxes follow equations $J(z) \propto 1/(z^\beta)$, where β describes the 'steepness' of particle flux decrease with depth (c.f. Section 2.7).

In all examples given in Fig. 4.5, fluxes from experiment HANT are higher than

fluxes from experiment LAT and sediment trap data. Export production in experiment HANT is up to a factor of about 9 higher (trap WA3, Fig. 4.5 (a)) than in experiment LAT. Due to higher export production and sometimes also deeper remineralization, fluxes reaching the deep ocean are higher in experiment HANT. The 'biological pump' is more effective in experiment HANT, at least at the example positions given here. But the black lines do not lie near the sediment trap data and are thus not in agreement with direct flux measurements.

Particle fluxes from experiment LAT (grey lines) almost exactly match the sediment trap data. Model fluxes of experiment LAT could be considered to be a very good representation of sediment trap data. Inspection of the model fields (export production and remineralization scale length β) shows that in this solution, the biogeochemical parameters were changed *at* the locations of sediment traps only. The local changes are comparably large. This is illustrated by plotting the difference of the parameter fields between experiment HANT and LAT in the South Atlantic. Figs. 4.6 and 4.7 show the difference of export production rates and remineralization scale length between experiment HANT and LAT for organic carbon. The trap positions from the examples given in Fig. 4.5 are clearly seen. Differences between model solutions HANT and LAT occur exactly *at* the trap positions, the neighbourhood remains relatively unaffected. The discontinuities occur in experiment LAT, whereas experiment HANT exhibits smooth distributions of export production and remineralization scale length comparable to the reference experiment REF described in Section 3.3.

This is probably due to the very high weight factors for the 'trap constraint' in the costfunction while keeping all other weight factors constant. Obviously, all other constraints, like deviations to data of dissolved nutrients and smoothness, 'lost' against the sediment trap constraint: The sediment trap data are reproduced accurately but the parameter fields seem to be unrealistic. Due to the discontinuities in the parameter fields, LAT is not considered a satisfying solution.

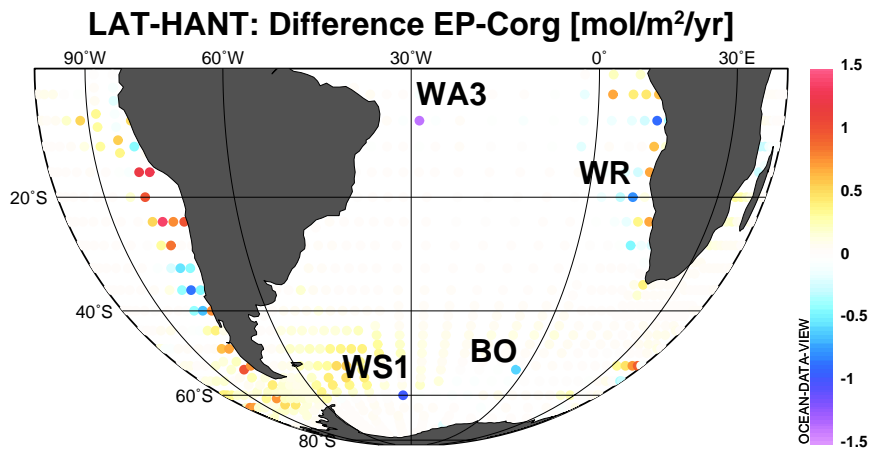


Figure 4.6: Differences of export production rates between experiments HANT and LAT.

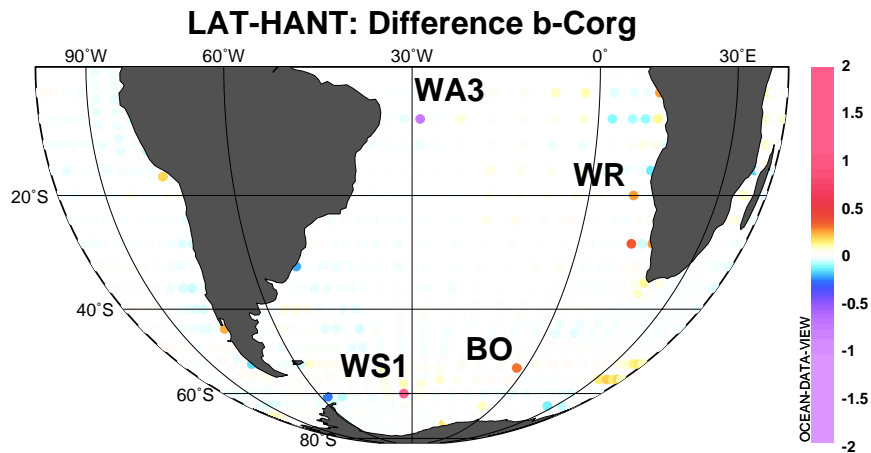


Figure 4.7: Differences of remineralization scale lengths between experiments HANT and LAT.

SLAT, a subsequent model run was performed to 'smoothen out' the parameter fields. Weight factors of smoothness constraints for export production and remineralization were increased to avoid abrupt changes as occurred in experiment LAT, whereas weight factors for sediment trap data were reduced. The discontinuities are not seen in the resulting parameter fields. Resulting particle fluxes for the examples above are between fluxes of experiments HANT and LAT. I.e., compared with experiment LAT, export production increases and particle fluxes reach deeper layers of the ocean. Sediment trap data are not as well reproduced as in experiment LAT.

4.2.2 Model fluxes vs. sediment trap data

Model fluxes of C_{org} , $CaCO_3$, and $Opal$ are compared with sediment trap data. The model fluxes are shown for both extreme experiments HANT and LAT for which examples were given above. Figs. 4.8 to 4.9 show calculated model fluxes vs. sediment trap data for C_{org} , $CaCO_3$, and $Opal$. Shallow (0m-2000m) and deep (> 2000m) traps are displayed separately. Sediment trap data (x-axis) and corresponding model fluxes (y-axis) for the shallow traps are given on the left sides in the figures (a) each, and for the deep traps on the right side (b), respectively. Generally, the differences between fluxes constrained to reproduce sediment trap data (crosses) and unconstrained (circles) model fluxes are relatively small at the positions of the deep traps (b). This is understandable by looking again at the examples given in the last section and recalling the definition of particle flux equations. A power law reduces particle fluxes mostly in shallow waters. A slight change in export production and/or particle remineralization has largest effects near the surface whereas deep particle fluxes are only slightly changed. To change a -small- deep particle flux requires large changes in the parameters for export and remineralization, respectively. In the shallow traps ((a) in Figs. 4.8 to 4.10), model particle fluxes for the unconstrained model (circles) are systematically higher than measurements. In most cases, deviations are reduced to almost zero applying the trap constraint with

high weight factors (LAT, crosses).

The particle fluxes derived in experiments REF, SLAT, and SLANT are not shown in detail. Particle fluxes from these experiments generally are between fluxes from experiment HANT and LAT.

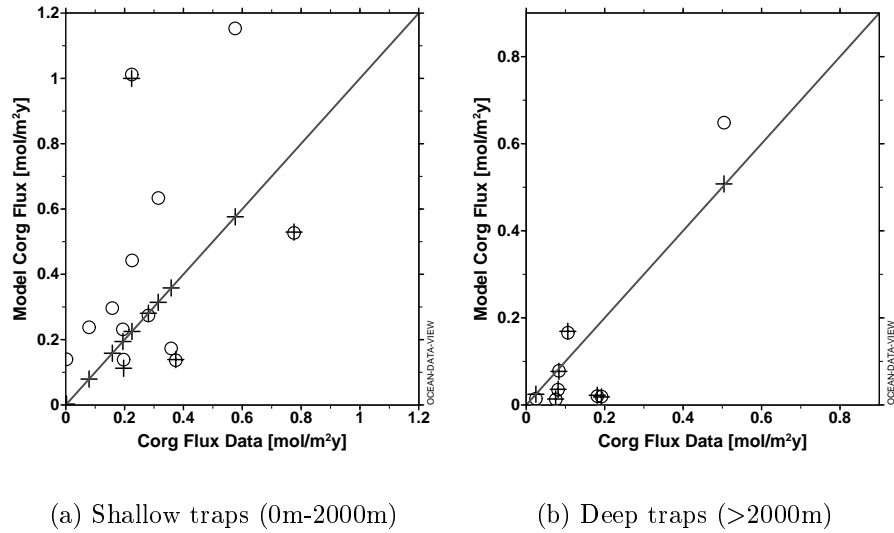


Figure 4.8: C_{org} model fluxes vs. sediment trap data for the unconstrained model HANT (circles) and the model constrained with sediment trap data LAT (crosses). Solid line: 1:1 relation

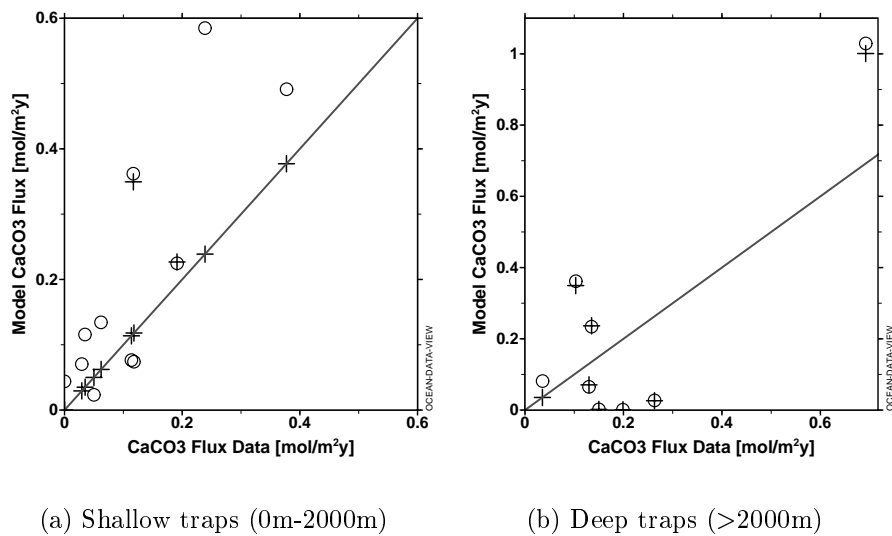


Figure 4.9: $CaCO_3$ model fluxes vs. sediment trap data for the unconstrained model HANT (circles) and the model constrained with sediment trap data LAT (crosses). Solid line: 1:1 relation

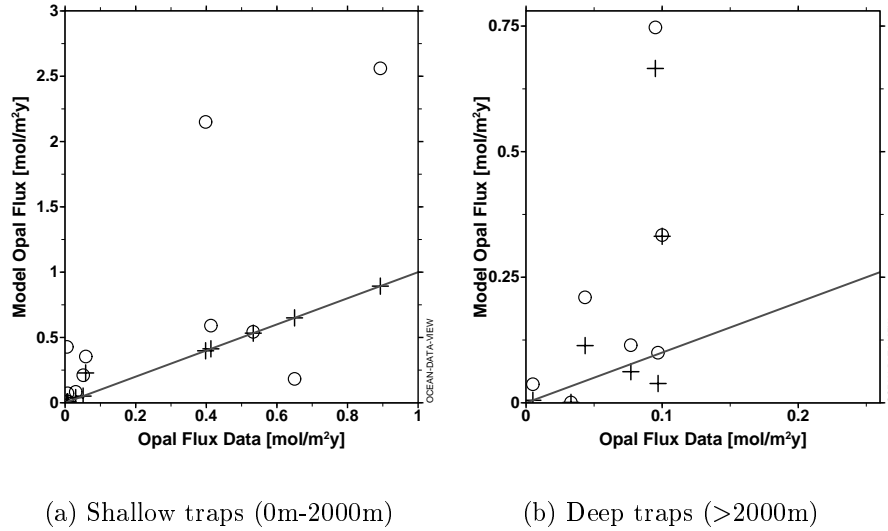


Figure 4.10: *Opal* model fluxes vs. sediment trap data for the unconstrained model HANT (circles) and the model constrained with sediment trap data LAT (crosses). Solid line: 1:1 relation

Table 4.2 summarizes mean deviations of model fluxes to sediment trap data for all experiments.

		REF	HANT	LAT	SLAT	SLANT
C_{org} [$mol/m^2/y$]	shallow	0.082	0.125	0.016	0.036	0.042
	deep	-0.065	-0.031	-0.047	-0.014	-0.012
<i>Opal</i> [$mol/m^2/y$]	shallow	0.387	0.376	0.016	0.022	0.329
	deep	0.099	0.156	0.109	0.106	0.108
$CaCO_3$ [$mol/m^2/y$]	shallow	0.037	0.078	0.024	0.025	0.035
	deep	-0.042	0.011	0.001	0.003	0.003

Table 4.2: Mean deviations of model results compared with sediment trap data ($\sum[J_{model} - J_{data}]$) from all experiments. Shallow: traps in 0m - 2000m water depth. Deep: traps below 2000m.

Generally, model fluxes at the shallow trap positions are higher than found in sediment traps. Mean deviations are positive for all components (C_{org} , $CaCO_3$, *Opal*) in all experiments. I.e., particle fluxes were calculated to be higher than measurements in all experiments.

Maximum deviations for the shallow traps are found in the unconstrained experiment HANT. The model calculations with very high weight factors (LAT) drastically reduce the deviations in the shallow traps (about one order of magnitude for C_{org} and *Opal* and to 1/3 for $CaCO_3$). This was already shown with the example fluxes in the south Atlantic in the last section where model fluxes almost exactly passed the data points (c.f. Fig 4.5). After the particle flux parameters were 'smoothed

out' in experiment SLAT, mean deviations of model fluxes to flux data again increase. Further weakening of the trap constraint in experiment SLANT (effectively setting the weights to zero) again yields increasing deviations. After 10,000 iterations only, the mean deviation of C_{org} and $CaCO_3$ is about 1/3 and 1/2 for the unconstrained model HANT. Mean deviations of $Opal$ are about the same as for experiment HANT.

It can thus be stated that the adjoint model *does not reproduce* shallow sediment trap data without massive forcing. Shallow sediment trap data are incompatible with particle fluxes derived from nutrient budgets.

At the positions of the deep sediment traps, $CaCO_3$ and $Opal$ fluxes are also higher than found in sediment traps in almost all model calculations. An exception is the $CaCO_3$ flux in experiment REF. Comparing $CaCO_3$ fluxes of experiment REF and HANT (both independent of sediment trap data) again indicates that the introduction of sediment accumulation rates has altered $CaCO_3$ fluxes. It was already shown in Section 3 that all experiments with sediment accumulation bear higher exports (and thus larger particle fluxes) for $CaCO_3$. The result that fluxes at the trap positions in experiment HANT are higher than in experiment REF is thus consistent with earlier findings.

However, the trend is the same as for the shallow traps: Mean deviations are largest in experiment HANT and lowest in experiment LAT. Reducing the weight factors successively (SLAT and SLANT) again yields increasing deviations.

Organic carbon results are different. Firstly, the deep model fluxes are *lower* than measurements. This is either due to too fast remineralization in the model experiments or because of lateral inputs into the deep traps. Too low particle exports are an unlikely reason because the results from the shallow trap positions indicate the opposite (where model fluxes are higher than measurements). Surprisingly, the effect of *underestimation* of measured particle fluxes only occurs for organic carbon.

Alltogether it can be stated that at *all* shallow trap positions the mean model particle fluxes are higher than found in sediment traps, even if the model is forced to reproduce the sediment trap data. This *might* be due to an overestimation of particle fluxes in the model calculations. More likely is that sediment traps do not catch sinking detritus quantitatively, especially in shallow water. As pointed out in the discussion of the sediment trap data in Section 4.1, increasing fluxes (with depth) are found in several moorings.

It has been known from many studies that sediment trap efficiency is influenced by many processes. Gust et al. (1994) showed that different deployments of sediment traps (surface tethered and bottom moored) yield very different collection behavior. Even using the same geometrical collection device the sampling efficiency (ratio of collected material to 'true' rain rate) was influenced differently by hydrodynamics and turbulences (Gust et al., 1994).

'Swimmers' can enter the traps to feed on the collected material. Nekton entering the traps is commonly removed from the samples but this might cause biasing of data, too.

Further, the material collected remains in the sampling device for weeks to months and degradation occurs. Khripounoff and Crassous (1994) compared poisoned (using $HgCl_2$) with non-poisoned traps. They found that poisoning leads to better preservation of organic carbon in deep traps but increases the rate of calcite dissolution.

Determining trapping efficiencies was identified to be a major problem limiting the quantitative interpretation of sediment trap data. It has been suggested that radionuclides can be used to calibrate sediment traps. The radionuclide most commonly used is ^{230}Th which is highly particle reactive and has a known production rate in water column (radioactive daughter of ^{234}U). Sinking particles scavenge dissolved ^{230}Th and total ^{230}Th concentration becomes a function of water depth only (constant flux model, see Bacon et al. (1985)). Particulate ^{230}Th found in sediment traps is used to normalize total particle fluxes. Bacon et al. (1985) showed that this method should only be used to normalize long-term moorings (at least one year) because in shorter periods, production and scavenging of ^{230}Th not always is in exact balance. Further, they point out that even the normalization of long-term moorings bears errors caused by advective processes. However, the normalization of sediment trap data using radionuclides is widely used and is an improvement for the interpretation of sediment trap data.

The adjoint method is a new, independent approach to get meso-scale estimates of particle fluxes. The results obtained in this work agree with earlier findings that sediment traps tend to underestimate vertical particle fluxes, especially at shallow water depths. Inverse modeling thus may help to understand conflicting interpretations of sediment trap data and to further constrain sediment trap data normalization.

5 Accumulation of biogeneious particles

Deep sea sediment cores are the almost *only* source of information about marine environments in geological history. The understanding of the recording of upper ocean processes in deep sea sediments is a basic task of marine geology. As was already pointed out in preceding sections, signals of primary production are modified in many ways. Particle fluxes to the sea floor are non-linearly linked to either export or primary production. At the sediment-water-interface, modification of signals continues. Early diagenesis of surface sediments is influenced by the special conditions at a given location. For instance, organic carbon accumulation depends on grain size, $CaCO_3$ accumulation on water depth, and *Opal* conservation on sedimentation rate, and more. This list is far from being complete and non-linear dependencies of preservation on sediment composition probably exist. Further, conservation generally depends on physical properties of bottom waters (current velocity, alkalinity, temperature etc.). Geological interpretation of cores is challenging because one has to consider all possible processes of signal modification. The 'natural way' to proceed is to firstly study the surface sediments which represent the modern environment. Contents of organic matter, calcite, opal, and terrigenous particles give an estimate of integrated signal transformation at a given location. Then, variations with depth (in a sediment core) are interpreted as changes in surface production and/or deep water properties with time and are connected with geological cycles (e.g. Milankovitch cycles). Physical and chemical properties of the sediment (e.g. stable isotopes and radionuclides, magnetic orientation and susceptibility) and biological indicators (microfossils) are used to date horizons in a sediment core. From these horizons, the age of sediments is calculated. A basic parameter is thus the sediment accumulation rate which maps thickness versus age. Without knowing the modern sedimentation rate (and thus, together with sediment composition, accumulation rates of all components) a connection between ocean properties and geological signal formation is problematic. Paleoreconstructions of marine environments can only be performed by understanding the 'signal coding' at the particular station.

5.1 Sediment accumulation rate data

Firstly, it should be pointed out that currently no sediment accumulation rate data are assimilated into the present model for several reasons:

- The database for sediment accumulation rates is rather sparse. Maps of sediment accumulation are generally compiled from few accumulation rate data (moles or gram per square meter and time). The maps of Lisitzin (Lisitzin, 1996) and Archer (1996a, 1996b) are based on data of percentage sediment composition and different models are used to estimate flux rates from these data.
- Accumulation rates for surface sediments are difficult to determine in vast regions of the ocean, especially where sediment accumulation is low. Many

surface accumulation rates represent mean values for the last 11000 to 12000 years. This is due to the last glacial/interglacial transition often being the most recent dateable event in a sediment core.

- Recently, a discussion arose about the reliability of accumulation rates from individual stations in areas with poor sampling coverage. Probably all data have to be corrected for focusing and erosion. Sediment redistribution seems to be common, even for deep sea sediments.
- Geological samples are usually from special locations which do not represent a mean accumulation rate for an area of about 2×2.5 degrees which is required for direct assimilation into the model.

No geological data and no functional a priori knowledge is included in the model calculations. Instead, in this model, sediment accumulation rates are exclusively calculated based on nutrient budgets. This approach is equivalent to the budget calculations to optimize particle fluxes in the water column already described earlier in this manuscript. The model optimizes the *mean* nutrient sink at the sea floor which is compatible to physical and biogeochemical cycles determined by the other model parameters *and* data of dissolved nutrients in the bottom box. The optimum model nutrient sink is an indirect measure of the mean accumulation rate and is calculated independently of geological data. As pointed out above, geological sediment accumulation rates are point data and usually show strong variations on small scales. Mean accumulation rates calculated on a the global grid described in Section 2.3 may be very different from geological accumulation rate estimates. Accumulation rates from the adjoint model give additional information about the variability of the *mean* accumulation rates to be expected from nutrient budgets.

5.2 Model sediment accumulation rates

It was already shown that the introduction of sediment accumulation rates did not change the results drastically with respect to total costfunction. Global model-data misfits are within the same range for all experiments (c.f. Fig. 3.1 in Section 3). Sediment accumulation rates mainly influence the concentrations in the bottom layer where nutrients *can* be removed by the model. Table 5.1 summarizes changes in the bottom layer for the properties with highest data density in the model bottom layer. Comparing the mean concentrations of O_2 , PO_4 , and SiO_2 and the mean absolute deviation from experiment REF reveals that, even without sediment accumulation rates, the model reproduces the deep concentrations quite well. Deviations are of the order of a few percent of observed values only.

	Data	REF	HANT	LAT
	Mean Concentration	Absolute deviation	Absolute deviation	Absolute deviation
$O_2[\mu\text{mol}/l]$	195	8.00	7.78	7.76
$PO_4[\mu\text{mol}/l]$	2.18	0.080	0.078	0.077
$SiO_2[\mu\text{mol}/l]$	125.6	7.03	7.27	7.0

Table 5.1: Changes of model nutrient deviations in the bottom layer. All values are averaged concentrations and absolute deviations where data are available in model bottom boxes

Column 4 and 5 in Tab. 5.1 give mean, absolute deviations of experiments HANT and LAT. Introducing sediment accumulation rates only slightly changes the deviations of model concentrations compared to data. But for oxygen and phosphate, both experiments with sediment accumulation rates show lower mean deviations to data. This shows that the optimization of sediment accumulation rates has a positive effect on nutrient budgets, i.e., the adjoint model *does* vary mean accumulation rates to improve bottom nutrient concentrations. Deviations of dissolved silica are larger in experiment HANT compared to experiment REF. This indicates that initial values for sediment accumulation rate parameters of *Opal* in experiment HANT (25%) were mis-set. It was already noted in Section 3 that sediment accumulation rate initial values for *Opal* in experiment HANT seemed to be too high also for other reasons (experiment HANT reduced parameter s drastically almost everywhere in the model domain). The negative effect in bottom silica concentrations proves that indeed high *Opal* accumulation worsened the model solution. Silica concentrations are closer to data when lower start values for *Opal* accumulation rates were used (4% in experiment LAT). This gives confidence that also for *Opal*, particle accumulation can improve model distributions. The high accumulation rates from experiment HANT thus give an *upper limit* of *Opal* particle accumulation.

All together it can be stated that sediment accumulation rates determined from nutrient budgets are weakly constrained because deep water nutrient measurements represent only a small fraction of the whole nutrient dataset but an improvement of deep water nutrient concentrations (despite SiO_2 in experiment HANT) indicates that nutrient distributions provide information about accumulation of biogeneous sediments. The accumulation rates determined by the adjoint model give independent estimates which are compared to literature values in the following.

	Acc [$\frac{Tmol}{y}$]	Acc/EP $\frac{mol}{mol}$ [%]	HANT		SLANT	
			Acc [$\frac{Tmol}{y}$]	Acc/EP $\frac{mol}{mol}$ [%]	Acc [$\frac{Tmol}{y}$]	Acc/EP $\frac{mol}{mol}$ [%]
Global						
C_{org}	$3^{1)}, 0.08 - 10^{2)}$	$0.33 - 3.3^{3)}$	4.81	0.58	4.33	0.52
$CaCO_3$	$10.8^{1),7)} - 53^{8)}$	$60^{8)}$	3.73	3.6	2.95	2.9
$Opal$	$2.8^{4),7)} - 8.9^{5)}$	$3 - 9^{5),6)}$	3.72	1.8	0.81	0.4

Table 5.2: Integrated burial (Acc) and preservation (accumulation relative to export production Acc/EP) of biogenic particles for the global model domain from experiments HANT and SLANT

- 1) (Broecker and Peng, 1993): $C_{org} \approx 3 \times 10^{12} mol/y$, $CaCO_3 \approx 14 \times 10^{12} mol/y$
- 2) (Sundquist, 1985): Compilation of estimates of mean burial of organic carbon over different geological time scales. Total burial criticized by the author were excluded
- 3) (Berger, 1989): see Figure 1.3
- 4) (Lisitzin, 1985): Global: 3.7-5.53 Tmol Si
- 5) (Tréguer et al., 1995), EP: 100 - 140, ACC: 5.3-8.9
- 6) (Nelson et al., 1995): Burial/(Export at 100m) $\approx 3\%$
- 7) (Lisitzin, 1996): Mean Holocene $CaCO_3$ $10.8 Tmol/y$ (incl. terrigenous), $Opal$ $2.8 Tmol/y$
- 8) (Milliman, 1993): PP: $5.3 \times 10^9 t/y$, ACC: $3.2 \times 10^9 t/y$

The global accumulation of C_{org} from adjoint modeling is a factor of about 1.5 higher than the relatively new estimate from Broecker and Peng (1993) for present day carbon cycling. Sundquist (1985) summarized estimates from various authors varying by more than a factor of 100. These estimates were derived using different methods and give mean accumulation over different time scales. The total accumulation of organic carbon derived with the adjoint model is well in the range of these estimates and comparably close to Broecker and Peng's (1993) most recent estimate. The global mean relative accumulation rate (or preservation efficiency) of organic carbon is within the same range as proposed by Berger (1989) (see also Fig. 1.3). $CaCO_3$ accumulation is much lower than independent estimates. The adjoint model gives total $CaCO_3$ accumulation of about 1/3 of the lowest value of $10.8 Tmol/y$ proposed by Lisitzin (1996). It was already pointed out in Section 3 that $CaCO_3$ fluxes are probably generally underestimated. The 'too-low' accumulation is thus not surprising. Consistent with independent estimates, the preservation efficiency for $CaCO_3$ is higher than the preservation efficiencies of C_{org} and $Opal$ but absolute values are much lower than proposed by Milliman (1993). Due to the very different initial values for $Opal$ accumulation, $Opal$ fluxes to the sediment range from $0.81 Tmol/y$ (LAT) to $3.72 Tmol/y$ (HANT) in the model calculations. It was stated above that the accumulation from experiment HANT yields an upper limit for $Opal$ accumulation because higher accumulation conflicts with nutrient budgets. However, this upper limit is lower than the estimates of Tréguer et al. (1995) but

higher than the value from Lisitzin (1996). The preservation efficiency in experiment HANT is lower than estimates from Nelson et al. (1995) which is not only due to lower accumulation but also due to higher (than Nelson's (1995)) model export fluxes. The preferred (from nutrient budgets) low accumulation of $0.81 Tmol/y$ is much lower than estimates from Tréguer et al. (1995) and Lisitzin (1996). The relative preservation efficiency is also much lower (approx. 1/10 of the values as proposed by Nelson et al. (1995) and Tregúer et al. (1995)).

Concluding, $CaCO_3$ fluxes are, in agreement with statements given earlier, systematically too low and global particle fluxes of C_{org} into the sediment derived with the adjoint model are consistent with estimates based on other methods. Model *Opal* accumulation and preservation is lower than independent estimates but as stated earlier, silicate cycling is currently not well understood and process rates are still controversial discussed. The estimates from adjoint modeling can be used to further constrain global budgets. In the following, the spatial distributions of biogenic surface sediments is presented.

5.3 Distribution of surface sediments in the Atlantic

Figs. 5.1 to 5.3 show the distributions of modeled particle fluxes reaching the bottom boxes (a) and sediment accumulation rates (b) from experiment HANT. As already mentioned above, absolute values of accumulation rates for *Opal* are probably too high but the general pattern is the same for both experiments HANT and SLANT. It should be noted that the flux to the sea floor in the model presented here is defined as the flux reaching the bottom box. This flux is not identical with the 'rain rate to the sea floor' as often used in literature. However, for particle fluxes described with functions $\propto 1/z$, this is a minor difference because fluxes do not decrease rapidly at these depths.

Organic carbon fluxes to the sea floor occur in considerable amount only in high-productive regions (compare Fig. 5.1(a) to Fig. 3.10(a)) and/or at shallow water depth as on the Argentinian shelf and at the Greenland-Scotland Ridge. Organic carbon accumulation occurs only where high fluxes to the sea floor are found. The patterns of accumulation, flux to the sea floor, and export production thus seem to depend on primary production in a predictable way. Even if the remineralization changes over larger scales (c.f. Fig. 3.10 (b) in Section 3.3), at least the global pattern of primary production is conserved in the sediments.

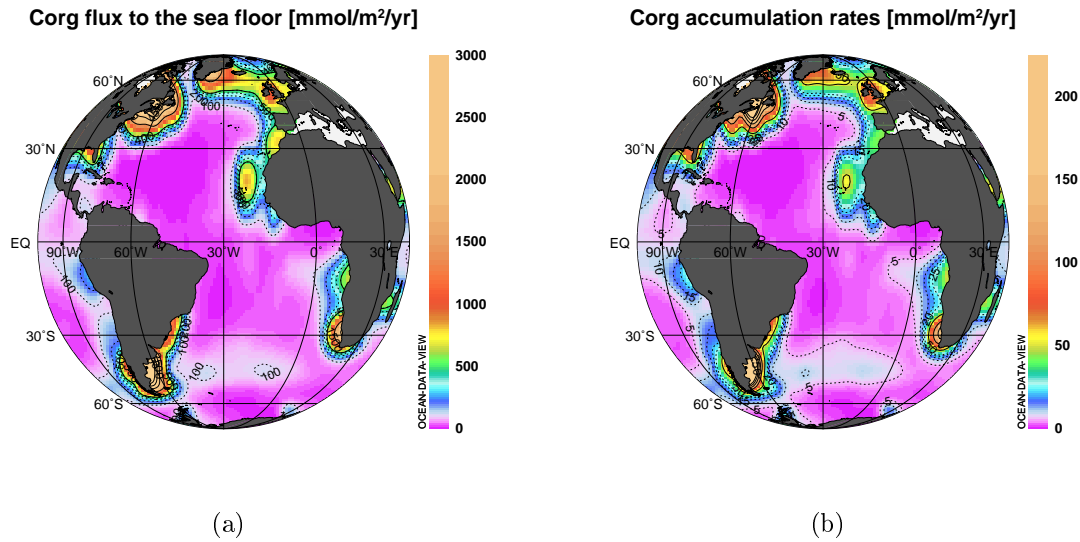


Figure 5.1: C_{org} flux to the sea floor (a) and accumulation rates (b) from experiment HANT

This is in agreement with common geological knowledge. Palaeoproductivity often is calculated from organic carbon accumulation in sediment cores. But -again referring to the remineralization rates- no overall valid equation should be used to calculate palaeoproductivities because absolute values may differ considerably.

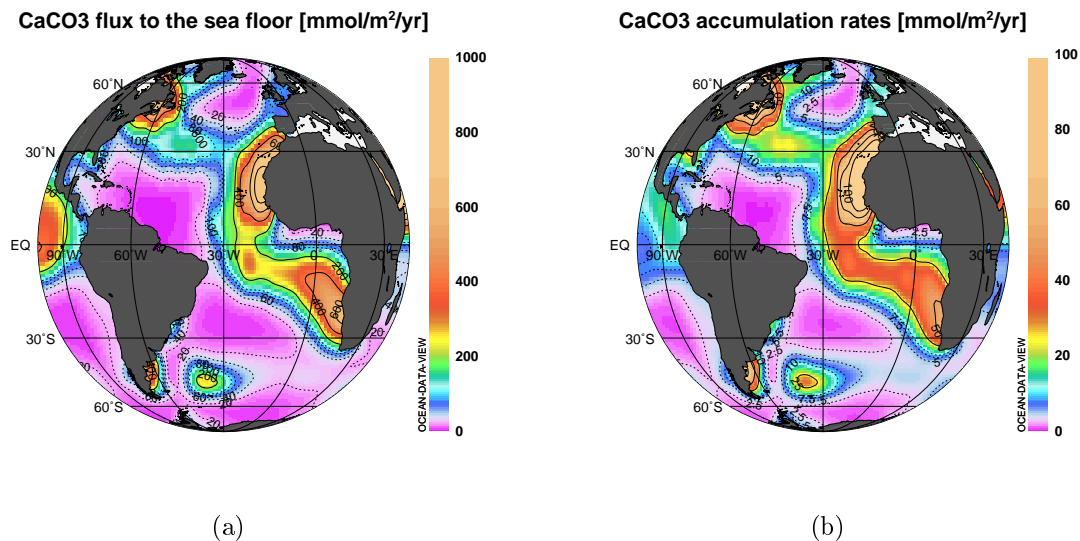


Figure 5.2: $CaCO_3$ flux to the sea floor (a) and accumulation rates (b) from experiment HANT

$CaCO_3$ fluxes to the bottom (Fig. 5.2(a)) are also high where $CaCO_3$ export pro-

duction is high (compare to Fig. 3.11 (a)). The relation between export production and deep fluxes seems to be more complicated compared to organic carbon. In a bow southern extending from north-west Africa towards south-west Africa, fluxes to the sea floor as well as sediment accumulation rates are highest. This is mainly due to the weak remineralization in water column (c.f. Fig. 3.11(b)) and so the pattern in $CaCO_3$ accumulation does not simply mimic high export fluxes. In general, $CaCO_3$ sediment accumulation preferably occurs at low latitudes in the eastern part of the Atlantic. This is in agreement with other models (see, e.g Archer (1996b), Lisitzin (1996)). Taking into account that $CaCO_3$ fluxes are only weakly constrained due to the sparse data base of alkalinity and ΣCO_2 , this is a surprising result. However, sediment accumulation rate distributions look very different from maps showing $CaCO_3$ content of sediments (e.g. Archer (1996a, 1996b), Lisitzin (1996)) and one should be very careful in comparing both kinds of information. This is particularly important for calcite because high $CaCO_3$ contents most often correlate with low flux rates (Lisitzin, 1996).

Even if the total $CaCO_3$ accumulation rates seem to be underestimated by the model (see above), the general patterns are acceptable.

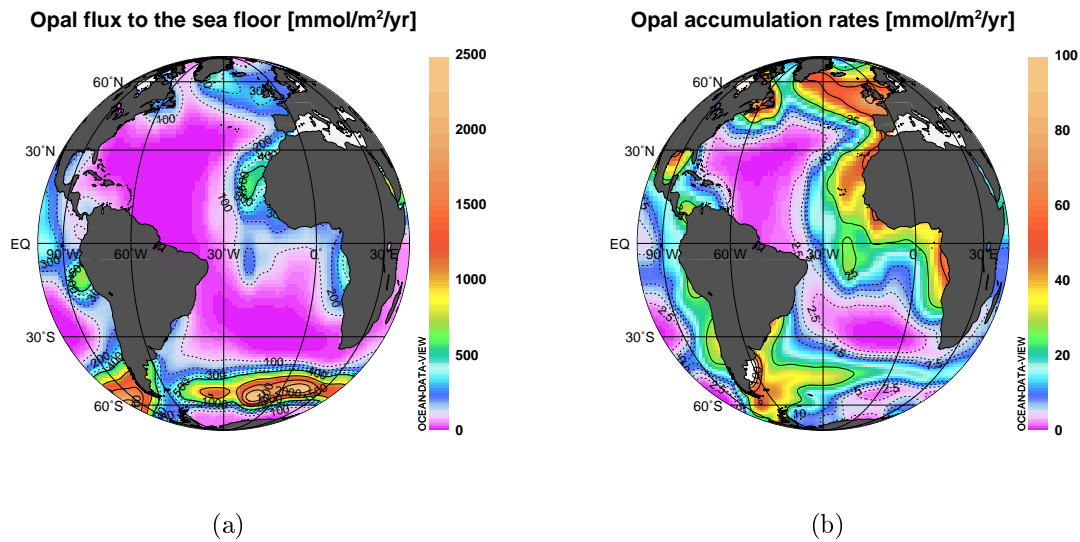


Figure 5.3: *Opal* flux to the sea floor (a) and accumulation rates (b) from experiment HANT

North of about $40^\circ S$ in the Atlantic, *Opal* fluxes to the sea floor and accumulation rates conserve the pattern of export production (c.f. Fig. 3.12). High fluxes (both, into the bottom box and into the sediment) are found along the eastern boundary of the Atlantic and at the Greenland-Scotland Ridge.

South of $40^\circ S$, flux patterns become much more complicated. It was already shown in Section 3.3 that in the area of the Antarctic Circumpolar Current (ACC) *Opal* flux properties drastically change. Comparing Figs. 3.12(a) and 5.3(a) reveals that the maximum flux to the sea floor is *not* below maximum export but shifted north-

wards. Whereas maximum export production occurs around $60^{\circ}S$, maximum flux to the sea floor is located around $50^{\circ}S$. This is due to the very strong change in remineralization rate β at ca. $55^{\circ}S$ (c.f. Fig.3.12(b)). The accumulation of *Opal* is also not located where maximum flux to the sea floor occurs but is again shifted northwards. Maximum accumulation is located between $40^{\circ}S$ and $50^{\circ}S$. The zonal pattern of *Opal* fluxes in the South Atlantic from export production to accumulation is shifted northwards about 15° of latitude. Such a decoupling is not found elsewhere and a closer view on the special silica system of this area is given in the next section.

6 A special case: *Opal* fluxes in the Weddell Sea

In Sections 3 and 5 it was already shown that the Southern Ocean exhibits strong gradients not only dynamically (the Polar Frontal System) but also with respect to silicate concentrations and *Opal* fluxes. The special environment of the Southern Ocean has attracted many scientists to investigate the biogeochemical system of that area and it has been stated (e.g. Ragueneau et al. (1997)) that the Southern Ocean is very important for global budgets of silica.

The Southern Ocean is a so-called high-nutrient-low-chlorophyll (HNLC) region. Surface nutrient concentrations are very high compared to the rest of the world ocean for all components namely phosphate, nitrate, and silicate (see, e.g. Fig. 1.1). But neither direct measurements nor satellite observations show high concentrations of chlorophyll. For a long time only minor photosynthetic activity was considered to be present. Many different hypotheses were examined to explain the low productivity of the Southern Ocean such as phytoplankton growth limitation due to iron limitation. However, the occurrence of deep (sub-surface) chlorophyll maxima led to a re-estimation of polar productivity giving the Southern Ocean a much larger importance for global budgets (see, e.g. Berger et al. (1987)). In the Antarctic, primary production is strongly coupled to *Opal* production because phytoplankton mainly consists of diatoms. *Opal* accumulation rates are widely used to reconstruct palaeo-environments in the Southern Ocean. For instance, the *Opal* belt is a zonal structure of high *Opal* content and is associated with the Polar Front (PF). The position of the *Opal* belt in sub-surface sediments is used to reconstruct palaeo hydrography. Preservation efficiencies of *Opal* were thought to be up to 100% of export fluxes and due to these high accumulation rates it was estimated that 75% of present day *Opal* accumulation occurs in the Southern Ocean (Nelson et al., 1991). Assuming that the *Opal* preservation is so high, *Opal* accumulation rates would be a very powerful proxy for the reconstruction of palaeoenvironments.

As could already be seen, strong meridional gradients are found in the Atlantic Ocean south of ca. $40^{\circ}S$ for general circulation, temperature, salinity, dissolved nutrients and also biogeochemical parameters.

The Antarctic Circumpolar Current (ACC) is the only closed circulation cell in the world ocean and transports more than 100 Sv in all oceans eastwards. The meridional extent of the ACC is from approx. $45^{\circ}S$ to $60^{\circ}S$. At least three fronts are identified within the ACC which separate the ACC into different sub-systems. Table 6.1 summarizes the definitions of the three fronts after Orsi et al. (1995).

SAF	$S < 34.20$ at $Z < 300m$, farther south $\Theta < 4 - 5^{\circ}C$ at $400m$, farther north $O_2 > 7ml/l$ at $Z < 200m$, farther south
PF	$\Theta < 2^{\circ}C$ at $Z < 200m$, farther south $\Theta - min$ (if present) at $Z > 200m$, farther south $\Theta < 2.2^{\circ}C$ at $Z > 800m$, farther north
southern	$\Theta > 1.8^{\circ}C$ at $Z > 500m$, farther north
ACC front	$\Theta < 0^{\circ}C$ at $Z < 150m$, farther south $S > 34.73$ at $Z > 800m$, farther south $O_2 < 4.2ml/l$ at $Z > 500m$, farther north

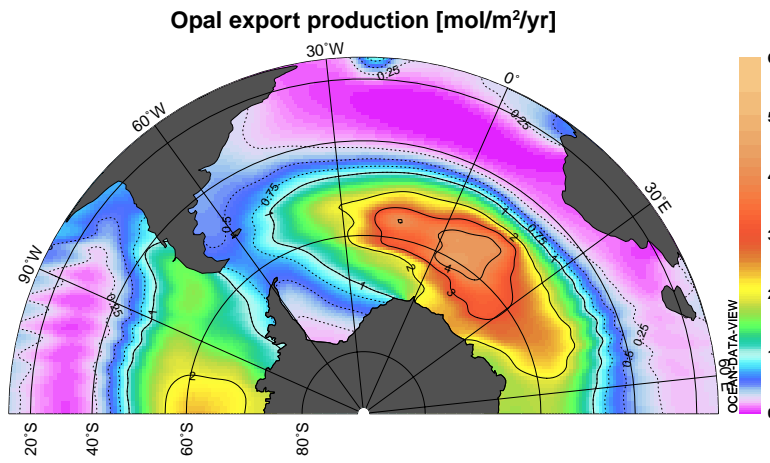
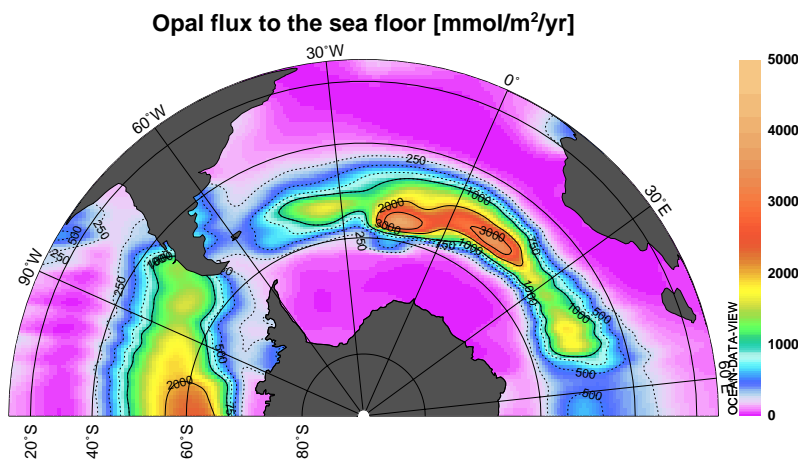
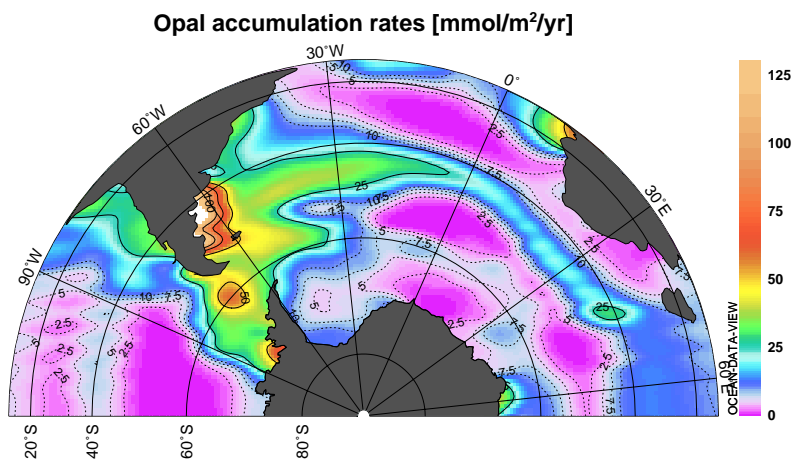
Table 6.1: Property indicators of the three ACC fronts from Orsi et al. (1995)

In the Atlantic, the Subantarctic Front (SAF) is located at approx. $50^{\circ}S$, the Polar Front (PF) between ca. $50^{\circ}S$ and $55^{\circ}S$. The southern ACC front is at ca. $60^{\circ}S$ at the Drake Passage and turns slowly northwards to approx. $55^{\circ}S$ south of Africa with a meander around the South Sandwich Islands. The changes in *Opal* fluxes from adjoint modelling are oriented perpendicular to this frontal system which can be seen in the Figs. 6.1 to 6.3 below.

Most intriguing in Figs. 6.1 to 6.3 is the strong zonal orientation of the general pattern. North of about $40^{\circ}S$, *Opal* fluxes are negligible at all depths (export, flux to the sea floor, and accumulation).

South of approx. $45^{\circ}S$, *Opal* export production (Fig. 6.1) increases drastically to a maximum of about $4.5mol/m^2/y$ around $60^{\circ}S$. *Opal* export fluxes are thus high everywhere south of $45^{\circ}S$ except in the south-western Weddell Sea. Here, productivity is limited due to a relatively stable sea ice cover during most of the year.

Fig. 6.2 shows the *Opal* flux to the seafloor. It can be clearly seen that the pattern of export production is not mirrored in the flux to the sea floor. The region of high fluxes is much narrower with maximum fluxes between $50^{\circ}S$ and $60^{\circ}S$. High fluxes to the sea floor are thus found in the entire region between the SAF and the southern boundary of the ACC, but fluxes are very low south of the ACC. This 'decoupling' is due to the rapid change in parameter β between $55^{\circ}S$ and $60^{\circ}S$ (c.f. Fig. 3.12). This transition occurs just south of the PF. Leyneart et al.(1993) also found that *Opal* fluxes in the Weddell Sea are quite different from elsewhere: "... Comparing our annual production estimate to previous estimates of vertical flux of opal in the Weddell Sea, we conclude that no more than 1% of the silica produced annually by phytoplankton in the upper water column reaches a depth of 800m. This is consistent with the general distribution of high accumulation rates of opal in the Southern Ocean sediments which evidence an unexplained gap in the Weddell Sea. Thus, regarding the cycling of biogenic silica in the Southern Ocean, the Weddell Sea appears to be atypical...".

Figure 6.1: *Opal* export productionFigure 6.2: *Opal* flux to the sea floorFigure 6.3: *Opal* accumulation rates

Van Bennekom et al. (1991) found that in the central Weddell Sea aluminium is less abundant than in other regions of the world ocean. Al/Si ratios in diatom shells were of an order of magnitude lower compared to diatoms from regions farther north. Biogenic *Opal* solubility was found to depend on aluminium content of the diatom shells. Bennekom et al.'s (1991) culture experiments showed that diatoms from the central Weddell Sea were incorporating aluminium when exposed to higher Al-concentrations and the solubility was decreased. The low aluminium concentrations south of the PF could thus explain the high remineralization rates of sinking *Opal* which is obviously reflected in the nutrient distributions because the adjoint model too produces very fast remineralization in this region. The aluminium hypothesis might even hold for an explanation of the reduced burial of biogenic *Opal* south of $50^{\circ}S$. Schlüter et al. (1998) calculated sediment accumulation rates and used pore water samples to estimate burial efficiencies in the Weddell Sea. They found that with the exception of the Scotia Sea and the eastern ACC only negligible amounts of primary produced biogenic *Opal* is preserved in the sediments. Table 6.2 summarizes their results.

Region	BSi Accu. <i>mmol/m²/y</i>	Total BSi-flux <i>mmol/m²/y</i>	PI _{tot} %
<i>W – Weddell Sea</i>			
Shelf	2.8 - 28.3	410.6 - 436.6	≈ 4
Slope	2.5 - 30	285.5 - 313.3	≈ 4
Deep-sea	0.17 - 1.3	95.2 - 97	≈ 0.2
<i>E – Weddell Sea</i>			
Maud Rise	1 - 12	346 - 357	≈ 1.5
Astrid Ridge	8 - 77	475 - 544	≈ 10
Scotia Sea	33 - 330	800 - 1097	≈ 21
E-ACC	367 - 380	967 - 980	≈ 24

Table 6.2: Sediment accumulation rates and flux to the sea floor from Schlüter et al. (1998). PI_{tot} denotes the relative accumulation rate, i.e. the ratio (BSi Accu.) / (Bsi-production).

The total preservation efficiency PI_{tot} in Tab. 6.2 gives the ratio of *Opal* accumulation to total primary produced *Opal*. Tab. 6.2 shows that preservation is low in most parts of the Weddell Sea. Only in the northern part of the study area, considerable amounts of *Opal* are buried in the sediments. Schlüter et al. (1998) conclude that biogenic *Opal* is of limited use for palaeo-reconstructions in the South Atlantic. Different dissolution kinetics due to trace metal content, different residence times in water column, and particle morphology might cause the decoupling of primary production of *Opal* and *Opal* accumulation.

The distributions of *Opal* export, flux to the sea floor, and accumulation from adjoint modelling also show this decoupling. The trends are the same as found by Schlüter et al. (1998). Absolute values of *Opal* accumulation rates in the ACC are lower (c.f. Fig.6.3) compared to Schlüter et al.'s (1998) values even for experiment

HANT (which gives probably overall too high *Opal* accumulation rates) but absolute values are difficult to compare. Sediment accumulation rates from adjoint modelling give mean accumulation over an area of about $2^\circ \times 2.5^\circ$ where mean values can be considerably different from point data. Even in deep sea areas, sediment accumulation rates can be highly variable spatially (Bennekoum et al. (1988), DeMaster (1981)) and focusing of sediments might add a bias towards higher accumulation rates in geological samples. Especially in areas with rough topography as near the Polar Front, one has to be very careful when budgets or mean accumulation rates are calculated. The selection of sampling sites most often depends on sediment type and expected sediment recovery and so sampling coverage is guaranteed to be non-randomly but biased towards high-accumulation sites (G. Kuhn, pers. comm.).

The mean, meso-scale accumulation rates from the adjoint model could be a more realistic estimate than 'upscaled' estimates from geological samples because nutrient distributions in water column integrate the signals from highly variable sea floor processes. The globally integrated *Opal* accumulation from the adjoint model is within the same range as estimates published by Tréguer et al. (1995) (c.f. Table 3.2) giving *Opal* accumulation rates from adjoint modelling higher confidence. The qualitative behaviour of *Opal* fluxes from inverse modelling in the Southern Ocean is summarized in Fig. 6.4

		North of the	At the	South of the	
		Polar Front			
Water column	{	Export production	<i>high</i>	<i>high</i>	<i>high</i>
	β	<i>low</i>	<i>intermediate</i>	<i>high</i>	
Sea floor	{	Flux to sea floor	<i>high</i>	<i>high</i>	<i>low</i>
	s	<i>high</i>	<i>low</i>	<i>low</i>	
	Accumulation	<i>high</i>	<i>low</i>	<i>low</i>	
Total	$\frac{\text{Accumulation}}{\text{Export production}}$	<i>high</i>	<i>low</i>	<i>low</i>	

Figure 6.4: *Opal* fluxes in the South Atlantic

The Southern Ocean is titled a high-nutrient-low-chlorophyll (HNLC) region which is reproduced by the model (c.f. C_{org} export in Fig.3.10). This statement is related to organic carbon only because chlorophyll is part of the soft organic tissue. The adjoint model gives very high *Opal* exports which are in agreement with independent studies of very high Si/C ratios in the Antarctic (Nelson et al., 1995). The Southern Ocean is thus a high productive region for biogenic *Opal*. On the other hand, *Opal* fluxes to the deep sea seem to be very low south of the southern boundary of the ACC. These results also agree with modern studies. Summarizing the results from adjoint modeling in the South Atlantic it can be stated that the Weddell Sea not only is a HNLC region for organic carbon but also a HPLF (high production, low flux) system for *Opal*. The decoupling of $Opal/C_{org}$ production and production/accumulation of

Opal might be linked by different yet unknown processes. It has been suggested that missing terrigenous components as *Fe*, *Al* are responsible for the special conditions in the Weddell Sea. The adjoint model could identify this special system from nutrient budget calculations.

7 Conclusions

The adjoint model has been found to be a very powerful tool to reproduce data of temperature and salinity and to give a current field which is in agreement with observations and other models. The overall circulation compares well with general oceanographic knowledge and all major current systems are reproduced. Data of dissolved nutrients and silicate could also be reproduced accurately by implementation of vertical fluxes of biogeneous particles. In the surface layer (0m to 133m), export of organic carbon, calcite, and opal was optimized to reproduce data of dissolved nutrients realistically. Simplifying one could say that excess (compared to data) of dissolved nutrients advected in the surface layer is transferred to particular matter which is then exported to the deep ocean.

Optimized export production of organic carbon closely resembles the pattern of observed primary production. *Opal* export production is similar in its spatial distribution as organic carbon north of ca. $40^{\circ}S$ and high *Opal* production also takes place in the Southern Ocean. So far, the results from adjoint modeling are in agreement with general ideas of the distribution of productivity in the world ocean and give independent estimates of annual rates of nutrient cycling in the surface layer. Global export of C_{org} is well in the range of independent estimates and *Opal* exports are within the same order of magnitude but higher than recent reestimates. The production of $CaCO_3$ is comparably weakly constrained from nutrient distributions because only relatively few alkalinity data are available for the global ocean and resulting exports seem to be underestimated by the model. To better constrain calcite formation it is necessary to include a priori knowledge and/or to assimilate more data of total carbon and total alkalinity.

Organic carbon flux vs. depth was parameterized with Suess-type functions $1/z^{\beta}$ (c.f. Section 2.7). These functions are widely used to reconstruct productivity from organic carbon content of deep sea sediments. With the adjoint model, the parameter β was varied spatially to give optimum nutrient distributions. The distribution of β shows systematic variations spatially. No overall valid value for β was found in the ocean. This is in agreement with recent studies and indicates that special care has to be taken when reconstructing paleoproductivities, because parameter β together with measured or estimated bottom fluxes determines the absolute values of reconstructed export fluxes. The distribution and variability of β should be investigated to better constrain paleo-estimates of organic carbon productivity. Because β from adjoint modeling shows systematic variations, these results could be used to better understand the interferences of β and oceanic conditions.

Remineralization of *Opal* and $CaCO_3$ was also parameterized using Suess-type functions. This parameterization was successfully applied to reproduce distributions of dissolved silicate, total carbon, and total alkalinity. Resulting *Opal* fluxes are reasonable in distribution and magnitude. This type of flux parameterization seems to be applicable to better understand *Opal* dissolution, which is further confirmed by the fact that the special conditions south of the Polar Front are reproduced by the model. $CaCO_3$ fluxes give (inspite of weak constraints) better preservation in the eastern Atlantic in agreement with geological knowledge.

A new feature of the model is the assimilation of direct flux measurements from sediment traps. A comparison of fluxes constrained with nutrient budgets only and sediment trap data showed that model fluxes were systematically higher than measurements. The model could be forced to reproduce sediment trap data more closely but systematic deviations remained. After the model was in a near-minimum state and relatively close to sediment trap data the assimilated sediment trap data were removed for an additional model experiment. The model fluxes very fast 'relaxed' giving higher particle fluxes again. A model solution which reproduces direct measurements *and* nutrients at the same time could not be obtained. Sediment trap data do conflict with budgets of dissolved nutrients showing systematic deviations. Model results indicate that sediment traps do not catch vertical particle fluxes quantitatively but trap efficiency seems to be low, especially at shallow water depths. This is in agreement with recent sediment trap studies which suggest that sediment trap data must be normalized (Buesseler et al., 1994). The results from adjoint modeling could be used to determine (together with other methods such as ^{230}Th normalization) trapping efficiencies.

Another new feature is the determination of sediment accumulation rates from nutrient budgets. At the sediment-water interface, a new model parameter '*s*' was introduced which regulates how much of the flux to the bottom box is removed from water column (burial efficiency). The parameter '*s*' was varied to obtain realistic concentrations of dissolved nutrients. It was found that integrated sediment accumulation rates for C_{org} are quite close to recent estimates of total C_{org} accumulation (Broecker and Peng, 1993) and the distribution of accumulation rates seems to be reasonable. In a first experiment, the initial value for burial efficiency of biogenic *Opal* was set to 25% and the model drastically reduced this burial efficiency almost everywhere in the ocean. This initial value thus appeared to be too high indicating that mean redissolution of sedimented *Opal* is more than 75% of the flux reaching the sea floor. The reduction of the start value to 4% gave much better agreement of model dissolved nutrients and data. Total *Opal* accumulation is lower than estimates by Tréguer et al.(1995) and Lisitzin (1996) but the pattern of high/low *Opal* accumulation in the Atlantic compares well with geological data. The absolute values at special locations deviate from pore water investigations and data from sediment cores but it is not yet clear whether this is due to an underestimation of model fluxes or due to an overestimation of geological data. The large-scale pattern of $CaCO_3$ accumulation is similar as proposed by Lisitzin (1996) with tendentially higher rates in the eastern Atlantic but absolute values were too low compared to literature values. This is probably due to a general underestimation of model $CaCO_3$ fluxes (see above).

Opal fluxes from the adjoint model show very special conditions in the Southern Ocean. A more detailed comparison of model *Opal* fluxes and recent studies shows that the principal findings are similar. The Weddell Sea south of the southern front of the Antarctic Circumpolar Current appears as a high-productive region with astonishingly low deep sea particle fluxes. This high-production low-flux (HPLF) anomaly is also found in direct measurements (Leynaert et al., 1991). The fact that

the same region was 'atypical' in the model parameter distributions indicates that the information about water column processes stored in distributions of dissolved nutrients indeed can be extracted with the adjoint method.

Ocean circulation and biogeochemical processes are strongly coupled and the dependencies allow to calculate process rates from properties in the water column: Primary production only can persist where nutrients are supplied to the sea surface. The modeling of new production (or export production) must include advective processes because standing stocks of phytoplankton or nutrient depletion alone do not provide information about nutrient *fluxes*. Deep sea particle fluxes probably depend on sinking velocity, particle morphology, physical properties of the surrounding waters, and more. The *combination* of all individual processes is reflected in distributions of dissolved nutrients. The adjoint model used in this study is a very powerful tool to calculate physical circulation and biogeochemical processes *simultaneously* and to detect areas of interest with respect to gradients of physical and biogeochemical process rates. The underlying processes cannot be explained by the model because resulting information are mean transports and mean cycling. These mean rates can be used to test whether point data are representative for larger areas and to normalize the integrated effects of small-scale processes.

The results of the experiments presented in this work are promising: Optimized independent model parameters show systematic variations which are mostly in agreement with general oceanographic and geological/biological knowledge such as the current field and the large-scale patterns of export production. On the other hand, processes which are poorly understood are to be seen in their effect on nutrient distributions. Systematic variations of model parameters and their relation to the oceanographic environment can give indicators about the processes involved.

The application of inverse modeling with higher resolution in areas of interest requires the assimilation of more data and/or independent tracers. An interesting future application of the adjoint model is the investigation of the drastic changes of physical and biogeochemical processes near the Polar Front in the South Atlantic and in the Weddell Sea.

A River input

The total removal of nutrients due to accumulation of surface sediments is compensated by river input of dissolved nutrients.

River water properties are usually given in units of $\frac{mg}{l}$. To calculate the contribution of a particular river one has to know the annual discharge of water. Estimates of river discharge bear relatively high errors so the absolute values are not to be taken too seriously but give an estimate. Further, the constituents of river water vary with season (depending on geography) and so the nutrient content of most rivers also covers a comparably wide range (e.g. Milliman (1980), Dyer (1980)).

River	Mass flux †		SiO_2 ‡	SiO_2^*	SiO_2^*
	$[\frac{m^3}{s}]$	%	$[\frac{mg}{l}]$	$[\frac{mg}{l} * \frac{m^3}{s}]$	%
Amazon	175000	42.113	11.1	1942500	49.167
Congo	39640	9.539	10.4	412256	10.435
Orinoco	33950	8.170	11.5	390425	9.882
Yangtse Kiang	22000	5.294	6.9	151800	3.842
Brahmaputra	19200	4.620	7.8	149760	3.791
Mississippi	17800	4.284	7.6	135280	3.424
Yenissei	17800	4.284	3.8	67640	1.712
Lena	16300	3.923	2.9	47270	1.196
Parana	14900	3.586	14.3	213070	5.393
Mekong	14900	3.586	8.9	132610	3.356
St.Lawrence	14160	3.408	2.4	33984	0.860
Ob	12200	2.936	4.2	51240	1.297
Ganges	11600	2.791	8.2	95120	2.408
Niger	6090	1.466	21	127890	3.237

Table A.1: Fresh water and SiO_2 inputs through major world rivers, †: (Lerman, 1980b), ‡: (Berner and Berner, 1996), *: calculated from water discharge (†) and silicate concentration (‡)

Table A.1 gives the mean annual fresh water discharge from Lerman (1980) and calculated inputs of dissolved silica (using Si concentrations from Berner and Berner (1996)) for the 14 largest rivers of the world. It is possible to take more rivers into account but all other world rivers have discharges smaller than the Niger river which is already almost negligible compared to the other rivers. The 10 biggest rivers account for 73% of global river water discharge (Lerman, 1980b). There is considerable variation in concentration of dissolved silica ranging from $2.4\frac{mg}{l}$ (St. Lawrence) to $21\frac{mg}{l}$ (Niger). Variations in dissolved inorganic carbon and organic carbon are generally smaller but within the same range (not shown, see, for instance Bennekou and Salomons (1980), Meybeck (1980), Degens and Kempe (1991), Ludwig (1996)). Comparing the percentage of water input and percentage of silica input shows that about 60% of water *and also* 70% of dissolved silica is contributed by three rivers,

namely Amazon, Congo, and Orinoco. All other rivers contribute with less than 6% to the global budget only.

The general dominance of three rivers is thus not changed by regarding the silica content of river water. Changes in the ranking by regarding carbon content were even smaller. In the model calculations, the sum of nutrients removed at the sea floor due to sediment accumulation is distributed according to the water discharge of these 14 rivers neglecting slight changes in relative nutrient content. The discharge of nutrients is realized by setting a source in the top box of a column near a river mouth. The boxes accounting for riverine input are the *only* boxes in the model where a nutrient source at the surface exists. The nutrient budget is balanced by riverine input through these 14 rivers, no aeolian nutrient input is modeled.

If $n_{r,i}$ denotes the top box 'at a river mouth', then the source term in this box becomes (Eq. 2.59):

$$q(n_{r,i})_{N,P,C,O,Si} = r_i \sum_{columns} J(\mathcal{S})_{N,P,C,O,Si}$$

Here, the coefficient r_i is taken from the third column in Table A.1 and gives the relative portion a river contributes to the total input of dissolved nutrients.

B Derivatives of costfunction $F(p^*, \tilde{p})$

For the calculation of the the gradient of $F(p^*, \tilde{p})$, all partial derivatives must be known. In addition to advection/diffusion terms, all source and sink terms contribute to model-data misfit. Partial derivatives for export ($\propto \alpha$), remineralization (β) and accumulation (s) resolve similar for all components ($C_{org}, CaCO_3, Opal$). For shortness, only equations for organic carbon are shown. The difference to $CaCO_3$ and $Opal$ is a factor in export production only (c.f. definition of particle fluxes in Section 2.7). The partial derivatives are then scaled with the Redfield ratios in order to penalize deviations of dependent model parameters to data.

All biogeochemical parameters are bound to non-negative values. Therefore, for each model column (j) the parameters are internally represented:

$$\gamma =: p_{1,j}^2 \quad \beta =: p_{2,j}^2 \quad \mathcal{S} =: p_{3,j}^2 \quad (\text{B.1})$$

The sources (for each box) contribute to the gradient with terms proportional to:

$$\frac{\partial}{\partial p_{i,j}} Q \quad (\text{B.2})$$

B.1 Euphotic zone

In the two uppermost boxes, only parameter $p_{1,j}^2$ ($= \gamma$) is involved. The source term is

$$Q = p_{1,j}^2 \frac{PP^2}{410}$$

and the derivatives become:

$$\frac{\partial}{\partial p_{1,j}} Q = 2p \frac{PP^2}{410} \quad (\text{B.3})$$

$$\frac{\partial}{\partial p_{2,j}} Q = 0 \quad (\text{B.4})$$

$$\frac{\partial}{\partial p_{3,j}} Q = 0 \quad (\text{B.5})$$

B.2 Water column

Within the water column, sources depend on export ($\propto p_{1,j}^2$) and $\beta (= p_{2,j}^2)$:

$$Q = - \underbrace{\gamma \frac{PP^2}{410}}_{=\alpha} z_{EP}^\beta \left[z_i^{-\beta} - z_{i+1}^{-\beta} \right]$$

Partial derivatives become:

$$\frac{\partial}{\partial p_{1,j}} Q = 2p_{1,j} \frac{PP^2}{410} z_{EP}^\beta \left[z_i^{-\beta} - z_{i+1}^{-\beta} \right] \quad (\text{B.6})$$

$$\frac{\partial}{\partial p_{2,j}} Q = 2p_{2,j} \alpha \left[2p_{2,j} \left[\ln \left(\frac{z_{EP}}{z_i} \right) z_i^{-\beta} - \ln \left(\frac{z_{EP}}{z_{i+1}} \right) z_{i+1}^{-\beta} \right] \right] \quad (\text{B.7})$$

$$\frac{\partial}{\partial p_{3,j}} Q = 0 \quad (\text{B.8})$$

B.3 Sediment-water interface

At the sediment-water interface, all parameters contribute to the source term:

$$Q_b = (1 - s) \alpha z_b^{-\beta}$$

All partial derivatives remain non-zero:

$$\frac{\partial}{\partial p_{1,j}} Q = (1 - s) \left[2p_{1,j} \frac{PP^2}{410} z_b^{-\beta} \right] \quad (\text{B.9})$$

$$\frac{\partial}{\partial p_{2,j}} Q = (1 - s) \left[\alpha z_b^{-\beta} \right] \left[2p_{2,j} \ln \left(\frac{z_{EP}}{z_b} \right) \right] \quad (\text{B.10})$$

$$\frac{\partial}{\partial p_{3,j}} Q = -2p_{3,j} \alpha z_b^{-\beta} \quad (\text{B.11})$$

B.4 Riverine input

The riverine input depends on the integrated flux to the sediment and thus, *all* fluxes $J(\mathcal{S})_j$ contribute to the source:

$$Q_{r_i} = r_i \sum_{\text{columns}} J(\mathcal{S})_j \alpha z_b^{-\beta}$$

A single box (where the riverine input applies) affects *all* parameters at columns where sedimentation occurs.

$$\frac{\partial}{\partial p_{1,j}} Q = p_{3,j} \left[2p_{1,j} \frac{PP^2}{410} z_b^{-\beta} \right] \quad (\text{B.12})$$

$$\frac{\partial}{\partial p_{2,j}} Q = p_{3,j} \left[\alpha z_b^{-\beta} \right] \left[2p_{2,j} \ln \left(\frac{z_{EP}}{z_b} \right) \right] \quad (\text{B.13})$$

$$\frac{\partial}{\partial p_{3,j}} Q = 2p_{3,j} \left[\alpha z_b^{-\beta} \right] \quad (\text{B.14})$$

B.5 Deviations from sediment trap data

The term in costfunction $F(p^*, \tilde{p})$ for penalizing deviations from trap data has the form:

$$[J(z)_{Model} - J(z)_{Daten}]^2 \quad (\text{B.15})$$

All sediment traps are located deeper than the euphotic zone (where model particle fluxes are defined). Further, trap data were 'mapped' to a horizontal boundary of a box (c.f. Appendix C). Therefore, the partial derivatives in combination of Equations (B.15) and (B.6) to (B.8) become:

$$\begin{aligned} \frac{\partial}{\partial p_{1,j}} Q = & 2 [J(z)_{Model} - J(z)_{Daten}] \\ & \cdot 2p_{1,j} \frac{PP^2}{410} z_{EP}^\beta [z_i^{-\beta} - z_{i+1}^{-\beta}] \end{aligned} \quad (\text{B.16})$$

$$\begin{aligned} \frac{\partial}{\partial p_{2,j}} Q = & 2 [J(z)_{Model} - J(z)_{Daten}] \\ & \cdot 2p_{2,j} \alpha \quad 2p_{2,j} \left[\ln \left(\frac{z_{EP}}{z_i} \right) z_i^{-\beta} - \ln \left(\frac{z_{EP}}{z_{i+1}} \right) z_{i+1}^{-\beta} \right] \end{aligned} \quad (\text{B.17})$$

$$\frac{\partial}{\partial p_{3,j}} Q = 0 \quad (\text{B.18})$$

C New variables and routines

Deviations of model fluxes to sediment trap data are included as soft constraints. As pointed out in section 2.8, care has to be taken not to overestimate the quality of data by setting small weight factors. To include sediment trap data in the model it is not sufficient to calculate source and sink terms of dissolved nutrients (c.f. section 2.7). Calculating deviations from sediment trap data:

$$[J(z)_{model} - J(z)_{data}]^2 \quad (\text{C.1})$$

for costfunction $F(p^*, \tilde{p})$ requires explicit model fluxes $J(z)_{Model}$. New dependent parameters representing model particle fluxes are defined (modeled properties \tilde{p} , c.f. (2.22) in section 2.5). Particle fluxes are calculated at the upper surface of each model box.

Trap depth generally lies between two levels (n and $n + 1$). Annual averaged sediment trap fluxes $J(z)_{Data}$ from table 4.1 are set at the next-most level (i.e. at level n if $z(trap) < z(n) + \frac{z(n+1)-z(n)}{2}$ and at level $n + 1$ else).

Sediment accumulation rates are realized with independent parameters s for C_{org} , $CaCO_3$, and $Opal$, respectively. These parameters determine how much of the flux reaching the sea floor is accumulated.

$$J(\mathcal{S}) = s \cdot J(z_{Bottom}) \quad (\text{C.2})$$

The formal implementation was already discussed in section 2.7.

Sediment accumulation rates thus become new dependent parameters. Model-data deviations can be penalized but up to now, no accumulation data are included (see Section 5).

Generally, it is possible to use sediment accumulation rates as soft constraints as for the sediment trap data. In the model, sediment accumulation rates can be penalized with terms:

$$[J(\mathcal{S})_{model} - J(z)_{data}]^2 \quad (\text{C.3})$$

To force sediment accumulation rates (relative to flux to bottom) to certain values one could also apply smoothness constraints and/or a priori value constraints in costfunction F . In the experiments discussed in the presented these terms were not used.

The calculation of new independent and dependent parameters requires new variables and routines.

C.1 New variables

C.1.1 moddat.h

The common block in `moddat.h` was expanded with variables for sediment trap data and sediment accumulation rate data. Sediment trap data can be set for each box and accumulation rate data for each column.

```
common /moddat/datte(mxclus,2),datsa(mxclus,2),
datox(mxclus,2),datpo(mxclus,2),
datni(mxclus,2),datsi(mxclus,2),
dattc(mxclus,2),datal(mxclus,2),
datc3(mxclus,2),datc4(mxclus,2),
datsw(mxcol,2), datsh(mxcol,2),
datts(mxdts,2), datkh(2),datkv(2),
datcofl(mxclus,2),datcafl(mxclus,2),
datsifl(mxclus,2), datcoac(mxcol,2),
datcaac(mxcol,2),datsiac(mxcol,2)
```

<code>datcofl(i,1)</code>	Sediment trap data C_{org} [$\frac{mol}{m^2y}$]
<code>datcofl(i,2)</code>	Error of <code>datcofl(i,1)</code>
<code>datcafl(i,1)</code>	Sediment trap data $CaCO_3$ [$\frac{mol}{m^2y}$]
<code>datcafl(i,2)</code>	Error of <code>datcafl(i,1)</code>
<code>datsifl(i,1)</code>	Sediment trap data <i>Opal</i> [$\frac{mol}{m^2y}$]
<code>datsifl(i,2)</code>	Error of <code>datsifl(i,1)</code>
<code>datcoac(i,1)</code>	Accumulation rate C_{org} [$\frac{mol}{m^2y}$]
<code>datcoac(i,2)</code>	Error of <code>datcoac(i,1)</code>
<code>datcaac(i,1)</code>	Accumulation rate $CaCO_3$ [$\frac{mol}{m^2y}$]
<code>datcaac(i,2)</code>	Error of <code>datcaac(i,1)</code>
<code>datsiac(i,1)</code>	Accumulation rate <i>Opal</i> [$\frac{mol}{m^2y}$]
<code>datsiac(i,2)</code>	Error of <code>datsiac(i,1)</code>

Table C.1: Meaning and units of new variables in `moddat.h`

C.1.2 parflux.prm

The file `parflux.prm` contains information for different modes of the model (for instance, how many iterations are to be performed). Here, a new parameter `indsed` is set (0 = false, 1 = true) defining whether sediment accumulation rates are to be calculated.

C.1.3 `sediments.h`

The new common-block `sediments.h` contains variables related to sediment accumulation rates.

```
c sedimente
```

```
common /sediments/posedi(0:mxcol),casedi(0:mxcol),sisedi(0:mxcol),
dpAorg(0:mxcol),dpBorg(0:mxcol),dpCorg(0:mxcol),
dpAsil(0:mxcol),dpBsil(0:mxcol),dpCsil(0:mxcol),
dpAcar(0:mxcol),dpBcar(0:mxcol),dpCcar(0:mxcol),
rivers(0:mxriver,0:4), idcols(0:mxcol)
```

<code>posedi(0:mxcol)</code>	Relative accumulation rate C_{org}
<code>casedi(0:mxcol)</code>	Relative accumulation rate $CaCO_3$
<code>sisedi(0:mxcol)</code>	Relative accumulation rate $Opal$
<code>dpAorg(0:mxcol)</code>	$\partial q_{C_{org}} / \partial p_1$
<code>dpBorg(0:mxcol)</code>	$\partial q_{C_{org}} / \partial p_2$
<code>dpAcar(0:mxcol)</code>	$\partial q_{CaCO_3} / \partial p_3$
<code>dpBcar(0:mxcol)</code>	$\partial q_{CaCO_3} / \partial p_4$
<code>dpAsil(0:mxcol)</code>	$\partial q_{Opal} / \partial p_5$
<code>dpBsil(0:mxcol)</code>	$\partial q_{Opal} / \partial p_6$
<code>rivers(0:mxriver,1:4)</code>	1: column number 2: percentage C_{org} 3: percentage $CaCO_3$ 4: percentage $Opal$
<code>idcols(0:mxcol)</code>	0: inactive 1: no river input, $nlvl > 2$ -1: river input, $nlvl = 1$ -2: river input, $nlvl = 2$ -3: river input, $nlvl > 2$ 2: sediment trap data assimilated 3: accumulation rates assimilated

Table C.2: Meaning of new variables in common block `sediments.h`

`idcols` indicates how the columns are to be treated in the model calculations. Biogeochemical particle fluxes are calculated in columns with at least 3 levels ($nlvl \geq 2$). Currently, no vertical particle fluxes are calculated in columns with river input ($idcols < 0$) and all nutrients are distributed with the same percentage (c.f. Appendix A).

C.1.4 `depprm.h`

Common block `depprm.h` contains variables of the dependent model parameters (the modeled properties). Since vertical particle fluxes and sediment accumulation rates

are now determined explicitly, `depprm.h` was expanded.

```
common /depprm/wfl(mxbox),
xtm(-mxbbox:mxclus), xsm(-mxbbox:mxclus),
xoxm(-mxbbox:mxclus), xpom(-mxbbox:mxclus),
xnim(-mxbbox:mxclus), xsim(-mxbbox:mxclus),
xtcm(-mxbbox:mxclus), xalm(-mxbbox:mxclus),
xc3m(-mxbbox:mxclus), xc4m(-mxbbox:mxclus),
xcoflm(-mxbbox:mxclus), xcaflm(-mxbbox:mxclus),
xsiflm(-mxbbox:mxclus), xcoacc(0:mxcol),
xcaacc(0:mxcol), xsiacc(0:mxcol)
```

<code>xcoflm(-mxbbox:mxclus)</code>	Particle flux C_{org} [$\frac{mol}{m^2y}$]
<code>xcaflm(-mxbbox:mxclus)</code>	Particle flux $CaCO_3$ [$\frac{mol}{m^2y}$]
<code>xsiflm(-mxbbox:mxclus)</code>	Particle flux $Opal$ [$\frac{mol}{m^2y}$]
<code>xcoacc(0:mxcol)</code>	Accumulation rate C_{org} [$\frac{mol}{m^2y}$]
<code>xcaacc(0:mxcol)</code>	Accumulation rate $CaCO_3$ [$\frac{mol}{m^2y}$]
<code>xsiacc(0:mxcol)</code>	Accumulation rate $Opal$ [$\frac{mol}{m^2y}$]

Table C.3: Meaning and units of new variables in `depprm.h`

C.2 New routines

C.2.1 `lfluxdat(finam,dat,edatmi,ident)`

Subroutine to read sediment trap data from file.

```
finam  filename
dat     sediment trap data in units [ $mol/m^2/y$ ]
edatmi minimum error of sediment trap data in units [ $mol/m^2/y$ ]
ident  indicator for sediment trap data (idcols(column) set to 2)
```

C.2.2 `laccudat(finam,dat,edatmi,ident)`

Subroutine to read sediment accumulation rates from file, analog to C.2.1 but `idcols(column)` is set to 3.

C.2.3 `setrivers`

If sediment accumulation rates are calculated, river input is set to balance total removal of nutrients. File *rivers* is read which must contain the number of rivers, column number of each river and relative contribution of organic carbon, calcite,

and opal. For each column where river input is set, `idcols(column)` is set to values as indicated in Table C.2

C.2.4 `calbiofl(p,np)`

Subroutine to calculate vertical fluxes of biogeneous particles. In this routine, `xcoflm`, `xcaflm`, `xsiflm` representing the flux through the top surface of each box are calculated. For each column, the sediment accumulation rates `xcoacc`, `xcaacc`, `xsiaacc` are determined.

`p` parameter (vector, `dim(np)`)
`objgrd` number of parameters (scalar)

C.2.5 `ofdbioflux(p,objgrd,np,objf,tobjf,tffak,ifobjf)`

Subroutine to penalize deviations of model fluxes to sediment trap data. For each box where sediment trap data exist, deviations of model fluxes are accumulated in `tobjf` and `objf`. Partial derivatives are added to gradient `objgrd`.

`p` parameter (vector, `dim(np)`)
`objgrd` gradient of F (vector, `dim(np)`)
`np` number of parameters (scalar)
`objf` total costfunction F
`tobjf` terms in costfunction F (vector, `dim(number of terms)`)
`tffak` weights of terms in F (vector, `dim(number of terms)`)
`ifobjf` number of weight (scalar)

C.2.6 `ofdacc(p,objgrd,np,objf,tobjf,tffak,ifobjf)`

Subroutine to penalize deviations of model accumulation rates from accumulation rate data, mostly analogous to C.2.5 but deviations are calculated column-wise.

`p` parameter (vector, `dim(np)`)
`objgrd` gradient of F (vector, `dim(np)`)
`np` number of parameters (scalar)
`objf` total costfunction F
`tobjf` terms in costfunction F (vector, `dim(number of terms)`)
`tffak` weights of terms in F (vector, `dim(number of terms)`)
`ifobjf` number of weight (scalar)

C.2.7 ofsmip(p,objgrd,np,objf,tobjf,tffak,ifobjf)

Routine to calculate the smoothness terms in costfunction F . This routine is not new but refined. Parameters contributing with their square values to the model are squared before penalizing the second derivative (c.f. Section 2.8.1). By doing so, the functional form of the penalty term is symmetric again. Otherwise, neighboring parameter values of, for instance, -2 and 2 would be penalized despite having the same effect in the model calculations. The parameters contributing with their square values only are export production, remineralization, and sediment accumulation.

p parameter (vector, dim(np))
objgrd gradient of F (vector, dim(np))
np number of parameters (scalar)
objf total costfunction F
tobjf terms in costfunction F (vector dim(number, of terms))
tffak weights of terms in F (vector dim(number, of terms))
ifobjf number of weight (scalar)

C.2.8 ofapbg(p,objgrd,np,objf,tobjf,tffak,ifobjf)

Subroutine to penalize deviations of independent biogeochemical parameters from a priori values. This routine is not new but refined. Parameters contributing with their square values to the model are squared before penalizing deviations to a priori values. The parameters contributing with their square values only are export production, remineralization, and sediment accumulation (see also C.2.7).

p parameter (vector, dim(np))
objgrd gradient of F (vector, dim(np))
np number of parameters (scalar)
objf total costfunction F
tobjf terms in costfunction F (vector, dim(number of terms))
tffak weights of terms in F (vector, dim(number of terms))
ifobjf number of weight (scalar)

D Abbreviations and units

\mathcal{A}	Advection/diffusion matrix
$A_{i,k,j}$	Surfaces of model boxes
AABW	Antarctic Bottom Water
AAIW	Antarctic Intermediate Water
Acc	Accumulation rate
ACC	Antarctic Circumpolar Current
AOU	Apparent Oxygen Utilization
BATS	Bermuda Atlantic Time Series
c, c^*	Concentrations at box center and box surface, respectively
^{14}C	Radiocarbon
CaCO_3	Calcium carbonate
CCSR	Center for Climate System Research
CFC	Chlorofluorocarbon
CO_2	Carbon-dioxide
C_{org}	Organic carbon
DOM	Dissolved Organic Matter
DOP	Dissolved Organic Phosphorus
E	Hard constraint
EP	Export Production
F	Costfunction
f-ratio	EP/PP
G	Giga = 10^9
GEOSECS	Geochemical Ocean Sections Study
GFDL	Geophysics Fluid Dynamics Laboratory
HAMOCC	Hamburg Ocean Carbon Cycle Circulation Model
HNLC	High Nutrient Low Chlorophyll
HPLF	High Production Low Flux
JGOFS	Joint Global Ocean Flux Study
$J(z)$	Particle flux
K_h, K_v	Horizontal and vertical mixing coefficients
L	Lagrange function
LSG	Large Scale Geostrophic
m	Milli = 10^{-3} or meter
mol	$1mol = 6.022 \times 10^{23}$
NABE	North Atlantic Bloom Experiment
NADW	North Atlantic Deep Water
NG	Not given

NO_3	Nitrate
O_2	Oxygen
ODV	Ocean Data View
<i>Opal</i>	Amorphous biogenic silica
p^*	Independent model parameters
\tilde{p}	Dependent model parameters
PF	Polar Front
PFZ	Polar Frontal Zone
PO_4	Phosphate
POM	Particulate Organic Matter
PP	Primary Production
Q	Heat flux
s	Parameter for burial efficiency of surface sediments
SAF	Southern ACC Front
Si	Silicate
Sv	Sverdrups, $1Sv = 10^6 m^3/s$
T	Tera = 10^{12}
<i>TALK</i>	Total Alkalinity
$\vec{u}, \vec{v}, \vec{w}$	zonal, meridional, and vertical velocities
z	Water depth
<hr/>	
α	Parameter for export production of particulate matter
β	Parameter for remineralization scale length
λ	Lagrange multiplier

Acknowledgments

First of all, I would like to thank my supervisor Reiner Schlitzer. Without his constant support, his enthusiasm for interdisciplinary science and his confidence in my capability to take part in (t)his research, it would have been impossible to complete this work. He also provided the model and additional software for gridding and visualization of model results. I also would like to thank him for providing the first expert opinion on this work.

Thanks are also due to Prof. W. Roether for his lively interest in this work and for providing the second expert opinion.

I would also like to thank Prof. D. Fütterer who made the resources of the Alfred Wegener Institute (AWI) available to me and who supports the interdisciplinary work of the small 'modeling subgroup' in the geology department.

Dr. Gerhard Fischer is thanked for providing a huge amount of sediment trap data and helping me with the evaluation and the selection of particle fluxes to be included in the model.

Thanks are due to all people who contributed bits and pieces to increase my mathematical/geological/physical/biological/chemical understanding and who were open to discussions and who I cannot all name here.

Special thanks go to W. Geibert with whom I had -sometimes endlessly- discussions about opal, thorium, the Weddell Sea and their causal connection to quantum mechanics and the universe. He also was a very constructive reviewer of early versions of this manuscript.

Special thanks also to C.-D. Hillenbrand who was persistently teaching me 'geological background knowledge' and who never got's out of patience when I was asking 'questions of a physicist knowing nothing of geology' and who also debugged this manuscript with respect to 'geological faux-pas'.

This manuscript also benefited from constructive reviews by Marie-France Weirig, Beate Müller, and Gabriele Uenzelmann-Neben.

Last but not least I would like to thank my friends and colleagues at the AWI who provided a creative, friendly, and sometimes very hilariously working atmosphere.

This work was funded by the Deutsche Forschungsgemeinschaft (SFB 261 at AWI)

References

- Abbot, M. and Barksdale, B. (1995). Variability in Upwelling Systems as Observed by Satellite Remote Sensing. In Summerhayes, C., Emeis, K.-C., Angel, M., Smith, R., and Zeitzschel, B., editors, *Upwelling in the Ocean*, pages 221–238. Wiley & Sons, Chichester, New York, Brisbane, Toronto, Singapore.
- Anderson, L. and Sarmiento, J. (1995). Global ocean phosphate and oxygen simulations. *Global Biogeochemical Cycles*, 9:621–636.
- Antoine, D., André, J.-M., and Morel, A. (1996). Oceanic primary production 2. Estimation at global scale (coastal zone color scanner) chlorophyll. *Global Biogeochemical Cycles*, 10:57–69.
- Antoine, D. and Morel, A. (1996). Oceanic primary production 1. Adaption of a spectral light-photosynthesis model in view of application to satellite chlorophyll observations. *Global Biogeochemical Cycles*, 10:43–55.
- Archer, D. E. (1996a). An atlas of the distribution of calcium carbonate in sediments of the deepsea. *Glob. Biogeochem. Cycles*, 10:159–174.
- Archer, D. E. (1996b). A data-driven model of the global calcite lysocline. *Glob. Biogeochem. Cycles*, 10:511–526.
- Bacastow, R. and Maier-Reimer, E. (1990). Ocean-circulation model of the carbon cycle. *Climate Dynamics*, 4:95–125.
- Bacon, M. P., Huh, C. A., Fler, A. P., and Deuser, W. G. (1985). Seasonality in the flux of natural radionuclides and plutonium in the deep sargasso sea. *Deep Sea Research*, 32:273–286.
- Bainbridge, A. E. (1980). GEOSECS atlantic expedition, vol. ii, sections and profiles 1972–1973. Technical report, Washington D. C.
- Baker, E. T., Milburn, H., and Tennant, D. (1988). Field assessment of sediment trap efficiency under varying flow conditions. *Journal of Marine Research*, 46(3):573–592.
- BATS (1998). Bermuda Atlantic Time Series. Internet <http://www.bbsr.edu/bats/bats.html>.
- Berger, W. (1989). Appendix Global Maps of Ocean Productivity. In Berger, W., Smetacek, V., and Wefer, G., editors, *Productivity of the Ocean: Present and Past*, number 44 in Dahlem Workshop Reports, pages 429–455. Wiley & Sons, Chichester, New York, Brisbane, Toronto, Singapore.
- Berger, W., Fischer, K., Lai, C., and Wu, G. (1987). Ocean productivity and organic carbon flux. Part I. Overview and maps of primary production and export production. Technical Report Reference Series 87-30, SIO, Scripps Institution of Oceanography, University of California.

- Berger, W., Smetacek, V., and Wefer, G. (1989). Ocean Productivity and Paleoproductivity – An Overview. In Berger, W., Smetacek, V., and Wefer, G., editors, *Productivity of the Ocean: Present and Past*, number 44 in Dahlem Workshop Reports, pages 1–34. Wiley & Sons, Chichester, New York, Brisbane, Toronto, Singapore.
- Berger, W. and Wefer, G. (1990). Export production: seasonality and intermittency, and paleoceanographic implications. *Paleogeography, Paleoclimatology, Paleoecology*, 89:245–254.
- Berner, E. and Berner, R. (1996). *Global Environment: Water, Air, and Geochemical Cycles*. Prentice Hall, New Jersey.
- Bishop, J. (1989). Regional Extremes in Particulate Matter Composition and Flux: Effects on the Chemistry of the Ocean Interior. In Berger, W., Smetacek, V., and Wefer, G., editors, *Productivity of the Ocean: Present and Past*, number 44 in Dahlem Workshop Reports, pages 117–137. Wiley & Sons, Chichester, New York, Brisbane, Toronto, Singapore.
- Broecker, W. and Peng, T.-H. (1993). Greenhouse puzzles. Technical report, Lamont-Doherty Earth Observatory of Columbia, Palisades, NY 10964.
- Broecker, W. S., Gerard, R., Ewing, M., and Heezen, B. C. (1960). Natural radiocarbon in the Atlantic Ocean. *J. Geophys. Res.*, 65:2903–2931.
- Buesseler, K. O. (1991). Do upper-ocean sediment traps provide an accurate record of particle flux? *Nature*, 353:420–423.
- Buesseler, K. O., Michaels, A. F., Siegel, D., and Knap, A. (1994). A three dimensional time-dependent approach to calibrating sediment trap fluxes. *Global Biogeochemical Cycles*, 8:179–193.
- Bullister, J. L. (1989). Chlorofluorocarbons as time-dependent tracers in the ocean. *Oceanography*, 89:12–17.
- Codispoti, L. (1989). Phosphorus vs. Nitrogen Limitation of New and Export Production. In Berger, W., Smetacek, V., and Wefer, G., editors, *Productivity of the Ocean: Present and Past*, number 44 in Dahlem Workshop Reports, pages 377–394. Wiley & Sons, Chichester, New York, Brisbane, Toronto, Singapore.
- de la Heras, M. and Schlitzer, R. (1999). On the Importance of Intermediate Water Flows for the Global Ocean Overturning. *Journal of Geophysical Research*, in print:xxx–xxx.
- Degens, E. and Kempe, S. (1991). Summary: Biogeochemistry of Major World Rivers. In Degens, E., Kempe, S., and Richey, J., editors, *Biogeochemistry of Major World Rivers*. Wiley & Sons, Chichester, New York, Brisbane, Toronto, Singapore.
- DeMaster, D. (1981). The supply and accumulation of silica in the marine environment. *Geochimica and Cosmochimica Acta*, 45:1715–1732.

- DeMaster, D., Nelson, T., Harden, S., and Nittrouer, C. (1991). The cycling and accumulation of biogenic silica and organic carbon in Antarctic deep-sea and continental margin environments. *Marine Chemistry*, 35:489–502.
- Deuser, W., Ross, E., and Anderson, R. (1981). Seasonality in the supply of sediment to the deep Sargasso Sea and implications for the rapid transfer of matter to the deep ocean. *Deep Sea Research*, 28A:495–505.
- Dyer, K. (1980). The measurement of fluxes and flushing times in estuaries. In Martin, J.-M., editor, *River inputs to ocean systems*, pages 67 – 76. Wiley & Sons, Chichester, New York, Brisbane, Toronto, Singapore.
- Eppley, R. (1989). New Production: History, Methods, Problems. In Berger, W., Smetacek, V., and Wefer, G., editors, *Productivity of the Ocean: Present and Past*, number 44 in Dahlem Workshop Reports, pages 85–97. Wiley & Sons, Chichester, New York, Brisbane, Toronto, Singapore.
- Eppley, R. and Peterson, B. (1979). Particulate organic matter flux and planktonic new production in the deep ocean. *Nature*, 282:677–680.
- Fischer, G. (1988). Seasonal variability of particle flux in the Weddell Sea and its relation to ice cover. *Nature*, 335:426–428.
- Fischer, G. (1996). Distinct year-to-year particle flux variations off Cape Blanc during 1988-1991: Relation to $\delta^{18}\text{O}$ -deduced sea-surface temperatures and trade winds. *Journal of Marine Research*, 54:73–98.
- Fischer, G. (1998). Organic carbon fluxes in the Atlantic and the Southern Ocean: relationship to primary production compiled from satellite radiometer data *submitted*.
- Fischer, G., Neuer, S., and Wefer, G. (1996). Short-term sedimentation pulses recorded with a fluorescence sensor and sediment traps at 900-m depth in the Canary basin. *Limnology and Oceanography*, 41(6):1354–1359.
- Fischer, G. and Wefer, G. (1999). Long-term Observation of Particle Fluxes in the Eastern Atlantic: Seasonality, Changes of Flux with Depth and Comparison with the Sediment Record. In Wefer, G., Berger, W., Siedler, G., and Webb, D., editors, *The South Atlantic: Present and Past Circulation*, pages 325–344. Springer, Heidelberg.
- GEOSECS (1998). Geochemical Ocean Sections Study. Internet <http://ingrid.ldgo.columbia.edu/SOURCES/.GEOSECS/>.
- Gust, G., Michaels, A. F., Johnson, A., Deuser, W., and Bowles, W. (1994). Mooring line motions and sediment trap hydrodynamics: in situ intercomparison of three common deployment designs. *Deep Sea Research*, 41:831–857.
- Honjo, S. and Manganini, S. (1993). Annual biogenic particle fluxes to the interior of the North Atlantic Ocean; studied 34°N21°W and 48°N21°W. *Deep Sea Research*, 40:587–607.

- Khripounoff, A. and Crassous, P. (1994). Particulate material degradation in sediment traps at 2000m depth on the Meriadzeck Terrace (Bay of Biscay). *Deep Sea Research*, 41:821–829.
- Lalli, C. and Parsons, T. (1997). *Biological Oceanography: an Introduction*. Open University. Butterworth-Heinemann, Oxford.
- Lampitt, R. and Antia, A. (1993). Particle flux in deep seas: regional characteristics and temporal variability. *Mar. Ecol. Prog. Ser.*, 96:1–15.
- Lerman, A. (1980a). Controls on river water composition and mass balance of river systems. In Martin, J.-M., editor, *River inputs to ocean systems*, pages 5 – 12. Wiley & Sons, Chichester, New York, Brisbane, Toronto, Singapore.
- Lerman, A. (1980b). Controls on river water composition and mass balance of river systems. In Martin, J.-M., editor, *River inputs to ocean systems*, pages 1 – 4. Wiley & Sons, Chichester, New York, Brisbane, Toronto, Singapore.
- Leynaert, A., Nelson, D., Quéguiner, B., and Tréguer, P. (1993). The silica cycle in the Antarctic Ocean: is the Weddell Sea atypical? *Deep Sea Research*, 96:1–15.
- Leynaert, A., Tréguer, P., Quéguiner, B., and Morvan, J. (1991). The distribution of biogenic silica and the composition of particulate organic matter in the Weddell-Scotia Sea during summer 1988. *Marine Chemistry*, 35:435–447.
- Lisitzin, A. (1985). The silica cycle during the last ice age. *Paleogeography, Paleoclimatology, Paleoecology*, 50:241–270.
- Lisitzin, A. (1996). *Oceanic Sedimentation*. AGU, Washington, D.C.
- Ludwig, W. (1996). Predicting the organic input of organic carbon by continental erosion. *Glob. Biogeochem. Cycles*, 10:23–41.
- Maier-Reimer, E. (1993). Geochemical cycles in an ocean general circulation model. Preindustrial tracer distributions. *Global Biogeochemical Cycles*, 7:645–677.
- Maier-Reimer, E. and Hasselmann, K. (1987). Transport and storage of CO₂ in the ocean - an inorganic ocean-circulation carbon cycle model. *Climate Dynamics*, 2:63–90.
- Martin, J., Knauer, G., Karl, D., and Broenkow, W. (1987). VERTEX: carbon cycling in the northeast Pacific. *Deep Sea Research*, 34:267–286.
- Matear, R. and Holloway, G. (1995). Modeling the inorganic phosphorus cycle of the North Pacific using an adjoint data assimilation model to assess the role of dissolved organic phosphorus. *Global Biogeochemical Cycles*, 9:101–119.
- Meybeck, M. (1980). Pathways of major elements. In Martin, J.-M., editor, *River inputs to ocean systems*. Wiley & Sons, Chichester, New York, Brisbane, Toronto, Singapore.
- Milliman, J. (1993). Production and accumulation of calcium carbonate in the ocean: Budget of a nonsteady state. *Glob. Biogeochem. Cycles*, 7:927–957.

- Murnane, R., Cochran, J., Buessler, K., and Bacon, M. (1996). Least-squares estimates of thorium, particle, and nutrient cycling rate constants from the JGOFS North Atlantic Bloom experiment. *Deep Sea Research*, 43:239–258.
- NABE (1998). JGOFS: North Atlantic Bloom Experiment. Internet <http://www1.whoi.edu/nabe.html>.
- Najjar, R., Sarmiento, J., and Toggweiler, J. (1992). Downward transport and fate of organic matter in the ocean: simulations with a general circulation model. *Global Biogeochemical Cycles*, 6:45–76.
- Nelson, D., Ahern, J., and Herlihy, L. (1991). Cycling of biogenic silica within the upper water column of the Ross Sea. *Marine Chemistry*, 35:461–476.
- Nelson, D., Tréguer, P., Brzezinski, M., Leynaert, A., and Quéguiner, B. (1995). Production and Dissolution of biogenic silica in the ocean: Revised global estimates, comparison with regional data and relationship to biogenic sedimentation. *Glob. Biogeochem. Cycles*, 9:359–372.
- NOAA (1998). Nimbus7 Coastal Zone Color Scanner. Internet <http://seawifs.gsfc.nasa.gov/SEAWIFS.html>.
- Orsi, A., Whitworth, T., and Nowlin, W. (1995). On the meridional extent and fronts of the Antarctic Circumpolar Current. *Deep Sea Research*, 42:641 – 673.
- Ragueneau, O., Tréguer, P., Anderson, R., Brzezinski, M., DeMaster, D., Dugdale, R., Dymond, J., Fischer, G., Heinze, C., Leynaert, A., Maier-Reimer, E., Martin-Jézéquel, V., Nelson, D., and Quéguiner, B. (1997). Understanding the Si cycle in the modern ocean, a pre-requisite for a better use of biogenic opal within a multi-proxy approach of paleoproductivity in the ocean. *Global and Planetary Change* submitted.
- Redfield, A., Ketchum, B., and Richards, F. (1963). The influence of organisms on the composition of sea water. In Hill, N., editor, *The Sea*, volume 2, pages 224–228. Interscience, New York.
- Roether, W., Manca, B., Klein, B., Bregant, D., Georgopoulos, D., Beitzel, V., Kovacevic, V., and Luchetta, A. (1996). Recent changes in eastern Mediterranean deep waters. *Science*, 271:333–335.
- Schlitzer, R. (1993). Determining the mean, large-scale circulation of the atlantic with the adjoint method. *J.Phys.Oceanography*, 23:1935–1952.
- Schlitzer, R. (1995). An adjoint method for the determination of the mean oceanic circulation, air-sea fluxes and mixing coefficients. *Berichte zur Polarforschung* 156, AWI, Bremerhaven.
- Schlitzer, R. (1999a). Applying the Adjoint Method for Global Biogeochemical Modeling. In Kasibhatla, P., Heimann, M., Hartley, D., Mahowald, N., Prinn, R., and Rayner, P., editors, *Inverse Methodes in Biogeochemical Cycles*, pages xxx–xxx. AGU, U.S.A.

- Schlitzer, R. (1999b). Ocean Data View by R. Schlitzer. Internet <http://www.awi-bremerhaven.de/GPH/ODV>.
- Schlüter, M., Rutgers van der Loeff, M., Holby, O., and Kuhn, G. (1998). Silica Cycle in Surface Sediments of the South Atlantic. *Deep Sea Research*, 45:1085–1109.
- Smith, R. (1995). The Physical Processes of Coastal Ocean Upwelling Systems. In Summerhayes, C., Emeis, K.-C., Angel, M., Smith, R., and Zeitzschel, B., editors, *Upwelling in the Ocean*, pages 40–64. Wiley & Sons, Chichester, New York, Brisbane, Toronto, Singapore.
- Suess, E. (1980). Particulate organic carbon flux in the ocean–surface productivity and oxygen utilization. *Nature*, 280:260–263.
- Sültenfuß, J. (1998). The radionuclide Tritium in the ocean: measurement and distribution of Tritium in the South Atlantic and the Weddel Sea. Berichte zur Polarforschung 256, AWI, Bremerhaven.
- Summerhayes, C., Emeis, K.-C., Angel, M., Smith, R., and Zeitzschel, B. (1995). Upwelling in the Ocean: Modern Processes and Ancient Records. In Summerhayes, C., Emeis, K.-C., Angel, M., Smith, R., and Zeitzschel, B., editors, *Upwelling in the Ocean*, pages 1–37. Wiley & Sons, Chichester, New York, Brisbane, Toronto, Singapore.
- Sundquist, E. (1985). Geological Perspectives on Carbon Dioxide and the Carbon Cycle. In Sundquist, E. and Broecker, W., editors, *The Carbon Cycle and Atmospheric CO₂: Natural Variations Archean to Present*. AGU, Washington.
- Tarantola, A. (1987). *Inverse Problem Theory*. Elsevier, Amsterdam.
- Thacker, W. (1988). Fitting Models to Inadequate Data by Enforcing Spatial and Temporal Smoothness. *Journal of Geophysical Research*, 93:655–664.
- Toggweiler, J. (1989a). Simulations of Radiocarbon in a Coarse-Resolution World Ocean Model 1. Steady State Prebomb Distributions. *Journal of Geophysical Research*, C6:8217–8242.
- Toggweiler, J. (1989b). Simulations of Radiocarbon in a Coarse-Resolution World Ocean Model 2. Distributions of Bomb-produced Carbon 14. *Journal of Geophysical Research*, C6:8243–8264.
- Toggweiler, J. and Samuels, B. (1993). Is the magnitude of the deep outflow from the Atlantic Ocean actually governed by southern hemisphere winds? In Heimann, M., editor, *The Global Carbon Cycle*, ASI, pages 303–331. NATO, Berlin.
- Tréguer, P., Nelson, D., Van Bennekom, A., DeMaster, D., Leynaert, A., and Quéguiner, B. (1995). The Silica Balance in the World Ocean: A Reestimate. *SCIENCE*, 268:375–379.
- Tréguer, P. and Van Bennekom, A. (1991). The annual production of biogenic silica in the Antarctic Ocean. *Marine Chemistry*, 35:477–487.

- Valdes, J., Buessler, K., and Price, J. (1998). A New Way to Catch the Rain. *Oceanus*, 40(2):33–35.
- Van Bennekom, A., Berger, G., Gaast, S. v. d., and Vries, R. d. (1988). Primary productivity and the silica cycle in the Southern Ocean (Atlantic sector). *Paleogeography, Paleoclimatology, Paleoecology*, 67:19–30.
- Van Bennekom, A., Buma, A., and Nolting, R. (1991). Dissolved aluminium in the Weddell-Scotia Confluence and effect of Al on the dissolution kinetics of biogenic silica. *Marine Chemistry*, 35:423–434.
- Van Bennekom, A. and Salomons, W. (1980). Pathways of nutrients and organic matter from land to oceans through rivers. In Martin, J.-M., editor, *River inputs to ocean systems*. Wiley & Sons, Chichester, New York, Brisbane, Toronto, Singapore.
- Walsh, I., Dymond, J., and Collier, R. (1988). Rates of recycling of biogenic components of settling particles in the ocean derived from sediment trap experiments. *Deep Sea Research*, 35:43–58.
- Wassmann, P. (1993). Regulation of Vertical Export of Particulate Organic Matter from the Euphotic Zone by Planktonic Heterotrophs in Eutrophicated Aquatic Environments. *Marine Pollution Bulletin*, 26:636–643.
- Wassmann, P. and Slagstad, D. (1993). Seasonal and annual dynamics of particulate organic carbon flux in the Barents Sea. *Polar Biology*, 13:363–372.
- Wunsch, C. (1984). An Estimate of the Upwelling Rate in the Equatorial Atlantic Based on the Distribution of Bomb Radiocarbon and Quasi-Geostrophic Dynamics. *Journal of Geophysical Research*, 89:7971–7978.
- Wunsch, C., Hu, D., and Grant, B. (1983). Mass, Heat, Salt and Nutrient Fluxes in the South Pacific Ocean. *Journal of Physical Oceanography*, 13:725–753.
- Yamanaka, Y. and Tajika, E. (1996). The role of the vertical fluxes of particulate organic matter and calcite in the oceanic carbon cycle: Studies using an ocean biogeochemical general circulation model. *Global Biogeochemical Cycles*, 10:361–382.
- Yamanaka, Y. and Tajika, E. (1997). Role of dissolved organic matter in the marine biogeochemical cycle: Studies using an ocean biogeochemical general circulation model. *Global Biogeochemical Cycles*, 11:599–612.